The Detection of Gravitational Microlensing Anomalies

Pierre le Roux Vermaak
Co-supervisors Dr. John Menzies and Prof. Brian Warner
In fulfilment of the MSc degree in Astronomy at the University of Cape Town
1997-1998

The Detection of Gravitational Microlensing Anomalies

Pierre le Roux Vermaak
Co-supervisors Dr. John Menzies and Prof. Brian Warner
In fulfilment of the MSc degree in Astronomy at the University of Cape Town
1997-1998

DST 520 VERM

99/9914

To Barbara, for everything.

Abstract

The detection and measurability of microlensing anomalies including planet detection, resolved source, blending and parallax effects are investigated by way of an extensive computer simulation as a function of the observation strategy. The most efficient strategy has a planet detection probability exceeding 75% for the most favourable binary geometry, while results for typical event follow up and survey observations agree well with previous work. A complex dependence of planet detection on the resolved source radius is discovered leading to a possible increase in the probability of detecting planets with mass ratios smaller than $q = 10^{-3}$.

Contents

List of Figures

Chapter 1

Introduction

A few observations and much reasoning leads to error, many observations and a little reasoning to truth.

Alexis Carrel (1873-1944)

1.1 Microlensing

When light from a luminous background object, like a distant star, passes very close to a massive foreground object, such as another star halfway between the background star and the observer, the gravitational field of the foreground object will bend the light rays from the background star. Depending on the precise geometry, the net effect may be to let the foreground object work like a natural lens, magnifying the background object, or source. This is the basis of gravitational lensing.

The idea of the gravitational deflection of light dates back as far as the Newtonian theory of gravity. As is well known to undergraduate physics students, the Newtonian angle of deflection is exactly half that predicted by General Relativity Theory [Einstein 1911], which has been experimentally verified in recent times. Einstein thought that the effect was unlikely ever to be observed [Einstein 1936], but the first observation was made 43 years later in [Walsh et al. 1979]. In this case the source was a quasar, but many other scenarios are feasible.

Galactic microlensing, in particular, deals with stars in the Local Group or the Galactic Bulge that are lensed by stellar-sized objects [Paczynski 1986]. On a Galactic scale, the individual images of the source star that are formed by a gravitational lens are too close together in the sky to be resolved, but much may be learnt from the integrated light of the images of the source. It was hoped that Galactic microlensing could be used to constrain some

of the properties of the dark matter distribution in the Galactic Halo. Paczynski concluded that any star in the Bulge has a very small chance of undergoing observable lensing, of the order of one in a million. If 10^7 stars are monitored, however, a few events should be seen in progress at any one time. After the Paczynski paper, survey groups did indeed form to look for Galactic Microlensing events towards the Bulge, the LMC and the SMC (and more recently M31). The first detections were published in 1993 by the MACHO [Alcock et al. 1993] and EROS [Aubourg et al. 1993] collaborations.

Impressive as these detections were, microlensing had still more to offer. It was pointed out [Mao & Paczyski 1991] that if the lensing object had a companion, even of planetary size, the single lens light curve may be altered in such a way as to allow detection of the planet. Microlensing joined the ranks of a few observational methods capable of detecting extra-solar planets. In addition, a planet could be detected at any time, in contrast to the orbital period timescale required by other methods such as radial velocity measurements or astrometry.

The detection probability, given that the lens has a planet or planets in orbit, has been calculated and revised several times. One estimate [Gould & Loeb 1992] suggested that 20% of microlensing events towards the Bulge would display perturbations of more than 5% if all lenses had planetary systems like our own. Bolatto and Falco estimated that 40% of light curves would be sufficiently perturbed so as to be detectable in the presence of a Jovian mass companion [Bolatto & Falco 1994]. Detection probability was later extended down to Earth-mass planets [Bennett & Rhie 1996], and these calculations were the first to include the effects of a resolved source (background) star where previous estimates were made using a point source model. Detection probabilities of more than 2% for Earth-mass planets and 10% for Neptune-mass planets were calculated, requiring a 4% deviation from the single lens light curve and provided that the planets reside in a narrow strip of orbital separation from the primary called the lensing zone.

The possibility of detecting planets as well as other anomalies discussed below, led to the formation of several "follow up" groups, notably the PLANET [Albrow et al. 1998] and GMAN [Becker et al. 1997] collaborations. These groups act on alerts issued by the survey groups when microlensing events in progress are detected. Dedicated observations of specific events allow much higher sampling frequencies and better photometry than a general survey.

1.2 Origin of this project

Although several estimates are available for planet detection efficiency and the measurability of other anomalies such as parallax and resolved source effects, previous investigations were sometimes fragmented in parameter space and did not consider all anomalies. There was need for estimates of the measurability of parameters such as parallax to optimise observation strategy and improve the planet detection efficiency of the observational groups.

1.3 Parameter space

Parts of planetary parameter space have been investigated in the past, but with several gaps and approximations. A good example of this is how the crucial role played by the central caustic in planet detection was missed until 1997 [Griest & Safizadeh 1997]. Large parts of the parameter space remain to be explored. One such exploration into the resolved source effect appears to have borne fruit in this investigation, giving a detection probability much larger than previously expected for planets with small mass ratios.

The interaction of various anomalies with each other has not been fully explored. The effects of blending on planet detection for example, although analytically extremely simple, have been excluded from most estimates.

1.4 Overview

The goals of this project can be summarized as follows:

1. The development of reliable computer software to simulate microlensing events, leading to:

2. The investigation of a large region of binary microlensing event parameter space, concentrating on planet detection, where mass ratios of $q = 10^{-3}$ or smaller are considered.

3. Investigation of other anomalies: parallax, blending and resolved source effects, and their interaction.

4. Finding the optimal planet detection strategy, taking observational methods and limitations into account. The detectability of other anomalies were also investigated, especially the parallax and resolved source effects, because of their potential to yield additional constraints on the lens parameters for some fraction of microlensing events.

The theory of microlensing and all the anomalies investigated in this project are discussed in chapter 2. Chapter 3 deals with the models adopted for simulating the distribution of microlensing parameters and the detection criteria. Chapter 4 describes numerical and calculation methods used to determine detection probability and distributions of parameters. Results are discussed in chapter 5 and the main conclusions and recommendations are set out in chapter 7. Finally, sources of error are discussed in chapter 6.

I would like to thank John Menzies and Brian Warner for supervision of the project, and Penny Sackett for many helpful discussions. Many thanks also to the South African Astronomical Observatory for the use of their facilities. This work was made possible by a bursary from the Foundation for Research Development (South Africa).

Chapter 2

Theory

2.1 The point source point mass lens model (SL)

The geometry of a microlensing event, approximating the source as a point source and the lens as a point mass, is illustrated in Fig. 2.1. D_s, D_l and D_{ls} represent the distance to the source plane from the observer, the distance to the lens plane from the observer, and the distance between lens and source planes, respectively. α is the well-known Einstein deflection angle for a ray of light passing within a distance r of an object with mass m, given by

$$\alpha = \frac{4Gm}{c^2 r} \tag{2.1}$$

The origins of the lens and source planes are chosen so as to fall on a line of sight from the observer to the source plane. y represents the distance from the origin in the source plane to the actual position of the source at S. x is the distance from the origin to the observed position of the source due to deflection, at S_i

As D_s, D_l and D_{ls} are O(kpc), while x and y are O(AU), we can assume that the angles involved are small, validating the thin lens approximation which yields

$$\alpha = \frac{x - y}{D_{ls}} \tag{2.2}$$

Now we introduce the coordinate change $x_1 = \frac{D_l}{D_s}x$ and $y_1 = \frac{D_l}{D_s}y$: x_1 and y_1 is the projection of x and y onto the lens plane. Substituting Eq. 2.1 in Eq. 2.2 for α, we obtain

$$\frac{D_s}{D_l}y_1 = \frac{D_s}{D_l}x_1 - \frac{4GmD_{ls}}{c^2\left(x_1 - x_m\right)} \tag{2.3}$$

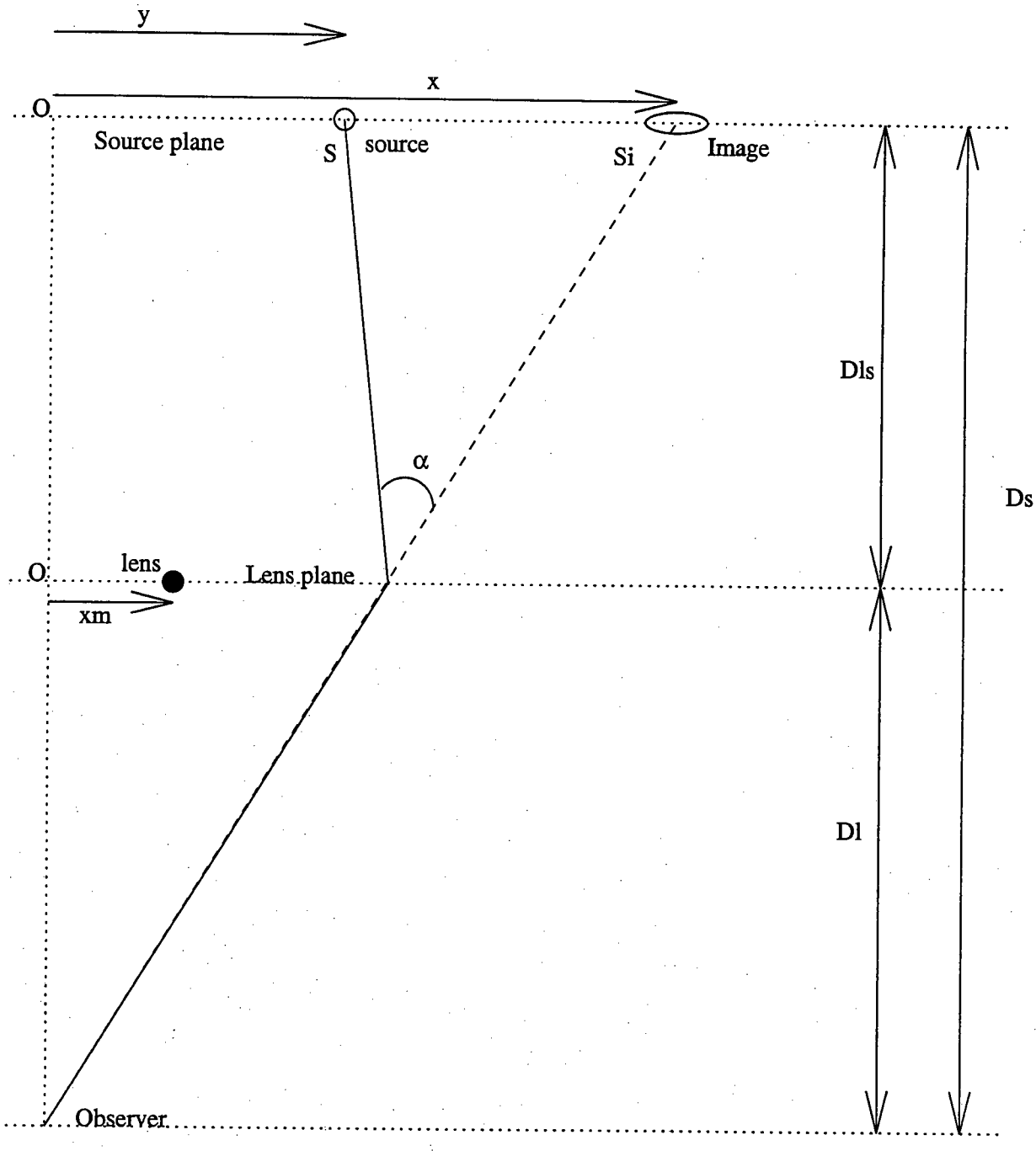

Figure 2.1: The geometry of a single lens microlensing event.

where x_m is the position of the lens in the lens plane. If we make the substitution

$$r_E = \sqrt{\frac{4GmD_{ls}D_l}{c^2 D_s}} \tag{2.4}$$

in Eq. 2.3, we find

$$y_1 = x_1 - \frac{r_E^2}{(x_1 - x_m)} \tag{2.5}$$

We introduce another coordinate change, making the unit of length the Einstein radius r_E, i.e. $x_2 = \frac{x_1}{r_E}$ and $y_2 = \frac{y_1}{r_E}$, yielding

$$y_2 = x_2 - \frac{1}{(x_2 - x_m)} \tag{2.6}$$

where the position x_m is in the same coordinates as x_2. Eq. 2.6 is called the lens equation. It is easily generalized to include more lenses in the thin lens approximation. Using complex notation,

$$\zeta = z + \frac{1}{(\overline{z_1} - \overline{z})} + \sum_{i=2}^{n} \frac{q_i}{(\overline{z_i} - \overline{z})} \tag{2.7}$$

where q_i is the mass ratio of a secondary or companion lens to the primary lens and ζ is the source position. z_1 and the z_i's are the positions of the primary and companions, respectively, measured in units of the primary lens r_E and projected to the lens plane. $\overline{z}$ denotes the complex conjugate of z, where z is an image position. The origin may be chosen arbitrarily and it is now chosen to be at the position of the primary lens, making $z_1 = 0$.

Eq. 2.7 is a transformation from source position to image position. Because each light ray preserves its intensity, the magnification of a single image of the source is given by the ratio of solid angle of the image to that of the source. Therefore the amplification of each image is given by the inverse of the Jacobian matrix of the transformation.

In the single lens case, a straight forward derivation [Witt 1990] to determine the amplification of any image yields

$$A = \frac{1}{\det[J]} = \frac{|z|^4}{|z|^4 - 1} \tag{2.8}$$

By taking the complex conjugate of the lens equation (2.6) and substituting for $\overline{z}$, we obtain two image positions, at

$$|z_{1,2}| = \frac{|\zeta| \pm \sqrt{|\zeta|^2 + 4}}{2} \tag{2.9}$$

Adding the amplification from both images gives the total amplification. Replacing $|\zeta|$ with u, the source's distance from the origin in the source plane, we obtain the single point mass lens amplification

$$A = \frac{u^2 + 2}{u\sqrt{u^2 + 4}} \tag{2.10}$$

2.2 Binary point mass lenses (BL)

Eq. 2.7 is a general lensing formula applicable to a point source and any number of point mass lenses. The lens equation for a binary lens only is

$$\zeta = z + \frac{1}{\overline{z_1} - \overline{z}} + \frac{q}{\overline{z_2} - \overline{z}} \tag{2.11}$$

Although the addition of one extra term looks innocuous enough, it introduces almost incredible complexity into the lensing model. Eq. 2.11 can no longer be solved analytically for image positions, z. It has a variable number of solutions (found numerically): either three or five, depending on the source position (ζ), the primary and secondary lens positions (z_1 and z_2) and the mass ratio q. It leads to an almost infinite variety of possible light curves in a highly non-linear fashion, depending on the parameters mentioned above and the geometry of the source crossing. Finally, sets of parameters obtained from fits to insufficiently sampled light curves are seldom unique and may inhabit very different areas of parameter space.

One option for the numerical solution of Eq. 2.11 is similar in nature to the solution of the single lens equation. First, image positions are obtained for a given lens geometry and source position (numerically), then the amplification for these images is obtained by calculating the determinant of the Jacobian transformation matrix for each in turn. The total amplitude is given by the sum of the reciprocals of the determinants. This approach was used in the calculation of light curves and magnification maps for binary lenses in this project, as discussed below. It is by no means the only option, with the most obvious alternative being the 'ray shooting' method, also discussed below.

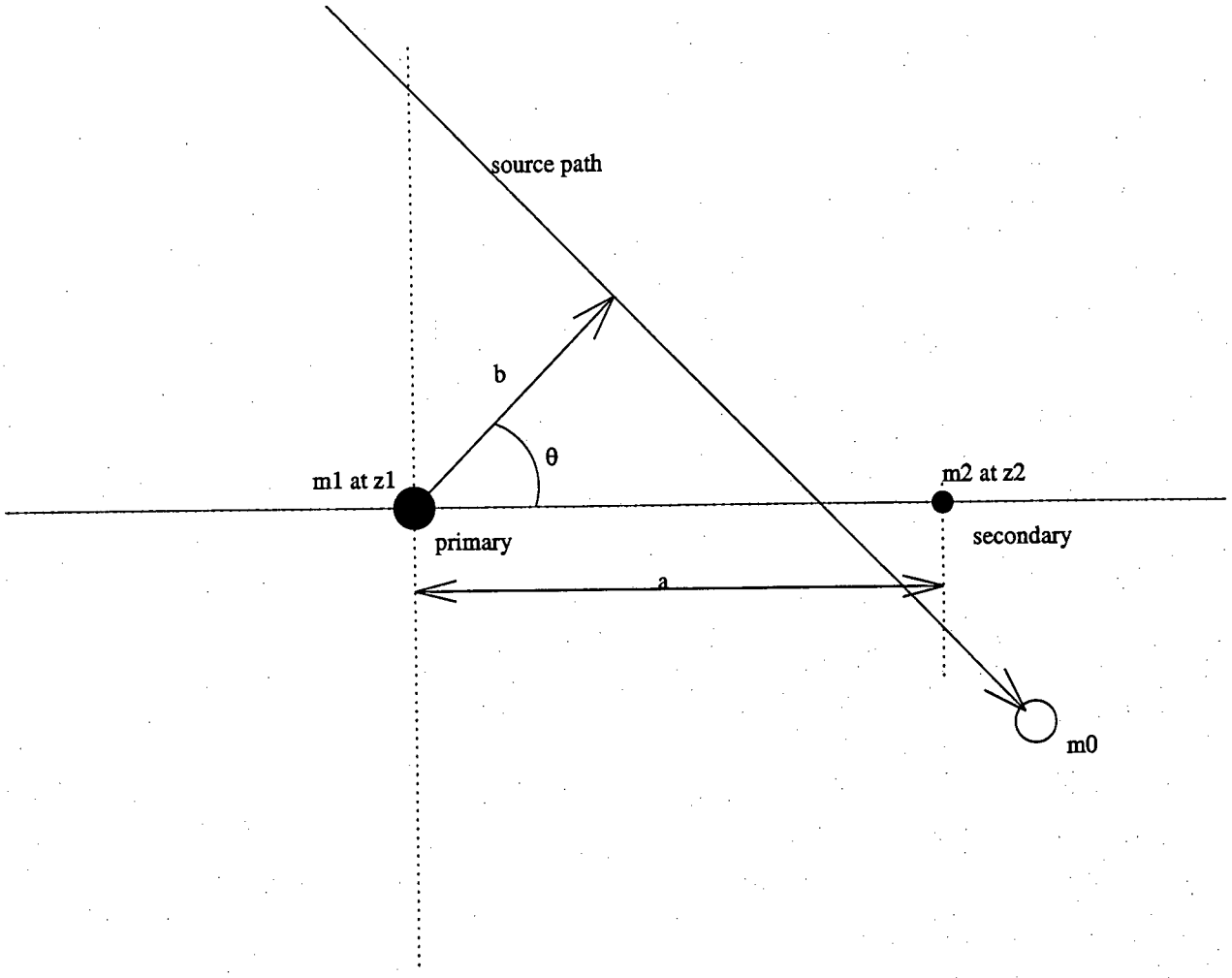

Figure 2.2: Binary event geometry, as seen along the line of sight, projected onto the lens plane.

2.2.1 The binary lens equation and event geometry

The geometry of a binary lens event is illustrated in Fig. 2.2.

Fig. 2.2 shows the source projected onto the lens plane. All lengths are in units of the Einstein radius of the primary, projected onto the lens plane. The primary is arbitrarily positioned at the origin, making $z_1 = 0$. There are seven parameters involved in a binary lens event light curve. These are

1. The projected binary separation, a, projected to the lens plane. With z_1 at the origin, $a = z_2$.

2. The mass ratio, q. This is simply $\frac{m_{secondary}}{m_{primary}}$.

3. The impact parameter of the source from the primary, b.

4. The angle between the impact parameter vector, b, and the positive real (x) axis, θ.

5. The Einstein radius crossing time, in days, t_E.

6. The time of closest approach to the primary, t_m.

7. The unlensed magnitude of the background star, m_0.

If we allow θ to take any value from 0 to 360, and say all sources move across the impact parameter vector from left to right when b is pointing parallel to the positive y axis, these parameters uniquely describe any point lens binary event (excluding other anomalies, such as resolved source effects or blending of light). The symmetry around the x axis allows us to always move the source from left to right, as this is completely equivalent to movement from right to left with θ advanced by 180 degrees.

The biggest difference between the single and binary lens cases, is the creation of caustics in the binary case. A caustic is defined as a point or continuous curve where the amplification of a source positioned on that point or curve diverges, for the point lens model. There is a related curve for every caustic curve, called a critical curve, where the amplification will diverge if an image is positioned on such a curve. Caustic curves are easily obtained from critical curves by substituting a critical point into the lens equation to obtain the caustic position corresponding to that image position.

For a single lens, we see from Eq. 2.10 that the amplification diverges for impact parameters approaching zero, corresponding to a single point caustic at the origin. The corresponding critical curve for the single lens caustic is in fact a ring with radius $1r_E$.

For binary lenses, the position of the critical curves can be obtained by setting the determinant of the Jacobian, ($[J]$), equal to zero, with $\det[J]$ given by

$$\det[J] = 1 - \frac{\partial\zeta}{\partial\overline{z}}\overline{\frac{\partial\zeta}{\partial\overline{z}}} \tag{2.12}$$

and

$$\frac{\partial\zeta}{\partial\overline{z}} = \frac{1}{(\overline{z_1} - \overline{z})^2} + \frac{q}{(\overline{z_2} - \overline{z})^2} \tag{2.13}$$

Note that the position of amplification peaks in an ongoing microlensing event can be predicted from extrapolating the expected path of the source through caustic crossings. Even

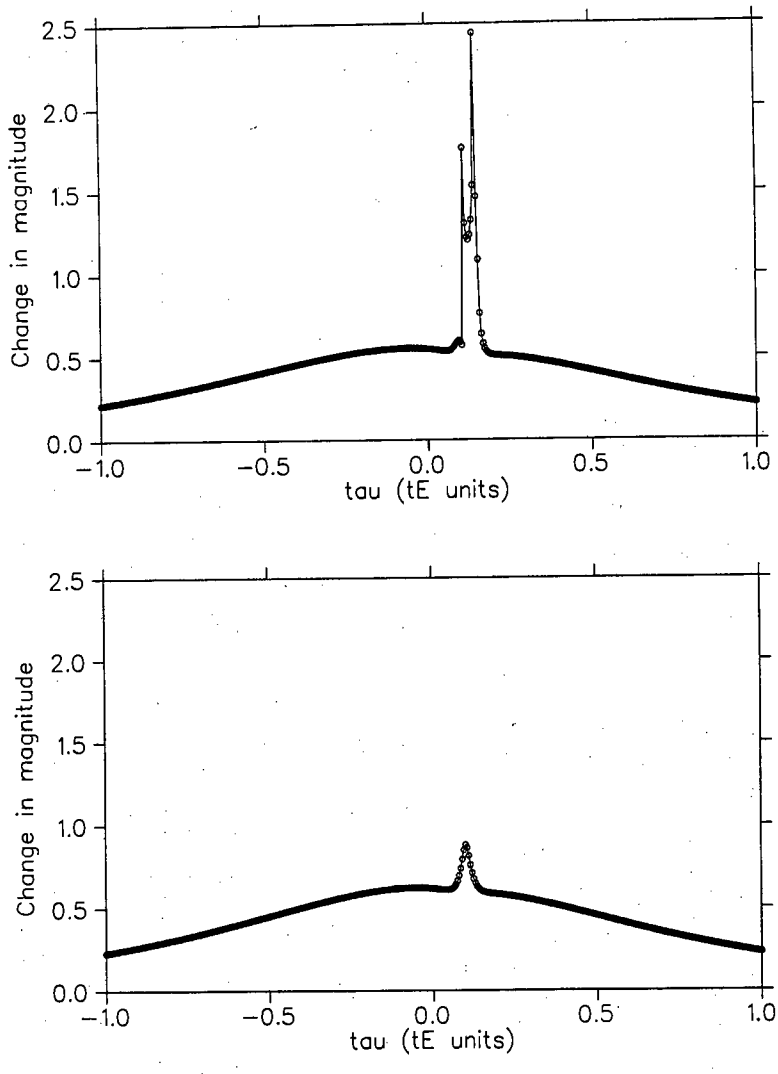

Figure 2.3: Two light curves of planetary events for a Jovian-mass planet, with all parameters varied by 10% from the top curve to the bottom curve.

when caustics are not crossed, major perturbations to the light curve may still occur. Caustics of binary lens light curves are discussed in depth in the literature [Schneider & Weiss 1986].

2.2.2 Sensitivity to small parameter changes

Binary events with slightly different parameters can lead to very different light curves. This is because the main features of binary light curves depend strongly on the positions of the caustic curves which can change dramatically with a small change in the binary parameters. The point is illustrated in Fig. 2.3, where 10% is added to all the binary parameters of the top event to generate the bottom event.

Such large variations should facilitate the fitting of a binary light curve, but does not necessarily improve the degeneracy situation.

2.2.3 Real binaries vs. Planets

So far no distinction has been made between light curves caused by binaries in general and those caused by planets. Both are governed by the lens equation (2.11), but in binaries with a mass ratio of around 10^{-3} and smaller, the secondary is generally considered to be a planet. In the Solar system, Jupiter has a mass ratio of almost exactly 10^{-3}, Saturn 5.16×10^{-5} and Earth 3.0×10^{-6}. The main difference between planetary and binary light curves is that planetary curves can be approximated as a single lens light curve with a lens the same mass as the primary, with a local perturbation added at some point in the curve. Binary light curves are often so different from single lens curves, that is a single lens with mass equal to the sum of or any one of the components, that it is difficult to compare them at all.

A few rules of thumb on mass ratios:

1. The perturbation width decreases with decreasing mass ratio.

2. High mass ratio (closer to equal mass) binaries are easy to detect. It has been shown [Gaudi & Gould 1996] that they are in fact almost impossible to miss for binary separations larger than 0.4 r_E, corresponding to about 1 AU for typical Bulge distances and assuming modest detection criteria.

3. A planet causes a much larger perturbation to the magnification map than you would expect from simply comparing the planet's Einstein radius to that of the primary,

$$\frac{r_{E(planet)}}{r_{E(primary)}} \propto \sqrt{q} \tag{2.14}$$

Instead, the caustic structure extends across parts of the difference map not localised to the position of the planet.

Other effects such as finite source resolution and blending were not considered above, and these may change the situation to a degree.

2.2.4 Approximations

The binary lens equation cannot be solved analytically leading to the development of various useful approximations in order to get some analytical hold on the problem.

The single lens equation,

$$\zeta = z + \frac{1}{\overline{z_1} - \overline{z}} \tag{2.15}$$

and binary lens equation, Eq. 2.11 differ only in the addition of the last term. Therefore the single lens equation is in fact a good approximation to binary lenses as long as q is small or $z \neq z_2$. This has the following physical interpretation: planets influence the single lens scenario when one of the images of the source happens to cross the position of the planet (all projected onto the lens plane), in other words $z \approx z_2$, and the planet perturbs the image in much the same way that the primary perturbs the source image in the first place.

A quick approximation would then be

$$\zeta \approx z_2 + \frac{1}{\overline{z_1} - \overline{z_2}} \tag{2.16}$$

or with $z_2 = a$,

$$\zeta \approx a - \frac{1}{a} \tag{2.17}$$

This approximation gives us the positions of the caustics, ζ, as a function of the projected orbital separation, a. It is quite good for small q. An additional level of accuracy may be attained by replacing z_2 with $z_2 + \epsilon$ where ϵ is small, and approximating to first order. This is known as the Chang-Refsdal approximation.

The use of the quick approximation above is illustrated in the derivation of the lensing zone. As discussed below in 5.1, the highest detection probability by far is to be found in a narrow region of projected planet separation, a. If an area in the lens plane within R_c Einstein radii of the primary is monitored for planetary anomalies, only those anomalies with caustic regions within a radius of R_c will be detected. Using Eq. 2.17, we find the boundaries of the lensing zone by imposing

$$a - \frac{1}{a} = R_c \tag{2.18}$$

yielding

$$|a| = \left| \frac{R_c \pm \sqrt{R_c^2 + 4}}{2} \right| \tag{2.19}$$

For a value of $R_c = 1$, Eq. 2.19 gives a lensing zone of $0.6 < a < 1.6$, in very good

agreement with previous results in the literature. Two other values of R_c of importance in this project are $R_c = 2$ and $R_c = 0.1$, for lensing zones of $0.4 < a < 2.4$ and $0.95 < a < 1.05$.

The approximations are far from ideal, as is immediately evident from the fact that z is approximated by z_2, but that $z_2 \neq z$ to avoid a singularity at z_2. In addition both approximations contain no information about the central caustic. The Chang-Refsdal approximation is a useful one nonetheless, and the quick approximation is used later.

2.3 The parallax effect

Theoretically, a microlensing event should show a departure from the standard model light curve when the motion of the observer is taken into account. This "parallax effect" is negligibly small for most Galactic events, but has been measured at least once to date, for example [Alcock et al. 1995]. The measurement of parallax enables the observer to find an additional constraint (see below) on the physical parameters of the event: the mass, distance to, and transverse velocity of the lens. In general these quantities cannot be measured directly as only one observable parameter in a point source, single point mass lens yields information about the three physical parameters.

One of the goals of this section was to determine the range in parameter space in which a reasonably accurate measurement of parallax parameters could be obtained, as well as estimating how often the anomaly occurs. As a result of the Earth's motion, parallax affects all microlensing events. In most cases, however, the effect is negligible. To measure parallax, a theoretical model that includes the Earth's orbital motion is fit to an observed light curve. As opposed to binary lens anomalies, the amplification as a function of time can be calculated analytically, facilitating the fitting procedure. The formal errors (the pivots of the covariance matrix for a chi-square fit) in the two parallax parameters, ρ and ψ, were calculated to evaluate how frequently parallax could be measured for any given light curve.

Parallax was treated separately from binary perturbations, as these anomalies are essentially independent. Any binary event can exhibit parallax effects, but with the same frequency of occurrence and severity as that expected for an SL event. A notable exception to this statement is the case of a binary event with a high amplitude caustic crossing. In such cases, it may be possible to compare light curves obtained by observers separated by a distance of the order of an Earth radius to obtain additional information about the lens. See [Hardy & Walker 1995] for a discussion.

For an SL event, the amplification is given as a function of the projected distance between

the source and the lens, measured in units of Einstein radius in the lens plane. See Eqs. 2.10, 2.20, and 2.21.

$$u \equiv u(\tau) = \sqrt{b^2 + \tau^2} \tag{2.20}$$

$$\tau = \frac{t - t_m}{t_E} \tag{2.21}$$

$u(t)$ and its associated light curve in the presence and absence of parallax are shown in Fig. 2.4. Also shown is the path of the source, when the impact parameter, b, and the time scaled to the Einstein ring radius crossing time, τ, are taken as y and x coordinates in the lens plane. The lens is at the origin.

When the Earth's motion is included in the calculation, it introduces a periodical perturbation to this path, with period equal to that of the orbital motion of the Earth (1 year). The first consequence of the perturbation is that the SL curve loses its symmetry around the peak amplification.

The influence of parallax is small for most microlensing events. In extreme cases, however, parallax could theoretically be responsible for causing distortions as severe as multiple peaks, but no events of this type have been observed to date.

2.3.1 Derivation

Following [Dominik 1996], we choose $p(t)$ as a parameter along the unperturbed source trajectory, and $d(t)$ as the parameter perpendicular to it. With the lens at the origin, $p(t)$, $d(t)$ and $u(t)$ are given by equations 2.22 to 2.24.

$$p(t) = \tau(t) + \cos\psi\,(x_1(t) - x_1(t_m)) + \sin\psi\,(x_2(t) - x_2(t_m)) \tag{2.22}$$

$$d(t) = b - \sin\psi\,(x_1(t) - x_1(t_m)) + \cos\psi\,(x_2(t) - x_2(t_m)) \tag{2.23}$$

$$u(t) = \sqrt{p^2(t) + d^2(t)} \tag{2.24}$$

$x_1(t)$and $x_2(t)$ are the dimensionless coordinates for the Earth's motion, projected onto the lens plane. They are:

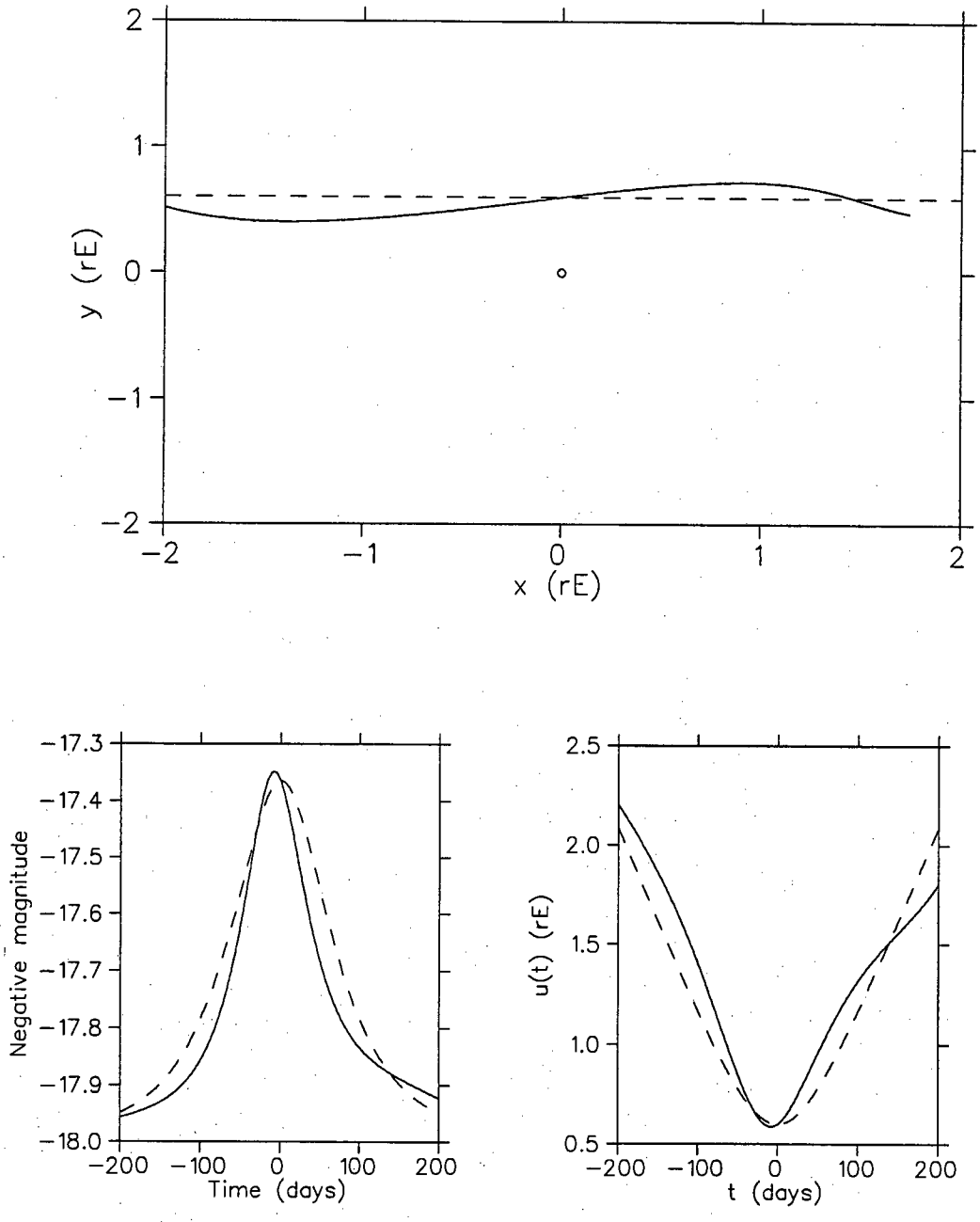

Figure 2.4: Three graphs to illustrate the parallax effect. The path of the source in the lens plane is shown in the top figure. The observed light curve is at bottom left, and the distance from the lens, $u(t)$ is at bottom right. The unperturbed event is indicated by a dashed line.

$$x_1(t) = \rho\left(-\sin\chi\cos\phi\,(\cos\xi(t) - \epsilon) - \sin\chi\sin\phi\sqrt{1-\epsilon^2}\sin\xi(t)\right) \tag{2.25}$$

$$x_2(t) = \rho\left(-\sin\phi\,(\cos\xi(t) - \epsilon) + \cos\phi\sqrt{1-\epsilon^2}\sin\xi(t)\right) \tag{2.26}$$

The angles ϕ and χ are the longitude in the ecliptic plane from the perihelion towards the Earth's position, and the latitude measured from the ecliptic plane towards the ecliptic north, respectively. They are related to the ecliptic coordinates of the source in the sky (β, λ) as follows:

$$\chi = \beta \tag{2.27}$$

$$\phi = \lambda + \pi + \phi_{aries} \tag{2.28}$$

$$\cos(\phi_{aries}) = \frac{\cos\left(\xi_{aries} - \epsilon\right)}{1 - \epsilon\cos\xi_{aries}} \tag{2.29}$$

τ_{aries} is the time of the vernal equinox. ψ is a rotation angle in the lens plane describing the relative orientation of the transverse velocity of the lens to the sun-Earth system. t_m refers to the time of closest approach by the source to the lens for the unperturbed light curve with identical non-parallax parameters. $x_1(t_m)$ and $x_2(t_m)$ are subtracted from $x_1(t)$ and $x_2(t)$ in equations 2.22 and 2.23 to facilitate comparison between a parallax perturbed light curve and an SL curve with the same parameters but no parallax. With the subtraction, we get the same values of $p(t)$ and $d(t)$ (and therefore $u(t)$ and $A(t)$) at $t = t_m$, with or without parallax added into the calculation.

$\xi(t)$ is a variable that introduces the Earth's period in the following relation:

$$2\pi\left(\frac{t - t_p}{T} - \left\lfloor\frac{t - t_p}{T}\right\rfloor\right) = \xi - \epsilon\sin\xi \tag{2.30}$$

The Earth's trajectory may be approximated to first order in eccentricity ϵ to make Eq. 2.30 analytically solvable. This reduces Eq. 2.30 to:

$$\xi(t) = 2\pi\frac{t - t_p}{T} + 2\epsilon\sin\left(2\pi\frac{t - t_p}{T}\right) \tag{2.31}$$

In the above, the parameters T, the Earth's period, ϵ, the Earth's eccentricity, and t_p, the time of perihelion, are all known. So are β and λ for the microlensing event in question, and

therefore ϕ and χ. The two new parameters that can be obtained from a fit of the parallax model to an event with measurable parallax, both of which describe physical information about the lens are ρ and ψ. ρ is given by:

$$\rho = a_{semi}\frac{1-x}{r_E} \tag{2.32}$$

where x is the distance to the lens, as a fraction of source distance, and r_E is the Einstein radius of the lens. a_{semi} is the semi-major axis of the Earth. Whereas ψ is an angle, ρ is the ratio of the Earth's orbital radius to the Einstein radius of the lens projected to the Earth's position.

For a very large projected Einstein radius (small ρ), the Earth's motion will be insignificant. For a small r_E at a medium x, ρ can be quite large. However, a small r_E could also mean a short Einstein radius crossing time, t_E, which in turn diminishes the effect of parallax. The connection between the observation of parallax and the parameters involved are investigated below.

2.4 The blending effect

A departure from the SL point source model is seen if the source being monitored contains a component of unlensed light. This component may be due to an unlensed star close to the line of sight to the source star, or due to a luminous lens. The effect is the same. The blended amplification is

$$A_{blend} = \frac{A_{abs}L_s + L_x}{L_s + L_x} \tag{2.33}$$

where L_s and L_x are the apparent fluxes from the lensed source star and the unlensed component respectively. A_{abs} is the amplification expected from an unblended source, and A_{blend} is the observed amplification. We now define the blending parameter f as

$$f = \frac{L_s}{L_s + L_x} \tag{2.34}$$

i.e. the fraction of the total flux that is coming from the lensed star. Replacing into Eq. 2.33 we obtain

$$A_{blend} = fA_{abs} + (1-f) \tag{2.35}$$

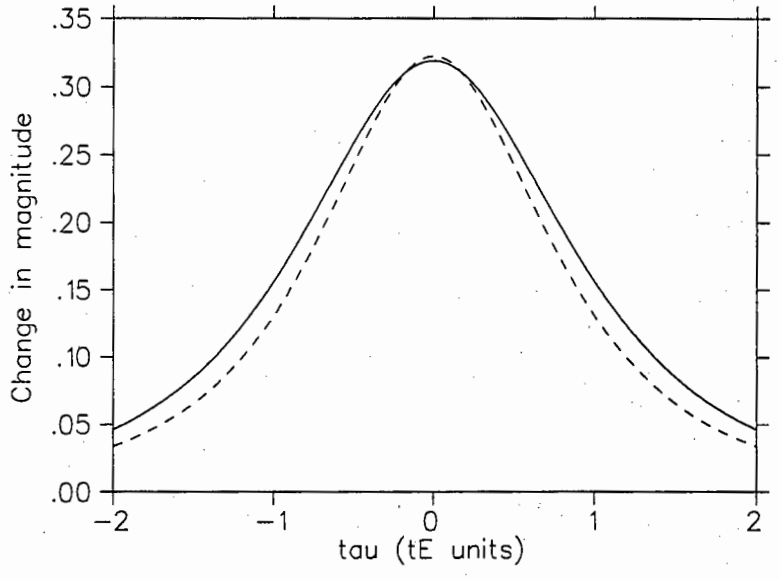

Figure 2.5: Substantially degenerate light curves due to blending. The solid line represents parameters $b = 1.0$ $f = 1.0$ while the dashed line represents $b = 0.8$ $f = 0.65$.

For $f = 1$ we regain the absolute amplification, and for $f = 0$ there is no amplification whatsoever.

Blending dilutes amplification. This is apparent from the fact that

$$D_f(A_{blend}) = A_{abs} - 1 > 0 \tag{2.36}$$

With increasing blending (decreasing f) the observed amplification will be lower than expected. Both the interpretation and the observation of microlensing events are affected.

A blended microlensing event will be harder to detect due to the lower amplification. Current microlensing surveys typically detect events towards the Galactic Bulge only if their amplification is higher than about $A = 1.34$, corresponding to a projected separation between lens and source of 1 r_E . If the event is detected, blending could still lead to misinterpretation of the event parameters. The Einstein radius crossing time, t_E, will appear to be shorter than its true value. The impact parameter, b, will appear to be larger. Therefore degeneracy is introduced between high amplification events with substantial blending, and low amplification events with minimal blending. Fig. 2.5 illustrates this effect.

Perturbations due to binary lenses (including planets) are also adversely affected. Because the detection of a planet orbiting a lens involves the observation of a short duration rise or drop in amplification superimposed on the expected single lens light curve, any reduction of the difference between the binary light curve and the single lens light curve will hamper

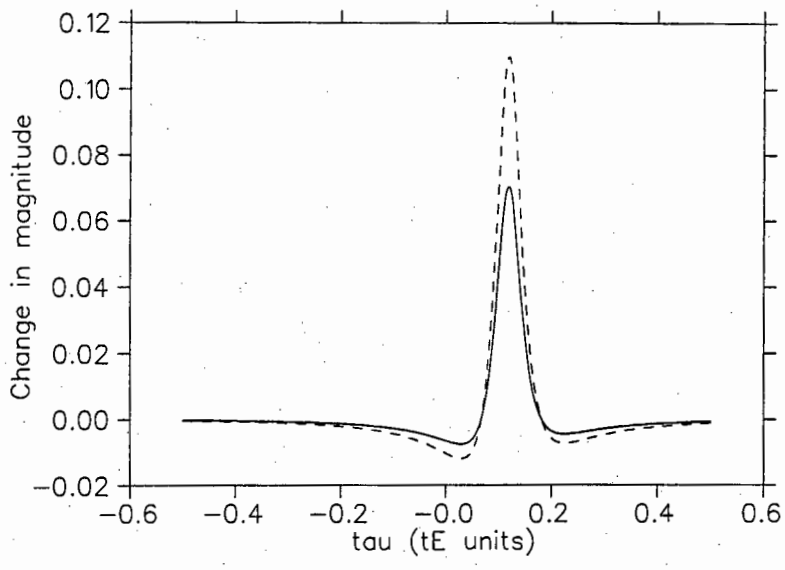

Figure 2.6: The effect of blending on a perturbation. This graph shows a difference curve in the absence (dashed line) and the presence (solid line) of moderate blending ($f = 0.5$).

detection. This effect is illustrated in Fig. 2.6. Clearly, as

$$(A_{bin} - A_{sl})_{blend} = f\,(A_{bin} - A_{sl})_{abs} \tag{2.37}$$

all perturbations are reduced by a factor f, the blending factor. (Drops in amplification as well as rises are evened out.) If uncorrected, blending will also affect statistical results based on the total amount of detections and the parameters t_E and b, for single lenses. All the parameters involved in a binary fit will be affected, as these are critically dependent on the shape and position of the anomaly.

Ultimately blending may have a positive influence on planet detection. This cannot be seen by the way that it affects a given light curve, but is a result of the distribution of detected events. As a blended event has a lower amplification than the comparable event without blending, the amplification distribution (if the effect of blending is ignored) of events that are currently being detected may be wrong. If a significant portion of these events are blended, their impact parameters, b are smaller than they seem when blending is ignored. In 5.1.3 below, it is shown that planet detection probability is a very strong function of u, so that a smaller value of b should yield more detections.

Luminous lenses as a source of blending are expected to lower the total optical depth by approximately 10% from the expected value in the absence of blending [Lee & Han 1997]. This low number is attributed to the fact that most source stars currently being monitored

are very bright, and that luminous lenses contribute more to blending when they are closer to the observer. However, such Galactic disk lenses contribute little to the optical depth due to their smaller probability of affecting a distant source star.

Other sources of unlensed flux include unresolved background stars and luminous companions to source stars. If a faint unresolved star is close enough to a resolved star, both may be lensed simultaneously, but the event will be attributed to the brighter star. This effect has been investigated [Alard 1997] and it is calculated to be very significant for short duration events. It may also be confused with lensing of brown dwarfs. The additional overall contribution to the optical depth is found to be highly significant and could explain the large optical depth seen for turn-off stars towards the Bulge. Blending due to the multiplicity of the source star is currently an open question. For a certain range of projected separation between a source star and a companion, both may be lensed in turn, leading to a characteristic double-peaked binary source light curve.

There are several ways to detect or measure the effects of blending. Breaking the degeneracy introduced by blending by photometric methods alone has been discussed in detail [Wozniak & Paczynski 1997] for the single lens case. A promising possibility for measuring the blending factor is to use chromatic effects that are introduced during the course of a blended event. An SL event is perfectly achromatic. When there is an unlensed component, it will be more pronounced at low amplification, while the lensed source light will form a larger fraction of the total flux at higher amplification. If the lensed and unlensed components have different colours, due to a luminous lens of a different spectral type, for example, this colour shift may be measurable. The amount of microlensing events with measurable colour-shift is estimated to be of the order of 1 in 10 [Kamionkowski 1995], but the estimate is highly dependent on the limiting magnitude of microlensing surveys, as well as other uncertain quantities such as the mass function below solar mass. If chromatic effects are measurable, however, they may help to break the degeneracy between the three physical parameters of a microlensing event: the projected transverse speed, distance to the lens and mass of the lens. Microlensing surveys and follow-up are conducted for the most part in two bands, so limited colour information is available. Spectra may also be obtained at low amplification and at peak to constrain or measure chromatic effects [Di Stefano & Esin 1995].

If significant blending is present, the fraction of blended events may be inferred statistically. The statistical effect will be most apparent in the distribution of event time scales, t_E. If blending is neglected in estimates of t_E, the distribution is expected to shift to shorter time scales. Furthermore the optical depth measured for the general lens population should

be smaller than that measured for a sample of events with giant sources only, where blending should be negligible [Di Stefano & Esin 1995]. Note that this effect works against that discussed above.

Other methods for identifying blended events include centroid shift and using the resolving power of the HST as suggested by Han in [Han 1997]. At least 15 detected events from the OGLE-1 database have been scrutinised for centroid shifts [Goldberg & Wozniak 1997]. Of these, 7 showed a significant centroid shift, indicating that perhaps half of microlensing events towards the Galactic Bulge are significantly blended, although the astrometric shift has not been used to attempt a quantification of blending to date.

Currently there are no estimates available for an expected distribution of f as a function of source magnitude, lens distance or any other parameter, that takes all the possible sources of blending mentioned above into account. A simple model that follows the expected trend is adopted and discussed below.

2.5 The resolved source effect

The point source approximation must fail at very high amplification as it predicts infinite magnification for sources and lenses that are perfectly aligned, or if the source is positioned on any caustic curve in the case of binary lenses. The failure is a result of the finite angular radius of the source star, which is in fact resolved at very high amplification. It is a geometrical effect.

If the ratio of the angular source star radius to the Einstein ring radius is large (of the order of 10^{-3} or larger) all the light from the source is not concentrated in one point. Rather, it takes up some finite area projected onto the lens plane, so that even if some part of the source profile lies on a caustic curve and should be magnified enormously, only a small portion of the luminous disk of the star is being magnified at any one time.

The most important consequence of a resolved source in the single lens case is that the expected amplification close to peak is reduced. This effect is illustrated in Fig. 2.7.

Where a caustic crossing during a binary lensing event causes a jump in amplification to infinity in the point source approximation, the rise will be more gradual and the peak finite as an infinitesimal part of the resolved source lies on the caustic curve at any given time. A binary lens may also lead to areas of reduced magnification, seen as a drop in amplitude compared to the expected single lens light curve. These drops will be less pronounced if the source is resolved. The effect is more severe for smaller caustic areas, where areas of increased

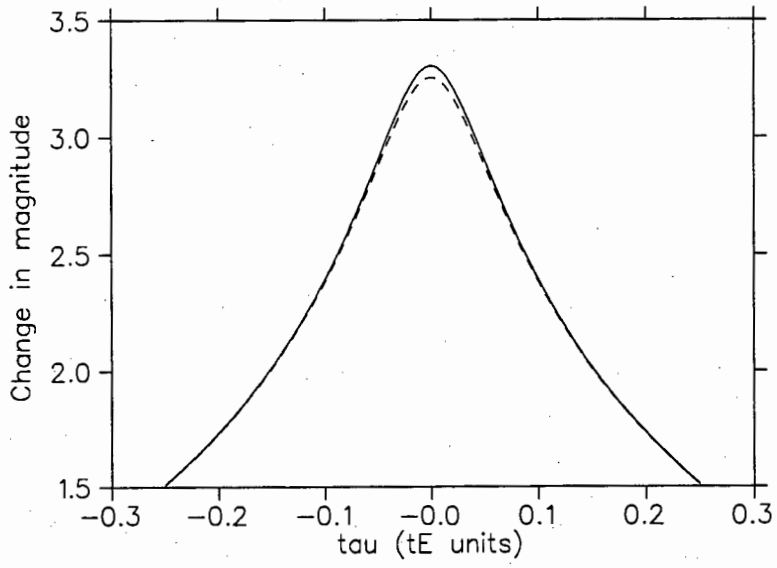

Figure 2.7: The effect of a resolved source on a single lens light curve. The solid curve is for a point source with impact parameter $b = 0.05$, while the dashed curve is the same event with $r_s = 0.03$.

amplification and reduced amplification are close together. A resolved source may cover both such areas simultaneously, canceling the perturbation completely. As the caustic area of a planet scales roughly with the square root of the ratio of the planet's mass to that of the primary, the resolved source effect places a limit on the minimum mass ratio that may be detected by single band photometry.

Depending on the details of the caustic shape and the accuracy of the photometry, a resolved source may also improve the chances of detecting a planetary perturbation slightly. This happens because the perturbation is broadened by roughly one source diameter. In cases where the center of a source crosses over a caustic curve, a resolved source will start crossing earlier and end the crossing later, even though the rise and fall in amplification will be more gradual. Some caustic curves that may have been missed entirely by a point source could also be grazed by the outer parts of the resolved source, leading to more detections.

The ratio of the angular source radius to the angular Einstein radius, r_s is given by

$$r_s = \frac{\theta_{source}}{\theta_{r_E}} = \frac{R_s D_l}{r_E D_s} \tag{2.38}$$

where R_S is the absolute source radius, r_E is the absolute Einstein ring radius, and D_l and D_s are the distances to the lens and source plane respectively.

Broadly speaking, the amplification of a resolved source is calculated by integrating the

flux over either the source profile in the source plane, or the image profiles in the image plane. For a single point mass lens, the total magnification of an arbitrarily shaped source, integrating in the source plane, is given by

$$A_{rs} = \int_0^{2\pi} \int_0^{\infty} p\,(r,\theta)\, A\left(\sqrt{u_0^2 - 2ru_0\cos\theta + r^2}\right) r dr d\theta \tag{2.39}$$

u_0 is the impact parameter, and r the distance from the center of the source measured in Einstein radii. $p(r,\theta)$ is the brightness profile of the source. $A(u)$ is the magnification as a function of impact parameter for an SL event, i.e. point source point mass lens, given in Eq. 2.10. A in 2.39 must be normalized so that $A_{rs} = 1$ for $A = 1$.

For a radially symmetric source, the integral can be performed over the angle and expressed by way of elliptic integrals. If the source profile is approximated by a constant surface brightness disk, A_{rs} may be calculated analytically. With limb-darkened disks, the integral cannot be evaluated analytically for an arbitrary impact parameter. Binary lenses in particular, require a numerical approach to the resolved source effect.

In spite of the negative aspects of resolving the source, it may in fact be advantageous to focus follow-up observations on such events. In broad terms, the canceling of planetary anomalies becomes significant for mass ratios $q = 10^{-4}$ or smaller. That means that detection of Jupiters may not be negatively affected.

If the sampling of the light curve is dense enough to fit the resolved source size accurately, it constitutes a direct measurement of r_s, i.e. the ratio of the angular source radius to the angular Einstein radius of the primary. As the angular radius of the source star can be gauged by conventional methods such as spectral typing, we have a measurement of the angular Einstein radius. In addition,

$$v_t = \frac{r_E}{t_E} \tag{2.40}$$

where t_E is the Einstein radius crossing time from a fit to the light curve.With the source size measured, we have two constraints on the three physical microlensing parameters: D_l, distance to the source, v_t, relative proper motion between source and lens, and m, mass of the lens, as opposed to the one constraint only that may be measured from an SL event.

In the first case of an accurate measurement of the resolved source effect [Alcock et al. 1997b], the above constraints were used to derive relative proper motion to within 13% (error dominated by measurement of source radius), lens mass to within about a factor of two with 80% probability and lens distance to within about 30%. There was some degeneracy in the inter-

pretation, depending on whether the source star was on the main sequence or an M4 III star on the far side of the bulge. Spectroscopic data favours the giant star interpretation.

Accurate sampling of resolved source effects also allows a limb-darkened model of the source to be fit to the data. The source profile is convolved with the SL light curve and may be measurable if sampling is 'good enough'. One of the goals of this investigation is to determine which effects are measurable with a given sampling rate but a successful fit to observations for limb-darkening coefficients has been carried out at least once [Albrow et al. 1997]. In resolved source calculations in this project a limb profile

$$\frac{I(\theta)}{I(0)} = 1 - 0.6\,(1 - \cos\theta) \tag{2.41}$$

is assumed.

2.6 Constraints to physical parameters from microlensing anomalies

The resolved source effect and the parallax effect both yield an extra constraint on the physical parameters m, v_t and x. From Eq. 2.38, $r_s = \frac{R_s x}{r_E}$, with R_s being the physical source radius and r_E the physical Einstein radius of the lens. As $r_E = t_E v_t$ (2.40), we have

$$v_t = \frac{x R_s}{t_E r_s} \tag{2.42}$$

r_s may be determined from fits to the affected light curve and t_E is easily determined in most cases. If R_s is estimated from a spectral study of the source star, Eq. 2.42 is an additional equation relating v_t and x with no unknowns.

The constraint that may be derived from a fit to a parallax event is obtained from the definition of ρ in Eq. 2.32. Substituting Eq. 2.40 and solving for v_t, one finds

$$v_t = a_{semi}\frac{1 - x}{t_E \rho} \tag{2.43}$$

Determining both r_s and ρ in a single microlensing event would enable a unique solution for x, v_t and m. Unfortunately these anomalies very rarely occur in conjunction, as they are both seldom observed and affect events within a small range of parameter space only.

Chapter 3

Models for the distribution of microlensing parameters in detected events and observational techniques

3.1 Distribution of parameters

To determine the range in parameter space in which a reasonably accurate measurement of parallax parameters can be obtained and to estimate how often anomalies occur, a model is required to simulate the microlensing events that are currently being detected towards the Bulge. The model should yield distributions for all the microlensing parameters, which are in general, not independent. These distributions should also be compared to the distributions of the current event data.

3.1.1 Model justification

The optical depth, mass spectrum, t_E distribution and other microlensing measurables can be predicted from values like the mass number density, $\frac{dn}{dm}$ and the mass density functions for sources and lenses, ρ_s and ρ_l. These values are all subject to uncertainties, leading to a large variety of Galactic Disk and Bulge models having been adopted in the past. Some of these include a central hole in the disk, and various inclination angles for the Galactic Bar when its existence is taken into account. In addition, the majority of models used for estimating microlensing distributions are simplifications.

The approach taken in this project was to adopt a model consistent with the latest avail-

able data on Galactic structure and to adjust the mass distribution to fit the latest observed microlensing results: t_E and m_0 distributions to fit the MACHO collaboration results [Alcock et al. 1997a] and recent observations towards Baade's Window for the r_s distribution [Witt 1995]. Where observational results were not available, models were adopted from the literature: an f distribution based on simple logic and theoretical amplification bias [Han 1997]. The distribution of the remaining parameters, t_p, b, ρ, and ψ are derived from first principles.

The mass density function of lensing objects has been the subject of intense debate since the publication of the first observational results for the optical depth of microlensing toward the Bulge. The most current data from the MACHO collaboration [Alcock et al. 1997a] yield $\tau = 3.9^{+1.8}_{-1.2} \times 10^{-6}$ from a sample of thirteen clump giants. This value is in agreement with the lower limit of $\tau \geq 3.3^{+1.2}_{-1.2} \times 10^{-6}$ obtained by the OGLE collaboration [Udalski et al. 1994a]. The MACHO value is greater than predictions made prior to the first results by a factor of three, roughly $\tau = 1.0$ - 1.5×10^{-6} [Griest et al. 1991],[Paczynski 1991],[Kiraga & Paczyski 1994].

This project adopted the mass density as a function of source and lens distance from the literature [Zhao et al. 1996]. This mass density, velocity distribution and mass function taken together predict 45 events for MACHO and 9 for OGLE, which compares very well with the 43-45 and 12 events observed respectively. Although it also reproduces the observed t_E distribution, the model predicts a total optical depth of $\tau = 1.5 \times 10^{-6}$ for all the MACHO fields together, assuming that clump giants have the same distribution and detection efficiency as the rest of the stellar population.

The algorithm for producing random microlensing events with the correct observed distribution and the resulting distributions themselves are discussed below in 4.1.1.

3.1.2 Microlensing model

The point source and single lens model may be fitted to a light curve to yield four parameters. These parameters are

1. m_0, the apparent magnitude of the source
2. b, the impact parameter
3. t_m, the time of maximum amplification, and
4. t_E, the Einstein radius crossing time

With parallax included, the parameters ρ and ψ defined above are added to the list.

For resolved source stars, the parameter r_s is included, and the blending effect is described by f, bringing the number of model parameters for a single lens to eight. Note that only t_E and ρ impart any information about the nature of the lens.

The impact parameter b, measured in Einstein radii, is assumed to be flatly distributed from 0 to the assumed maximum detection radius at $b = 1r_E$, corresponding to an amplification of 1.34. This follows from the geometrical argument that all impact parameters are equally likely to occur. The actual distribution of b for the MACHO events to date [Alcock et al. 1997a] agrees well with this prediction. It should be kept in mind that the MACHO t_E distribution is multiplied by their detection efficiency. For the model used in this project, the absolute detection efficiency is not a factor since distributions are the only interest. The efficiency is a function of t_E that falls off towards very short timescales. This effect will be neglected in the microlensing model because it is small and very short events will not play a large role in the measurement of anomalies in any case.

The time of maximum amplification, t_m, is also assumed to be distributed evenly, with microlensing events equally likely to occur at any time.

Although the t_E distribution for observed events is known (within error), the characteristics of the lens and the geometry of the event can only be extracted from this distribution by statistical means and by way of modeling. As shown in Eq. 2.40, t_E is dependent on the relative transverse velocity of the lens and source, v_t, and on the Einstein radius of the source. The lens and source distance, D_l and D_s, are tied up with the Einstein radius along with the mass of the lens, m. If x is the ratio of D_l to D_s ($x \leq 1$). r_E is given by Eq. 2.4.

To obtain distributions of the parameters of detectable events, and therefore a realistic model event population, distributions of the underlying parameters, D_s, D_l, m and v_t are required. In general, the distributions for lensing events are different than those for the stellar population. The source distance D_s, for example, does not follow the number distribution of stars toward the Galactic Bulge. That is because source stars and lenses with a certain geometry are favoured as microlensing candidates, and because lensing of a brighter source is more likely to be detected than lensing of a faint source. Distributions of parameters of lensing events can be derived from the total event rate, Γ. According to Paczynski (1991) Eq. 14, the average time interval between microlensing events is

$$\langle \Delta t \rangle = \frac{\pi t_E}{2\tau} \tag{3.1}$$

where τ in this case is the optical depth to microlensing. τ is defined as the probability that a certain star is within the Einstein radius of any of the lenses. For stars (sources) at the

distance D_s to $D_s + dD_s$, and lenses at the distance D_l to $D_l + dD_l$, $\tau(D_s)$ is given by

$$\tau(D_s) = \pi \int_0^{D_s} \rho_l r_E^2 (D_l, D_s)\, dD_l$$

$$= \frac{4\pi G}{c^2} \int_0^{D_s} \rho_l \frac{D_l (D_s - D_l)}{D_s} dD_l \tag{3.2}$$

It is assumed that the fraction of detectable stars varies as the inverse square of the source distance, canceling the effect that the growing volume element $D_s^2 dD_s$ has on the number of detectable stars. The number of detectable stars in the range D_s to $D_s + dD_s$ is then given by

$$dn(D_s) = k\rho_s dD_s \tag{3.3}$$

k is a constant. The event rate is defined as

$$\Gamma = \langle \Delta t \rangle^{-1} = \frac{2\tau}{\pi t_E} \tag{3.4}$$

Incorporating Eqs. 3.1 to 3.4, Γ is given by the integral

$$\Gamma = \frac{\frac{4}{c}\sqrt{\frac{G}{m}} \int_0^\infty \left(\int_0^{D_s} \rho_{l,s} v_t (D_l, D_s) \sqrt{\frac{D_l (D_s - D_l)}{D_s}} dD_l \right) \rho_{l,s} dD_s}{\int_0^\infty \rho_{l,s} dD_s} \tag{3.5}$$

where it is assumed that all lenses have identical mass m. The determination of the lens mass distribution is one of the goals of current microlensing experiments. When the total number and the t_E distribution of the first 55 Bulge microlensing events reported by the MACHO and OGLE collaborations are compared to those predicted by various models of the Bulge and Disk, a Salpeter mass function,

$$\frac{dn}{dm} \propto m^{-2.25} \tag{3.6}$$

with $0.08 M_\odot < m < 0.6 M_\odot$ is the best fit to the data [Zhao et al. 1996]. With this mass function adopted for the lens mass function, the differential microlensing rate is proportional to

$$d\Gamma \propto m^{(0.5-2.25)} \rho_l D_l \rho_s D_s \langle v_t (D_s, D_l) \rangle \sqrt{\frac{D_l (D_s - D_l)}{D_s}} dm dD_l dD_s \tag{3.7}$$

A tabulation of $\langle v_t \rangle$ and ρ_l as a function of distance toward Baade's Window in the Galactic Bulge based on the surface light map from COBE and radial velocities of bulge stars is used

in this project [Zhao et al. 1996], [Zhao 1996]. The lens population mass density is assumed to be proportional to that of the source population, thus $\rho_l \propto \rho_s$. Note that $\langle v_t(D_s, D_l)\rangle$, the mean relative speed of lens and source projected to 8 kpc, is in fact an integral over two 2D Boltzmann distributions for the relative mean speed, where the Boltzmann distributions are themselves functions of D_s and D_l,

$$f(v_t)\,dv_t = \frac{v_t}{2\mu^2} e^{-\left(\frac{v_t^2}{4\mu^2}\right)} dv_t \tag{3.8}$$

and

$$\sqrt{\pi}\mu = \int_0^\infty v_t f(v_t)\,dv_t = \langle v_t \rangle \tag{3.9}$$

We will take the following microlensing scenarios into account:

1. Main sequence turn off sources and lenses in the Bulge (BMS)
2. Clump giant sources in the Bulge and lenses in the Bulge (BCG)
3. Main sequence turn off sources in the Bulge and lenses in the Disk (DMS)
4. Clump giant sources in the Bulge and lenses in the Disk (DCG)

The stellar type of the source star has a direct effect on two of the microlensing parameters: r_s, the source star radius projected onto the lens plane in units of r_E; and m_0, the apparent source magnitude. Of the first 45 MACHO events [Alcock et al. 1997a], 13 sources were clump giants within the Bulge. The distribution in unlensed source magnitude for the 45 source stars is compared to the clump giant distribution in Fig. 3.1. The value of m_0 is assumed to be normally distributed, fit to the sample of 13 clump giants, with mean $V = 17.5$ and $\sigma(V) = 0.64$ for BCG events. In the BMS case, a mean of $V = 18.7$ with $\sigma(V) = 1.23$ is obtained for the MACHO events and adopted as the source distribution for simulation purposes.

For the source radius, another normal distribution is assumed. For main sequence turn off sources a mean of $3R_\odot$with $\sigma = 1R_\odot$ and for clump giant stars a mean of $13R_\odot$, $\sigma = 1R_\odot$ is assumed. The source radius in r_E units, projected onto the lens plane is given by Eq. 2.38.

The situation for lenses in the Disk is somewhat simpler. The Disk is modeled as a constant stellar mass density of $\rho_l = 0.1R_\odot pc^{-3}$ out to $4kpc$ with a central hole, following a simple model [Kiraga & Paczyski 1994]. The uncertainty in current models of the Disk are so large that this

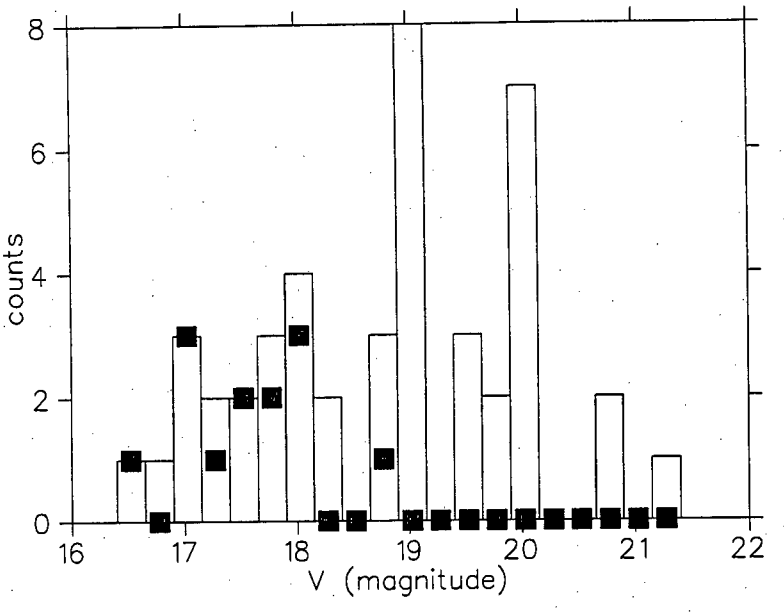

Figure 3.1: The distribution of MACHO source apparent magnitudes from [Alcock et al. 1997a]. Unfilled bars indicate the total distribution, while solid blocks indicate the distribution of clump giants.

model is quite acceptable. For the relative velocity a Boltzmann distribution with a dispersion of 100 $km.s^{-1}$ is used.

The model adopted for the blending parameter, f, was based on simple logic. No distributions are available in the literature and the actual distribution has not been measured in the majority of microlensing events detected so far. The model assumes that f is distributed as

$$f = \frac{l}{l+k} \tag{3.10}$$

where l is the luminosity of the source star, and k is a constant, chosen to be 5.0×10^{-9} on a scale where a magnitude of zero corresponds to a luminosity of 1. A random fluctuation from this distribution is included by adding a value from a normal distribution with standard deviation of 0.2 to the value of f. Values of $0 < f < 1$ are assumed.

Eq. 3.10 incorporates the following principles of blending:

1. All stars are blended.

2. Very bright stars are not expected to be blended by much.

3. Very faint stars should almost always be heavily blended.

4. There is a constant luminous background, be it from unresolved stars or from an averaged lens luminosity.

3.2 Detection criteria and sampling of events to find planetary perturbations

Estimation of realistic detection efficiency requires a model of the observational capabilities of microlensing survey and follow up groups. To model various detection strategies, the following variables were used:

1. N, the number of sampled data points per t_E, Einstein radius crossing time.
2. c, the magnitude difference cutoff. If the absolute value of the difference between the single lens magnitude and the binary lens magnitude is larger than c, the data point is considered anomalous.
3. e, factor by which the sampling rate is increased after two consecutive anomalous points have been observed, until either a detection occurs, or a non-anomalous point is observed. This models the observer's capability to react to anomalies. For most survey groups, the value of e is zero, i.e. no reaction to observed anomalies due to the survey nature of the search. If an anomaly is detected, the follow up groups are alerted.
4. R_c, the maximum radius (in r_E) from the primary lens where events are sampled.
5. h_c, the minimum number of consecutive anomalous points required to ensure a detection.
6. Cost, the total number of data points that are taken, following any given strategy with a set of these parameters.
7. P_d, the percentage of all possible light curves through the area with radius R_c centered on the origin, that yield planetary anomaly detections. This number is referred to as "detection probability".

The variables defined above allow an analysis of the probable success of an observing strategy vs. the required observing time "cost".

The actual detection efficiency for a certain geometry and observing strategy is determined by calculating a magnification map with binary lens parameters a and q (projected binary

separation and mass ratio). This map is convolved with a resolved, limb-darkerned source profile of radius r_s, and blending is calculated (parameter f). After the entire process is repeated for a single lens with identical r_s and f , positioned at the location of the primary lens, the difference map in units of magnitude is constructed.

Each point in the difference map is subjected to the detection criteria above, and checked to see whether it would fall on a sampled light curve with sampling frequency N. A full description of the algorithms and numerical processes involved is given in 4.2.4, while the sample of microlensing parameters and model parameters for which detection rates were calculated in the original "survey" calculation are:

a	0.2, 0.4, 0.5, 0.6, 0.7, 0.8, 0.9, 1.0, 1.1, 1.2, 1.3, 1.4, 1.5, 1.6, 2.0, 3.5, 5.0
q	10^{-3}, 10^{-4}, 10^{-5}, 10^{-6}
r_s	0.006, 0.01, 0.03
f	1.0, 0.75, 0.5

More parameters were included in the list for specific plots below.

The actual criteria for planet detection are largely subjective as can be seen from the four different approaches taken previously in the literature discussed above. As a detection criterion in this work, the absolute value of the magnitude difference between the theoretical SL curve and the observed light curve is required to be above the threshold c for h_c consecutive points. As an example, for typical PLANET photometry with precision around 1%, a 2% anomaly would correspond to a perturbation from the Paczynski light curve at about the 2-σ level. Thus the probability of four points differing by this amount or more by chance is of the order 1 in 10000. The anomalous points are required to occur consecutively, to lower the chance of a false positive, and the criterion is based on the fact that planetary perturbations are essentially localised to a small area of the light curve.

3.3 Detection criteria and sampling for non-binary anomalies

As noted above, binary light curves and parallax affected light curves were considered separately. For parallax light curves, a different set of detection criteria are required, as the difference method applied to binary lenses does not apply here. The reason is that a parallax

event is not merely a single lens event with a well-defined local perturbation as in the case for planetary system anomalies. Parallax affects the entire light curve, and may cause asymmetry and peak shifts.

To determine how often parallax will be detected, it is preferable to resort to the error analysis of a fitting procedure. In practice, light curves are fitted for microlensing parameters using a χ^2 criterion. Under certain assumptions about the nature of the noise in the data, the pivots of the covariance matrix may be used to determine the uncertainty in any of the fit parameters. If the percentage error in a parameter is below a certain threshold, that parameter is considered to be measurable in a certain light curve. This line of reasoning has been applied in a recent paper [Buchalter & Kamionkowski 1997] to estimate the measurability of parallax. Another similar method [Wozniak & Paczynski 1997] has been applied to estimate the effects of blending.

For this project, a fit parameter is considered measurable if it can be determined to within a formal error of 50% with 95% confidence.

3.3.1 Use of the covariance matrix

The covariance matrix for a set of N data points fit to a theoretical curve with k parameters is easily calculated [Press et al. 1992]. If $[\alpha]$ is the matrix

$$\alpha_{kl} = \sum_{i=1}^{N} \frac{1}{\sigma_i^2} \frac{\partial y\left(x_i; \vec{a}\right)}{\partial a_k} \frac{\partial y\left(x_i; \vec{a}\right)}{\partial a_l} \tag{3.11}$$

the covariance matrix $[C]$ is given by the matrix inverse of $[\alpha]$. The relation between the covariance matrix and the formal error in a fit parameter, is

$$\Delta a_i = \pm\sqrt{\Delta\chi^2}\sqrt{C_{ii}} \tag{3.12}$$

A $\Delta\chi^2$ of one corresponds to a confidence level of 1-σ, i.e. $\Delta\chi^2 = 4$ corresponds to 95.1% confidence, and $\Delta\chi^2 = 9$ to 99% confidence.

Eq. 3.12 is valid only if the errors on data are normally distributed. In actual fact, noise on current observed microlensing light curves is not normally distributed, but suffers from slightly larger "tails". Nonetheless, it is an acceptable approximation and normally distributed noise will be assumed.

3.4 The model for sampling of non-binary events

The same sampling model as that used for binary events is adopted for non-binary events, except that it is assumed that there is no increase in data density during the measurement of non-binary anomalies because the parallax and blending effects are essentially present for the duration of the curve. Resolved source anomalies, however, are expected to be localized to areas of highest amplification on a given light curve, and only in high amplification light curves. Therefore some increase in sampling around the peaks of likely curves can be expected from follow up groups.

For binary events a magnitude difference was used as detection criterion. Depending on an observing group's photometric precision or the source magnitude of the event, different values of the cutoff c, may be chosen to simulate detections at different confidence levels. For non-binary anomalous events, we are also interested in measuring the percentage of the total events observed in which these anomalies will be measurable.

It is not assumed that the photometric accuracy improves with increasing amplification. The reason for this counter-intuitive assumption is that the main cause of noise in microlensing light curves towards the Bulge is crowding, not photon noise, and this does not necessarily depend on brightness, but more on observational effects like seeing. Noise from these effects does in fact show a weak trend with source magnitude in some events, but most follow-up groups adjust their exposure time for constant accuracy at high amplification to save integration time.

The parameters used to model the observation of parallax, blending and finite source size anomalies are

1. N, the number of sampling points per t_E, Einstein radius crossing time.
2. c, the average standard deviation in magnitude of the observations
3. R_c, the maximum radius (in r_E) from the lens where events are sampled.
4. Cost, the total number of data points that are taken, when following any given strategy with a set of the above three parameters.

Chapter 4

Calculations

Numerical methods and algorithms are discussed in this chapter. All simulations were performed in the Linux environment, running on a variety of PC's from 120 MHz 686's to 400 MHz Pentium II's. The code for most algorithms was written in C, and large sets of operations were performed using Linux scripts. The calculation of an entire set of results with parameters similar to those in 3.2, from constructing the difference maps to running the detection routine takes roughly five days on a 400 MHz Pentium II PC.

The philosophy behind the software was to create a "toolbox" for microlensing calculations. This modular approach allowed calculations to be done in a flexible fashion. For example each operation on a magnification map, such as resolved source convolution or calculating the effect of blending, could be performed independently, and results extracted when needed. This made making adjustments to the calculation process easy.

All data storage was made to be file-based as opposed to memory-based. Using this approach, the resolution of the calculations were not limited by memory requirements, but rather by the size of the hard disk (typically a few gigabytes) and the computation time. Conventional memory management would not have allowed computations on maps with more than about 10^6 data points (250 points per r_E on a 4x4 r_E map) on a typical PC.

The final version of the software comes to just more than 10000 lines of code including blank lines, comments and some commercially available numerical recipes and is available on request from the author via e-mail to the address pierre@saao.ac.za.

4.1 Single Lens light curves

Due to the fact that most of the calculations for a single lens light curve are analytical in nature, it is straight forward to obtain a light curve for such an event. To generate a sample of light curves representative of the detected event population, the method described in 3.1 may be used, with an appropriate random number generation method.

4.1.1 Random generation of parameters

In all cases where random numbers with a certain distribution were required, the rejection method [Press et al. 1992] was used. The following is a simple algorithm for generation of parameters based on the model distributions discussed in 3.1:

1. Based on the MACHO statistics, 30% of events are chosen to have Bulge Giant sources.

2. The mass of the lens is chosen from the distribution of Eq. 3.6.

3. A random distance to the lens, D_l, and source, D_s ($D_s > D_l$) is chosen. The mass density at the positions of lens and source, and the mean relative lens speed are linearly interpolated from the model adopted above (see 3.1) for the random values of D_s and D_l. The probability of this configuration is then calculated by use of Eq. 3.7 and rejected or accepted by comparison to another random value from a flat distribution. This is just the well-known Monte Carlo method, used to find values with a certain distribution that are dependent on one another.

4. The actual relative speed for the event is obtained from the 2-D Boltzmann distribution of Eq. 3.8, using the mean speed obtained above.

5. The absolute source radius is obtained from a Gaussian distribution, based only on whether the source is a clump giant or main sequence turn off star, as determined above. For a main sequence turn off source a Gaussian with mean 3 $R_\odot$ and dispersion 1 $R_\odot$ is used. For Clump giants, the mean is 13 $R_\odot$ with a dispersion of 1 $R_\odot$. The apparent magnitudes are also Gaussians, with mean $V = 18.7, \sigma = 1.23$ for main sequence turn off and mean $V = 17.5, \sigma = 0.64$ for clump giants. The apparent magnitudes are based on Gaussian fits to the 13 events identified by MACHO as clump giants out of their sample of 45 events [Alcock et al. 1997a]. The apparent magnitude and absolute source radius are independent in this model. The uncertainties of Bulge models are great enough to

make the dependence of apparent magnitude on source radius within the two categories of source stars unimportant by comparison.

6. The blending parameter is chosen from one of the blending distribution models discussed in section 3.1.

7. t_m is chosen to be zero, while t_p, the time of Earth's perihelion, is randomly selected from a flat distribution covering one year. The parallax parameter ψ is also chosen from a flat distribution as is the impact parameter, b, with $|b| < 1$.

8. The microlensing parameters t_E, ρ and r_s of the event that are dependent on the physical parameters, D_s, D_l, m and v_t are calculated using the formulae from chapter 2.

All the parameters for the event are now known, and this event has a probability of occurrence that should agree with the observed MACHO t_E distribution.

4.1.2 Calculating amplification

The point source amplification is easily calculated from the source position, using Eq. 2.10, after the parallax effect is introduced by perturbing the linear path of the source across the lens plane (2.22 to 2.24).

The next anomaly to include after the point source amplification has been calculated, is the resolved source effect. As noted above, the finite source amplification cannot be calculated analytically in general. For single lenses the numerical calculation is simple. There are several approaches, one of which is to evaluate the integral in Eq. 2.39 numerically. In this work an even simpler approach was followed. The amplification of a number of point sources evenly distributed over the source profile is calculated analytically and then averaged. Limb darkening of the source is included by working out the distance from the center of the source to each point and applying Eq. 2.41.

The accuracy of the calculation can be improved by increasing the density of points in the grid covering the source at the expense of computing time. See chapter 6 for a discussion on the size of the numerical errors.

The last anomaly we consider, blending of light, is included after the finite source amplification is calculated. This is done by applying Eq. 2.35 to the finite source amplification.

The final amplification obtained by following the above steps is called A_{obs}, the observed amplification. To convert it to the magnitude scale

$$m = -2.5 \log A_{obs} + m_0 \tag{4.1}$$

4.2 Calculation of binary lens light curves

4.2.1 Planet parameters

The approach taken to simulate binary events (more specifically primaries with planets) is different from that taken for the single lens calculations. The parameter space is explored without attempting to model the frequency or distribution of planetary systems, simply because almost nothing is known about extra solar planetary systems at the moment. The planets discovered recently by radial velocity methods [Mayor & Queloz 1995], [Marcy & Butler 1996] serve as a warning that the generic "factor of two" solar system, or Sun and Jupiter model that is normally adopted, e.g. [Bennett & Rhie 1996] may not be representative.

Additional information is available from pulsar planet detections [Wolzczan 1992] but the connection between such extreme systems and planetary systems around main sequence stars is unclear.

4.2.2 Calculating amplification for binaries

One obvious way to calculate the amplification for any given lens position and binary geometry in the point source approximation, is to solve the binary lens equation 2.11 for the source positions. Source positions are then used to calculate the determinant of the Jacobian of the transformation matrix and the reciprocal gives the amplification for each image.

The lens equation can be converted to a fifth degree complex polynomial by taking the conjugate of Eq. 2.11 and replacing for $\overline{z}$. The coefficients are:

$$c_0 = -\zeta a^2 \tag{4.2}$$

$$c_1 = 2\zeta aq + \zeta a^3 - 2\zeta\overline{\zeta}a^2 - qa^2 + 2\zeta a \tag{4.3}$$

$$c_2 = 4\zeta\overline{\zeta}a - \zeta\overline{\zeta}^2 a^2 - \zeta - \zeta q^2 + aq - 2q\zeta + \overline{\zeta}a^2 - qa^2\overline{\zeta} + 2\zeta\overline{\zeta}qa + q^2 a + \zeta\overline{\zeta}a^3 - 2\zeta a^2 - \zeta qa^2 \tag{4.4}$$

$$c_3 = \zeta a - 2a^2\zeta\overline{\zeta} + qa^2 - 2a\overline{\zeta} - 2q\zeta\overline{\zeta} - 2\zeta\overline{\zeta} + aq\zeta + \overline{\zeta}^2 a^2 + 2a\zeta\overline{\zeta}^2 - \overline{\zeta}a^3 \tag{4.5}$$

$$c_4 = q\overline{\zeta} + \overline{\zeta} - \zeta\overline{\zeta}^2 - 2a\overline{\zeta}^2 + 2\overline{\zeta}a^2 + \zeta\overline{\zeta}a - aq \tag{4.6}$$

$$c_5 = -a\overline{\zeta} + \overline{\zeta}^2 \tag{4.7}$$

with

$$\sum_{i=0}^{5} z_i c_i = 0 \tag{4.8}$$

The purpose of transformation to a polynomial is that one may apply Laguerre's method [Press et al. 1992] to solve for all five complex roots uniquely, even though the input "guessed" root is the same, by reducing the order of the polynomial by one with every root found. Without further refinement of the image positions, Laguerre's method gave accurate answers (see chapter 6) for mass ratios in excess of roughly 10^{-3}.

To calculate amplifications for smaller mass ratios, the roots found by Laguerre's method were used as initial guesses for a two-dimensional Newton-Raphson algorithm. With this method accurate roots were obtained for mass ratios above 10^{-7}. Below this value, the N-R routine often converges to the same root for different initial guesses, due to the inaccuracy of the Laguerre roots.

A fifth degree polynomial always has five roots, while the lens equation has three roots for a source outside a caustic area and five for a source crossing a caustic area. Therefore the polynomial yields two spurious solutions that are not solutions of the lens equation itself, when the source is outside of an area enclosed within a caustic curve. All roots of the polynomial must be substituted back into Eq. 2.11 to check whether they are in fact valid image positions before they are passed on to the N-R routine as initial guesses. Substitution into the lens equation also provides a check on the accuracy of the roots (up to machine accuracy) obtained by the numerical methods.

Fig. 4.1 is an example of image profiles obtained from a source profile using this method. The binary parameters are not typical of the parameters investigated in this project as the source radius and mass ratio is larger than typical planetary values, but these values were chosen for illustration purposes. The system shown here has $q = 0.01$, which is in the brown dwarf regime. The projected source radius is 0.1 r_E, about ten times larger than typical.

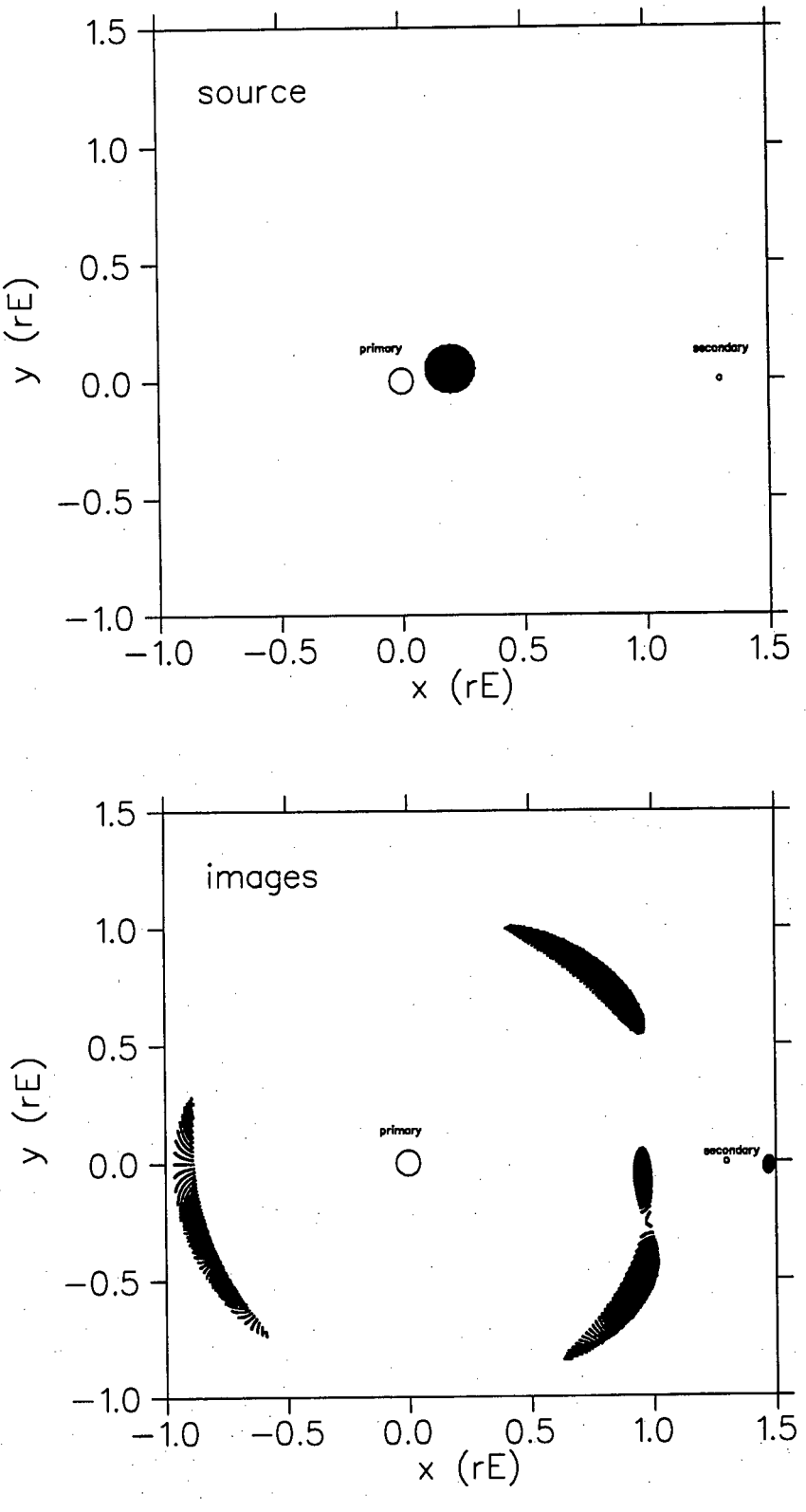

Figure 4.1: An example of image profiles obtained from a source profile.

4.2.3 Introducing resolved source and blending anomalies into planetary light curves

4.2.3.1 Source plane integration

It is considerably more complicated to compute resolved source effects for binary light curves than for single lens curves, as the binary lens equation cannot be solved analytically for a point source, hence one cannot easily use the average of a grid of point sources.

Another obstacle to source profile integration is the highly non-linear nature of the amplification as a function of ζ around caustic curves. For a single lens the only caustic is a point at the origin. For binary lenses, caustic curves and cusps are crossed leading to sudden changes in amplification.

If we consider a resolved source as a grid of point sources, this causes a grid point to be amplified enormously if it happens to fall particularly close to a caustic curve. If the number of points in the grid is too small, the weight of any one point would be too large, and the average amplification of all points would be inaccurate. The net effect is to cause large scatter in the resolved source calculations around caustic crossings. It is advantageous to use as fine a grid of source points as possible to prevent this scatter while still taking computational effort into consideration.

When implementing a source profile integration routine, a check may also be built into the routine to monitor points with unusually large amplification. Such points may be compared with adjacent points in the source plane grid. If the adjacent points have much smaller amplification (a factor of ten is used as a trigger), the anomalous point is calculated using the slower but more accurate image plane integration method, assuming a resolved source size smaller than the spacing of the grid points, for that particular point in the source grid.

4.2.3.2 Image plane integration

An alternative to source profile integration is to integrate the image profiles. A resolved circular source is mapped to its images using Eq. 2.11 whereafter the amplification is given simply by dividing the total area of the images by that of the source. Each point in the image profile integral carries the same weight which avoids the problem of diverging integration values.

There are essentially two approaches to image integration. One is to find the image of the boundary of a source plane contour, whereafter a discretised version of Stokes's theorem is applied to the image contours to determine the total area of the images [Gould & Gaucherel 1996]. Alternatively, image positions can be mapped onto source positions. If an image point is

mapped onto the resolved source profile, it is accepted, weighted for limb-darkening and added into the integration. All positions in the image plane that map onto the source profile must be found, otherwise it is possible to leave an entire image out of the integration leading to an incorrect amplitude. This method appears computationally expensive, but as the lens equation does not need to be solved when mapping from image plane to source plane since each image plane position corresponds to exactly one source plane position, found by substituting z into Eq. 2.11, it is quite practical.

An image integration algorithm:

1. Solve the lens equation once for the position of the center of the source to find a point inside each of the images.

2. Construct an integration grid, working outwards from each of these image positions.

3. Replace each integration point into the Eq. 2.11 to see whether it maps onto the source. If it does, it is added to the integration.

4. If no more points are found to map onto the source, end the integration and divide by the source area to find the amplification.

A method like the one above has been described in the literature [Bennett & Rhie 1996]. It is easy to include limb darkening into the above calculation by determining the distance to the center of the source of each point mapped from the image plane and weighting it according to Eq. 2.41.

Care must be taken not to add the same image points twice, as images may merge or separate depending on source size and position causing integration grids for two images to overlap. The problem is solved by checking which images fall into which integration grids. This information is used to set up a five by five matrix for each image's integration grid that tells which of the other images' grids it contains, as well as a vector that gives the total image area in each integration grid. The linear system is solved numerically and ensures that the redundant image area is dropped from the calculation.

Pixel size in the image integration needs to be rescaled for every source position where amplification is calculated to avoid excessive computing time and to ensure constant precision throughout the calculation of a light curve.

4.2.3.3 Ray shooting

A straight forward but computationally taxing method for calculating the amplification of sources of arbitrary shape is the ray shooting method. The analytical mapping from the image plane to the source plane is used to map a grid of image points onto the source plane. The density of points in the source plane is then directly proportional to the amplification. The results are stable and the density may be convolved with any source shape to obtain resolved source effects. Many points are required to attain accurate results, however, causing this method to be used mostly for small areas around caustic crossings [Wambsganss 1997].

4.2.3.4 Magnification maps

A quick way to obtain resolved source effects is to make a magnification map. Such a map is simply a grid of calculated point source amplifications covering an area in the source plane. These point source amplifications may be converted to finite source amplifications by convolving the map with the resolved source profile. The accuracy of the finite source calculation improves with growing source radius, because the source profile includes more grid points. In addition, for very small sources, the point source grid points themselves will be a good approximation to the actual amplification.

The method used in this work was to calculate a magnification map, using the point source method outlined above:

1. A magnification map with spacing of 100 points per r_E was calculated for a binary lens with projected separation a and mass ratio q. This map was compared at each point to the amplification of a single lens with the mass of the primary. Mass ratios of $q \leq 10^{-3}$ were considered. For mass ratios in this range, the effects of the binary lens may be considered a perturbation on the magnification map of a single lens with mass of the primary only. For larger mass ratios, it becomes increasingly difficult to make a comparison between single lens and binary lens magnification maps. For close binaries with similar masses, a single lens with mass equal to the total mass of the binary system, and located at the center of mass is in closer agreement with the binary system's amplification map than a single lens located at the position of either one. In other words, the binary system must be compared to the closest single lens fit for the binary system if such a comparison is to be made. For smaller mass ratio planets ($q \leq 10^{-3}$) the closest single lens fit is given by a single lens with the mass of the primary, located at the position of the primary.

2. If the difference between the binary and single lens amplification is larger than 0.5%, the position of the grid point is written to a list. The single lens and binary lens point source amplification maps and difference map for a typical set of planetary parameters at this stage of the process (resolution of 100 points per r_E, only anomalous points kept) are shown in Figs. 4.2 and 4.3.

3. The magnification map is refined four times, by halving the spacing of grid points around points in the list from item 2 above. The new points calculated are also compared to the single lens case, and added to the list if their amplification differs by 0.5% or more from the single lens case. After refining, the density of calculated points around anomalies is 1600 points per r_E, or 2.56×10^6 points per r_E^2. For mass ratios larger than $q = 10^{-4}$, only three refinements are made to the original grid, leading to resolution of 800 points per r_E. Above this mass ratio, the magnification map features tend to be coarse enough to be fully resolved with lower resolution, allowing a saving in computation time without penalty. Figs. 4.4 and 4.5 illustrates the refining process up to 800 points per r_E. The highest resolution (1600 points per r_E is not shown due to plotting constraints). High resolution magnification maps were required to ensure accurate results during the convolution of the maps with a resolved source profile. Numerical errors are discussed in chapter 6.

4. The magnification map is convolved with the resolved source profile, and the blending effect is added, as described above. During convolution, the effects of limb-darkening are taken into account, using the limb darkening model from Eq. 2.41. Convolution is performed by multiplying the Fourier transforms of the point source magnification map and the source profile together and taking the inverse Fourier transform to obtain the convolved map. Both the binary lens and single lens magnification maps must be convolved with the source profile to enable the calculation of a difference map. To illustrate the convolution process, Fig. 4.6 shows the original planetary system difference map, the convolved difference map and the map after blending for the example event used above.

5. The final map, in the form of a list of points with amplification differing from the single lens case by more than 0.5%, is divided by the single lens amplification at each point, and converted to the magnitude scale, yielding a difference map in stellar magnitudes.

The magnification map covers an area of 16 r_E^2, that is a 4 r_E by 4 r_E grid centered on the primary. Currently, microlensing events are only detected when they reach a certain

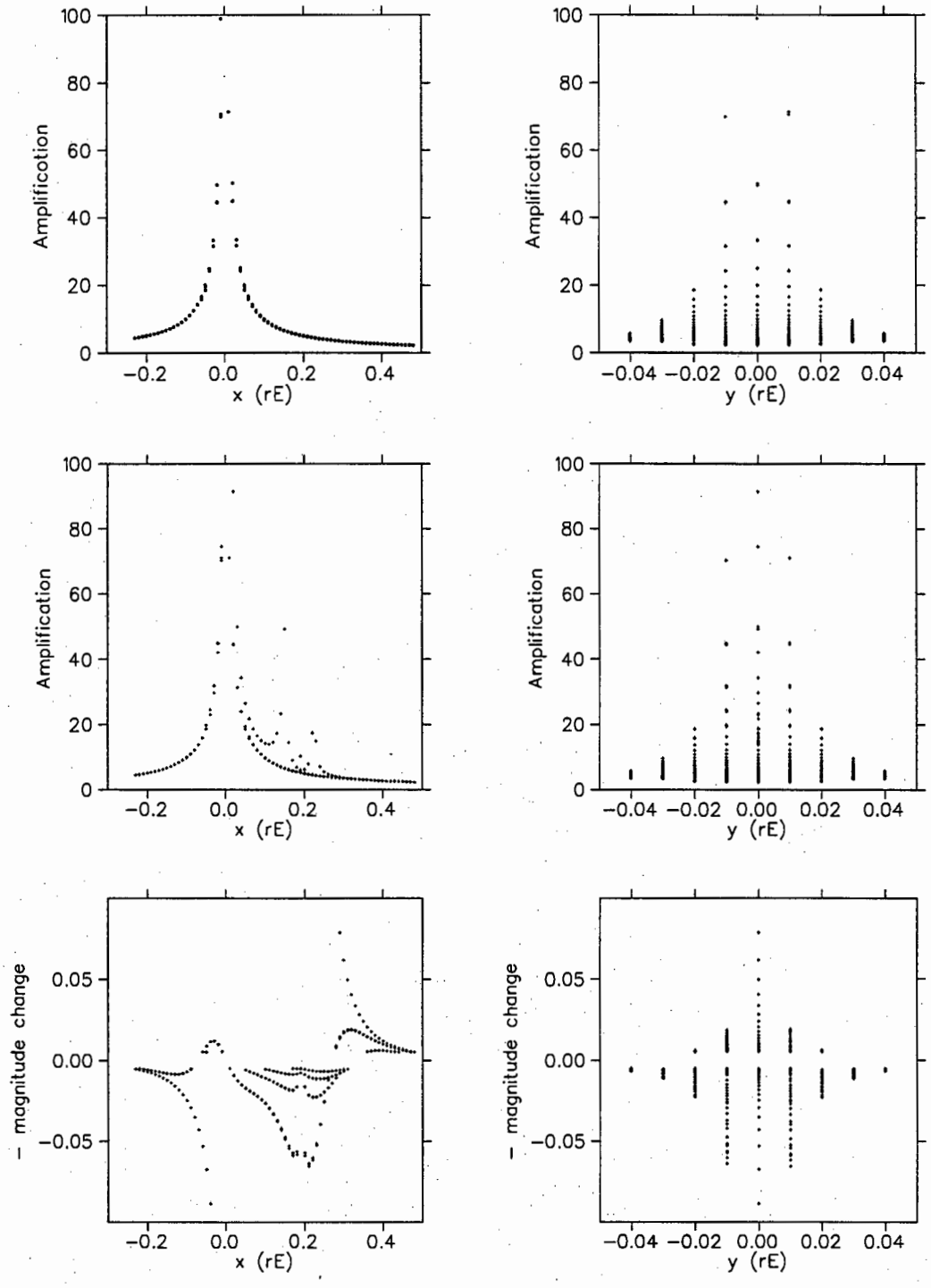

Figure 4.2: x and y profiles of magnification and difference maps at the initial resolution of 100 points per r_E. Only anomalous points are plotted. The top row is the total amplification in the single lens point source case, the middle row is the total amplification in the presence of a planet with $q = 10^{-4}$ at $a = 1.1$ and the bottom row shows the difference between the single and planetary maps in units of negative magnitude (i.e. a positive value is an increase in brightness).

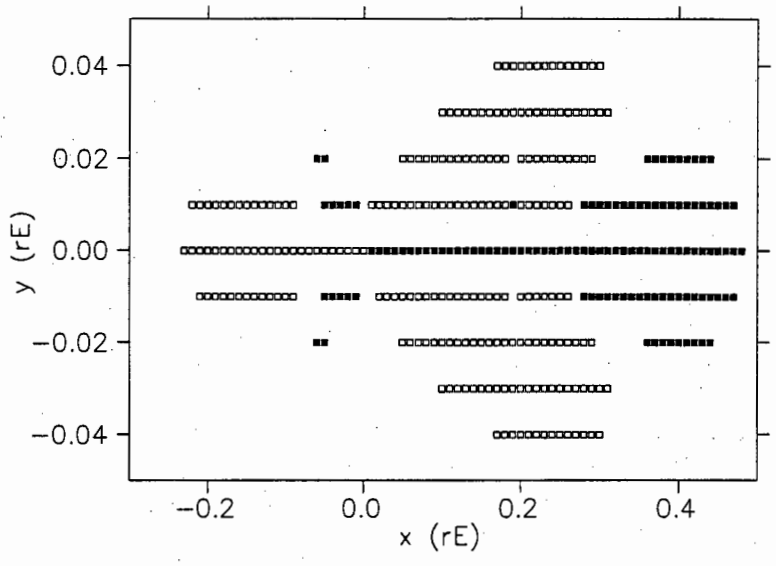

Figure 4.3: The difference map of the event displayed in Fig. 4.2, plotted as a function of source position in the lens plane. Solid blocks are areas of increased magnification above the single lens point source model, and open blocks are points with less magnification. The map is for the preliminary resolution of 100 points per r_E.

minimum amplification threshold. This has traditionally been set at an amplification of 1.34, corresponding to a single point lens with projected source distance of 1 r_E. In practice, the detection threshold depends on various parameters, such as the event length, unlensed magnitude of the source and blending.

Long events, O(100 days) may be detected earlier if they pass the detection criteria set by the survey groups. One such criterion may be a sequence of consecutive rising data points. A long event could pass this cut while still being outside the Einstein ring radius of the lens. Survey groups have the advantage of hindsight, as their coverage extends over the entire duration of the survey: all stars with reasonable photometry have light curves. Follow up groups rely on the real time detection of events, and can only start observations once they have been alerted to the presence of an event by a survey group.

The source magnitude is important due to the effect it has on photometric accuracy. Blended events have a smaller amplification than an unblended event at the same source distance from the lens. Their apparent Einstein ring crossing time, t_{Eapp} is therefore shorter than an unblended event with the same impact parameter and relative velocity, leading to a later detection. The effect of blending does not necessarily imply a lower total detection rate for survey groups, because the very fact that blending is detectable in roughly 50% of microlensing events with complementary methods, i.e. astrometric shifts [Goldberg & Wozniak 1997],

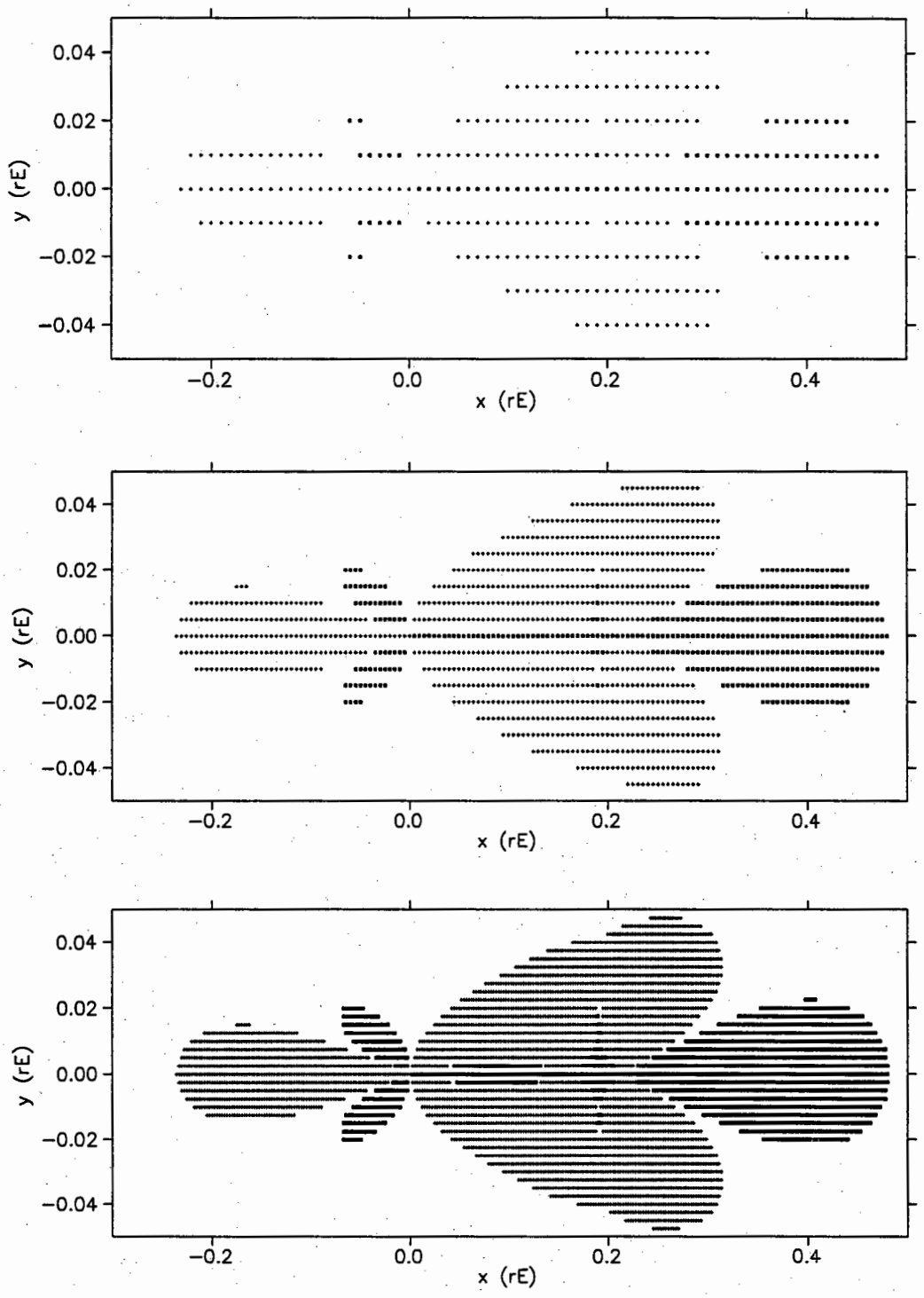

Figure 4.4: The initial difference map and first two refinements of the event displayed in Fig. 4.2, plotted as a function of source position in the lens plane. Solid blocks are areas of increased magnification above the single lens point source model, and plus-signs are points with less magnification. The top map is for the preliminary resolution of 100 points per r_E, the center map for 200 points per r_E and the bottom map for 400 points per r_E.

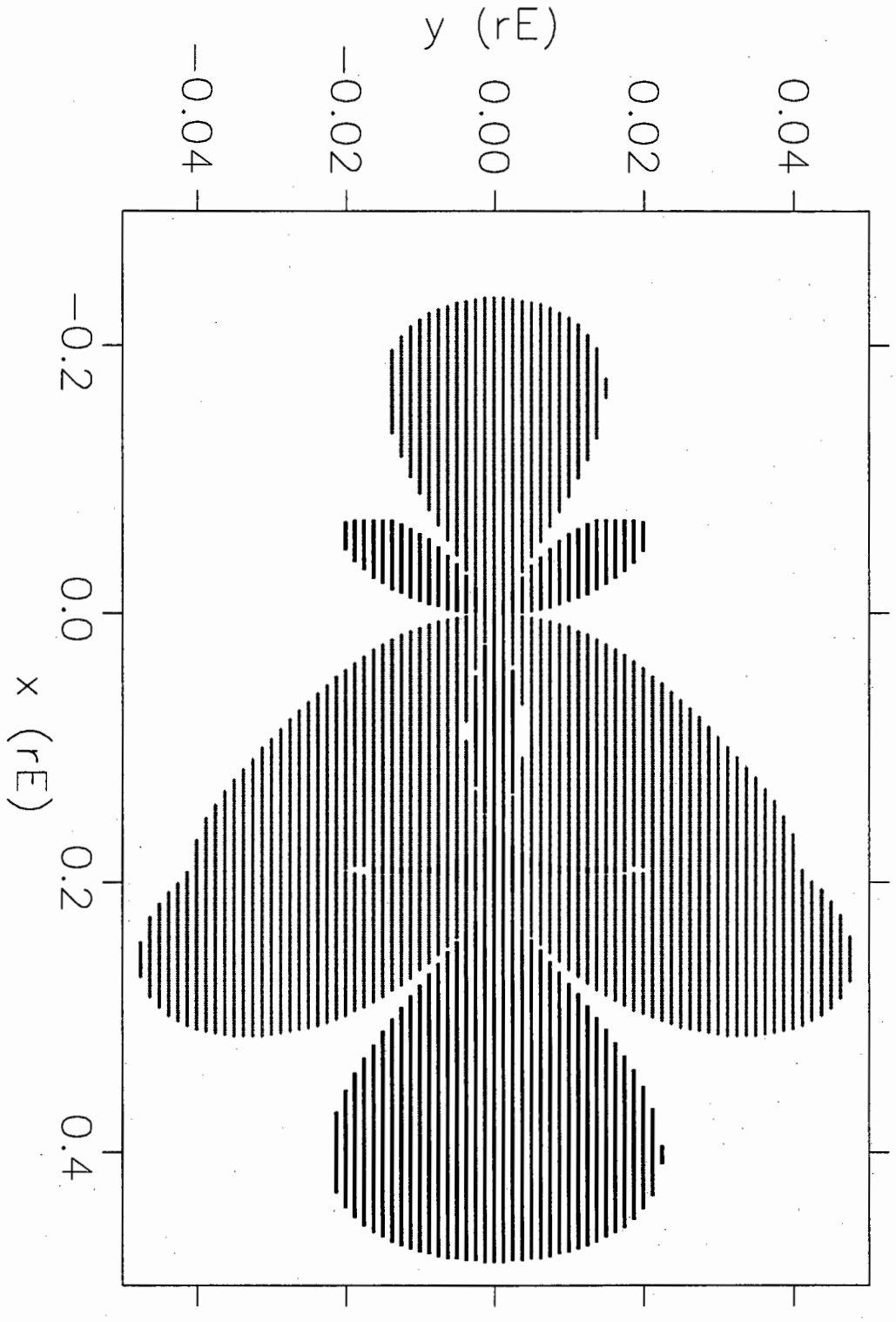

Figure 4.5: The same map as that displayed in Fig. 4.2 with solid blocks for areas of increased magnification above the single lens point source model, and plus-signs for points with less magnification. The resolution is 800 points per r_E.

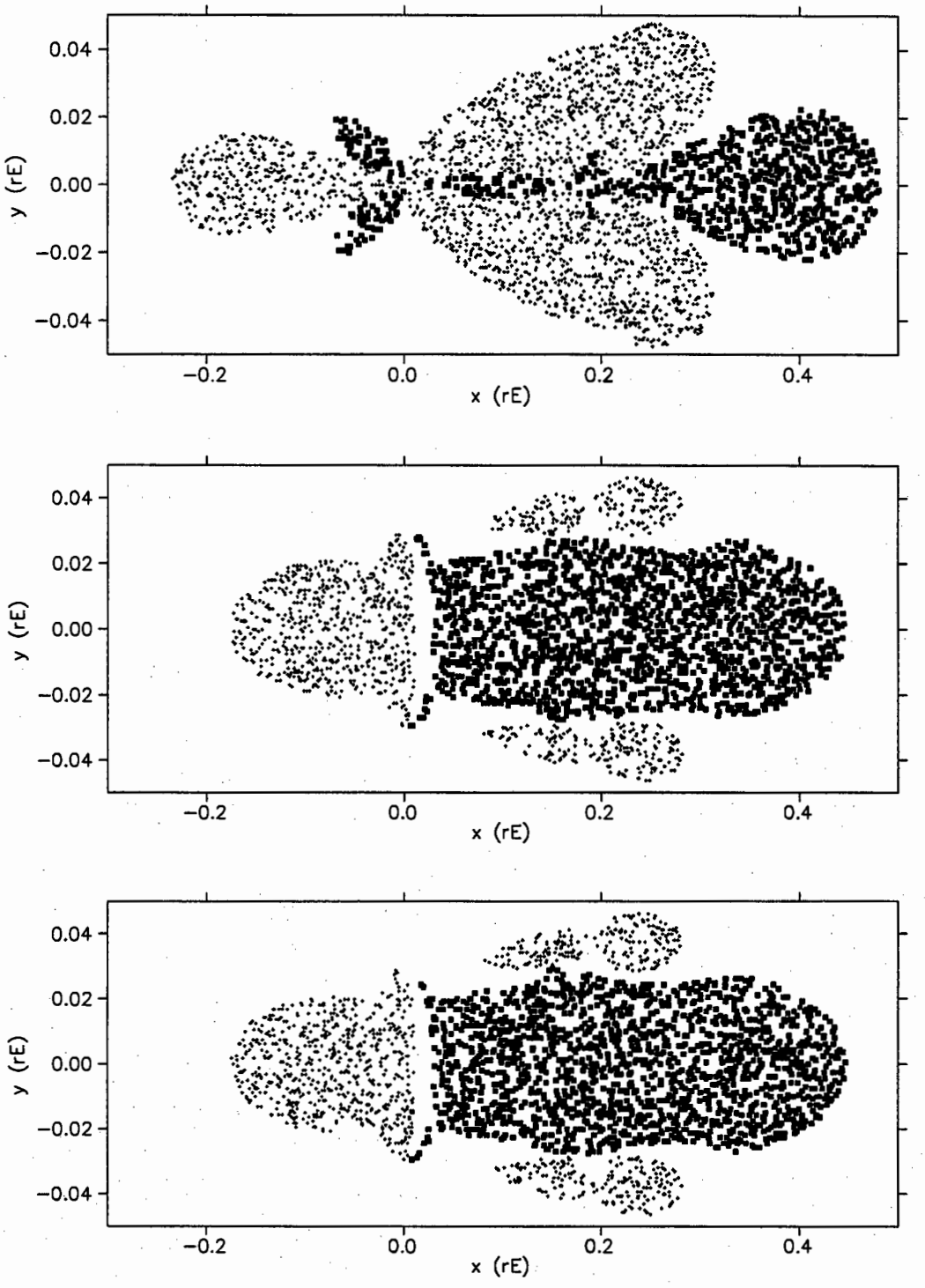

Figure 4.6: Resolved source convolution and blending of the example event from Fig. 4.2. The top panel shows every 30th point from the original point source difference map, the center panel shows every 30th point of the resulting resolved source map for $r_s = 0.03$ and the bottom map the same event after blending of $f = 0.5$ has been included. The resolution of the complete map is 1600 points per r_E.

[Han 1997] indicates a large population of unresolved stars in surveys that serve as potential sources of lensing events.

4.2.4 Detection routine

Detection probability as calculated will depend not only on detection criteria but also on the specific method used to sample a difference map for anomalies. The safest way to calculate the detection probability is to simulate real-life sampling as closely as possible, i.e. to cut light curves out of a difference map with observers' sampling frequencies and check how many such curves yield detections. The detection algorithm used in all calculations was:

1. Examine the difference map in the form of a list of points that deviate from the single lens amplification by more than 0.5%, point by point.
2. For each point, cycle through all observation model parameters.
3. For each set of observation parameters:
   (a) Check whether the data point differs by more than the cutoff c, and whether it falls on an observer's sampled light curve.
   (b) If so, the point is a "hit" - an anomalous point, but not yet a detection.
   (c) If there are more than two consecutive hits by now for this model, enable real-time frequency modification where applicable.
   (d) If more than h_c hits have been made, the light curve has yielded a detection. The rest of the curve is skipped for this model, and the detection count is incremented.
4. After going through the entire list of points, rotate the map through 10 degrees and repeat the process, from 0 degrees to 90 degrees. This takes into account the symmetry of the difference map, simulating each possible light curve once per rotation.

This method has the advantage in computation efficiency because the list of anomalous points is checked only once per rotation for each model.

4.2.5 Parallax and planetary perturbations

Planetary perturbations were examined separately from binary perturbations. Ignoring parallax effects on binary light curves is justifiable. Parallax is a long time scale effect, coupled to

the Earth's motion around the sun O(100 days). Perturbations due to planets, in contrast, are short time scale effects, to the extent that parallax will be negligible on a planetary perturbation, even though it may affect the curve that the planetary anomaly occurs in as a whole. It is therefore reasonable to consider these two kinds of anomalies separately, although resolved source and blending effects were included in both investigations.

Chapter 5

Results

5.1 Planet detection results

5.1.1 Method of observation and efficiency

The best observational strategy would maximise detection probability while minimising observation time: an important step towards optimizing current and future microlensing surveys and follow up observations.

5.1.1.1 Photometric precision

The detection probability, using the criteria discussed in 3.2 above, is plotted as a function of c, the anomaly detection threshold, in Fig. 5.1.

The sharp decline in detection probability between one- and five percent photometry is apparent from the figure (5.1). A rise in detection probability at this level is particularly important, because survey groups typically detect perturbations of 5-10% at the 2-σ level, whereas follow up groups are capable of 1% photometry, with a 2% detection threshold corresponding to a 2-σ deviation.

A sharp increase in detection probability is expected when c is small enough to detect a significant fraction of the wing. This concept is further explored in Fig. 5.2 by examining the cumulative distribution of anomalous area in a difference map of the magnitude of the anomaly. Although the details of the distribution vary with varying parameters, there is always a sharp decline in anomalous area with increasing magnitude difference.

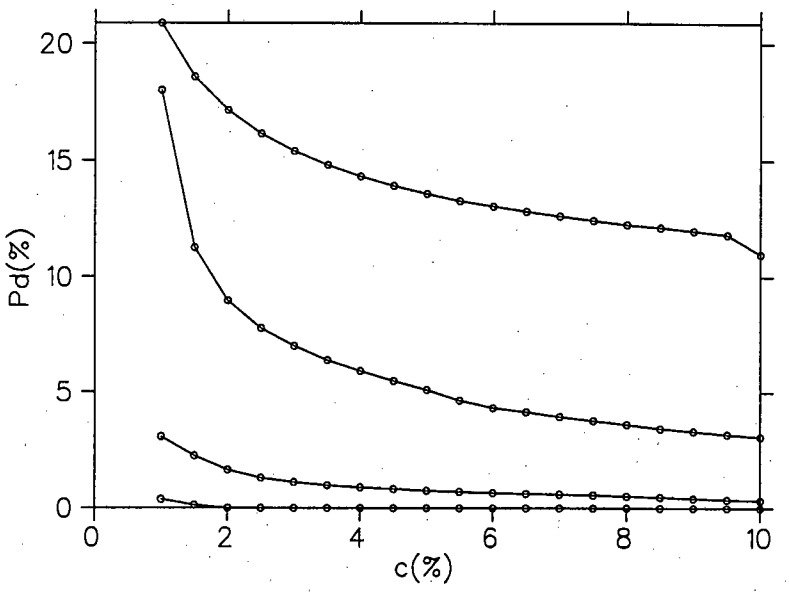

Figure 5.1: Detection probability as a function of the photometry cutoff. All curves have planetary lens parameters $a = 1.3$, $r_s = 0.006$, $f = 0.75$ and observing parameters $N = 400$, $e = 0$, $R_c = 1$ and $h_c = 4$. The mass ratio, q, from top to bottom is 10^{-3}, 10^{-4}, 10^{-5} and 10^{-6}.

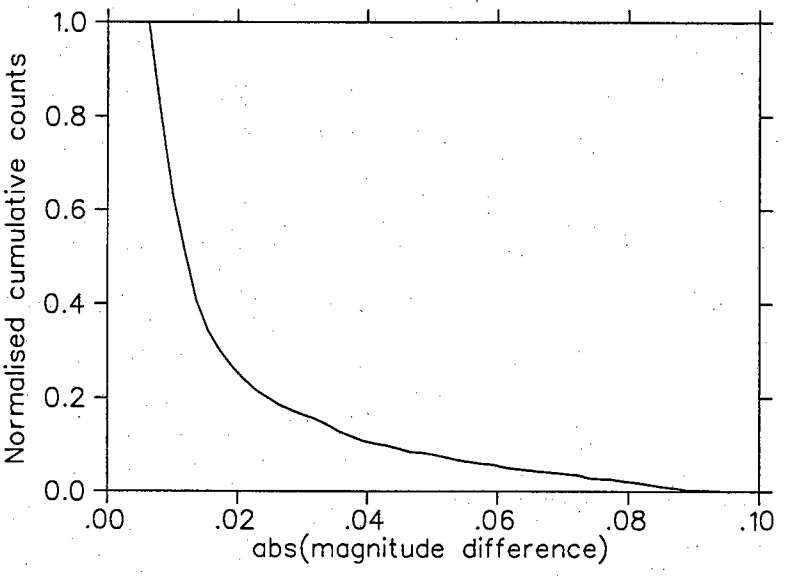

Figure 5.2: Cumulative distribution of anomalous area (normalised)for a difference map with planetary parameters $a = 0.6$, $q = 10^{-3}$, $r_s = 0.006$ and $f = 1$.

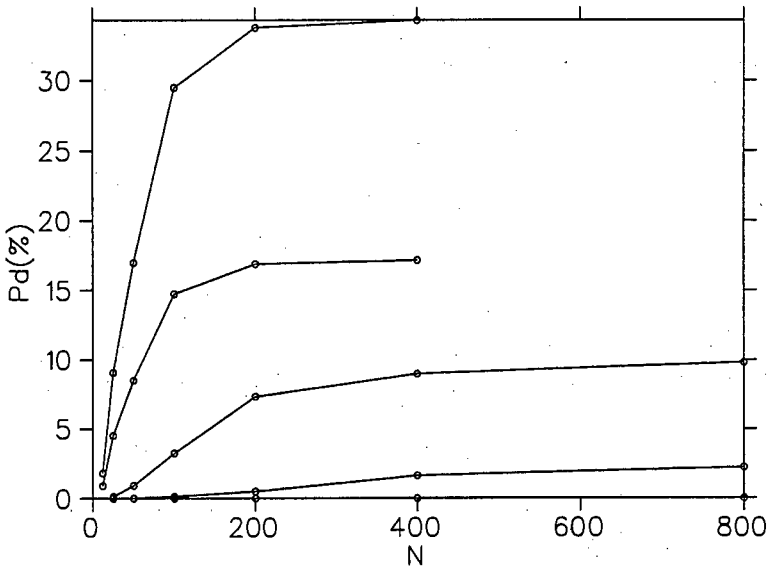

Figure 5.3: Detection probability as a function of the sampling frequency. All curves have planetary lens parameters $a = 1.3$, $r_s = 0.006$, $f = 0.75$and observing parameters $c = 0.02$, $e = 0$, $R_c = 1$ and $h_c = 4$. . The mass ratio, q, from top to bottom is 10^{-3}, 10^{-4}, 10^{-5} and 10^{-6}.

5.1.1.2 Sampling frequency

Detection probability as a function of sampling frequency (N) is plotted in Fig. 5.3. A priori, an s-curve is expected. At very low sampling frequency anomalies are missed altogether. At very high sampling frequency, anomalies are always discovered, leading to a flattening of the detection curve. The position of the turnover will depend on the extent of the anomalous area in the difference maps. More frequent sampling is required for smaller mass ratios or worse photometry (larger c). In Fig. 5.3, the flatter part of the curve is reached earlier for the mass ratio $q = 10^{-3}$, while the "saturation" frequency has not yet been reached for the $q = 10^{-4}$ planet at sampling of 200 data points per r_E.

5.1.1.3 Increased sampling after an alert (e)

At the first sign of a planetary detection ("first sign" is defined as two consecutive anomalous points), observers react either by continuing sampling at the normal rate, i.e. no reaction ($e = 0$), or by increasing the sampling rate until the detection is confirmed or the light curve returns to normal without satisfying the detection criteria. The effect of doubling or quadrupling the sampling frequency temporarily is compared to the no-reaction scenario in Fig. 5.4.

The opportunistic increase in sampling frequency improves detection probability consid-

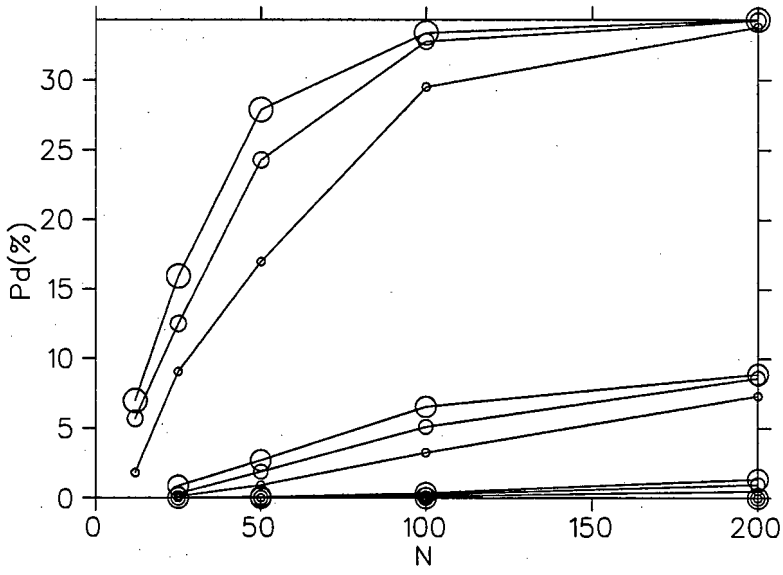

Figure 5.4: Detection probability as a function of the sampling frequency. All curves have planetary lens parameters $a = 1.3$, $r_s = 0.006$, $f = 0.75$ and observing parameters $c = 0.02$, $R_c = 1$ and $h_c = 4$. P_d is zero throughout for the mass ratio $q = 10^{-6}$. Solid lines refer to $q = 10^{-3}$, dashed lines to $q = 10^{-4}$ and dotted lines to $q = 10^{-5}$. The size of the plot symbol refers to the value of e. Small: $e = 0$, medium: $e = 2$ and large: $e = 4$.

erably . The largest gain in detection efficiency occurs at low sampling frequency, where detections can be doubled just by virtue of live data reduction and further investigation of anomalous points. There is also a saturation effect for larger N, where anomalies are detected regardless of the additional data.

Quick response to anomalous data, by way of live data reduction leads to a definite improvement in detection probability at very little cost to observation time.

5.1.1.4 R_c, sampling radius

It is traditionally assumed that light curves are monitored for planetary anomalies when the source distance from the primary is smaller than 1 r_E. The reason for the wide acceptance of this value is that survey groups generally alert follow up groups to microlensing events after the amplification crosses a detection threshold, taken to be $A = 1.34$. In practice, follow up groups may choose to observe less of the light curve or follow it up until well outside the Einstein radius, while survey groups will have data covering many Einstein radii before and after the event from the survey. Fig. 5.5 shows the total number of anomalous curves normalised to the number of curves checked per r_E as a function of the sampling radius for two binaries with different projected separations, a.

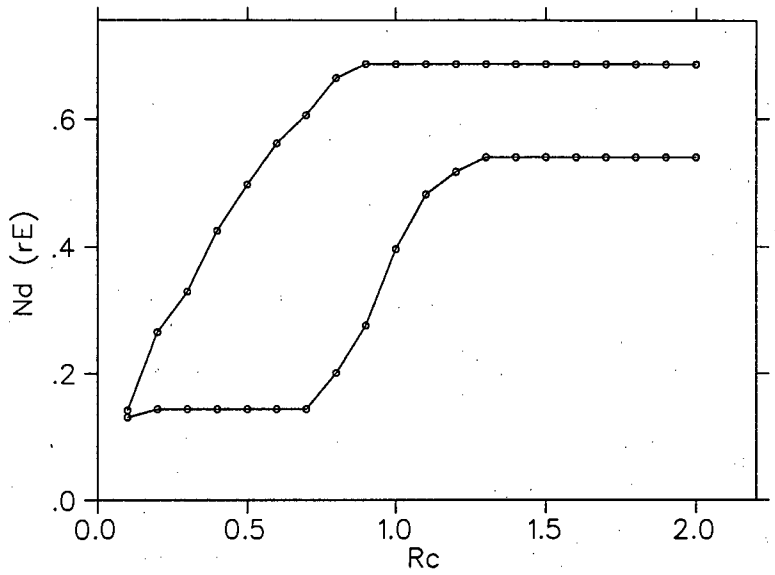

Figure 5.5: Total number of anomalous curves normalised to the number of curves checked per r_E as a function of the sampling radius. Both curves have planetary lens parameters $q = 10^{-3}$, $r_s = 0.006$, $f = 0.75$ and observing parameters $N = 400$, $c = 0.02$, $e = 0$ and $h_c = 4$. The top curve is for binary separation $a = 1.3$ and the bottom for $a = 0.6$.

Maximum detection is reached even before $R_c = 1$ for the $a = 1.3$ curve, while the $a = 0.6$ curve is still missing a large number of potential detections at $R_c = 1$. For planets situated inside 1 r_E, two caustics occur outside of 1 r_E, and these will be missed by observers following within 1 r_E only. This effect is predicted by the approximation Eq. 2.17, although only qualitatively, as this approximation ignores the important role of the central caustic to planet detection.

As discussed in 2.2.4, the projected distance of the source from the primary to where light curves are sampled determine the region in a where detection probability is reasonably high, a.k.a. the lensing zone. At binary separations outside of the lensing zone, the "non-central" caustics move further away and out of the region of the source plane that can reasonably be expected to be monitored for anomalies. The cost in observation time for an R_c strategy scales as $cost \propto R_c^2$, so that a small gain in the number of detections will not outweigh the tremendous observing cost, unless observing cost is not a factor.

5.1.1.5 h_c, number of anomalous points required for a detection

Unlike the other observing parameters, h_c is highly subjective by nature. Ultimately, the number of anomalous points required to confirm a detection will be dependent on the specific situation. Limits may be set, by for example how many points are required to make an

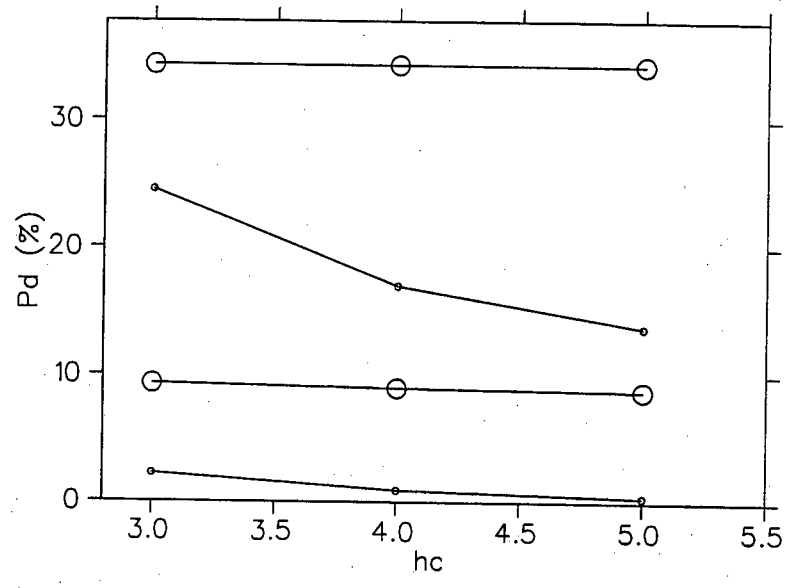

Figure 5.6: Detection probability as a function of the number of anomalous points required to confirm detection. All curves have planetary lens parameters $a = 1.3$, $r_s = 0.006$, $f = 0.75$ and observing parameters $c = 0.02$, $e = 0$ and $R_c = 1$. The large plot symbols refer to $N = 400$ while the small symbols refer to $N = 50$. The top two curves have $q = 10^{-3}$, and the bottom two $q = 10^{-4}$.

acceptable binary lens fit to the data, or the precision of the photometry of the anomalous points in question and nearby data. Unfortunately other parameters like the persuasiveness of the observer are not easily modeled. A value of $h_c = 4$ has been considered reasonable in the past. Fig. 5.6 shows $\frac{P_d}{P_{dmax}}$ as a function of h_c, where P_{dmax} is the maximum detection probability for an entire set of geometrical and observational parameters with variable h_c.

5.1.1.6 Observing time cost

An observational strategy with a large number of data points may have a high detection probability but at a prohibitively large cost in observation time. In Fig. 5.7 we plot the distribution of detection efficiency, $E = \frac{P_d}{cost}$, for all sets of observation parameters that yield a non-zero P_d for a planetary system with parameters $a = 0.6$, $r_s = 0.006$, $f = 0.75$ and $q = 10^{-3}$.

The peak efficiencies occur for observation parameters $N = 50$, $c = 0.01$, $e = 4$, $h_c = 3$, and $R_c = 0.1$. This set of observation parameters remains the most efficient for other values of a and q, but not r_s. The small-R_c monitoring strategy fails dramatically for the combination of small q and a large resolved source radius, r_s, due to the total cancellation of the central caustic anomaly. This cancellation is discussed further in 5.1.2.2. For this regime, i.e. $q = 10^{-5}$,

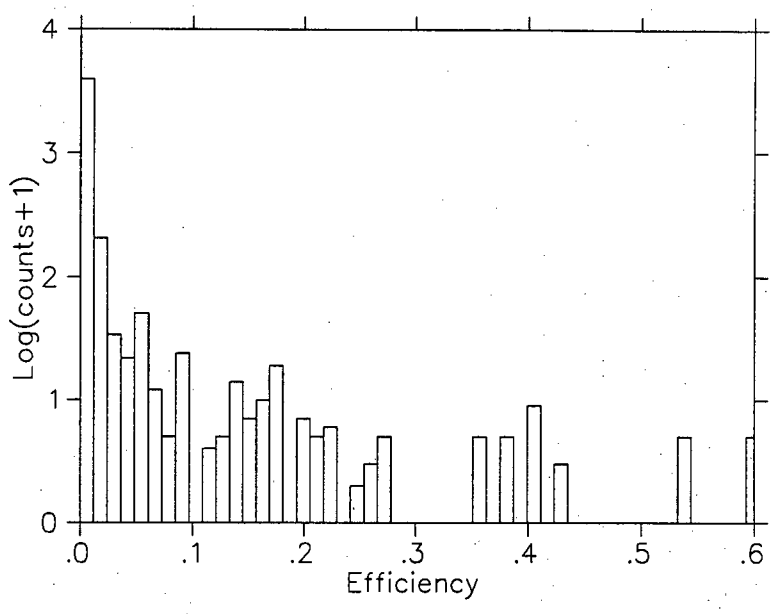

Figure 5.7: The distribution of detection efficiency for all sets of observation parameters that yield a non-zero P_d for a planetary system with parameters $a = 0.6$, $r_s = 0.006$, $f = 0.75$ and $q = 10^{-3}$.

$r_s = 0.03$, the most effective observation parameters are $N = 50$, $c = 0.01$, $e = 4$, $h_c = 3$, and $R_c = 1$.

As expected, a quick response (a non-zero value for e) has a dramatic positive influence on efficiency.

A decision about sampling frequency N for a follow up observer, if not already forced into a certain N by circumstances such as a short time scale, bad weather or a faint event requiring long integration times, will depend mostly on the amount of events that are available for follow up monitoring. If few events are available, the increase in detection probability with greater sampling frequency could be exploited and would yield the additional benefit of constraining the fit to the light curve. If more events are in progress than can be monitored at any given time, however, the detection strategy with maximum efficiency should be followed, provided that the photometry can provide enough constraints to the fit.

5.1.2 Detection probability due to event parameters

The role of the observer's effort and methods in determining detection probability was discussed above, while below, the microlensing event parameters' effect on detection probability is examined. Most of the parameters discussed below are "out of the observer's control" i.e. the parameters cannot be known until many observations have been made (event parameters

such as a, q, r_s and f). The observer will be unable for the most part to select events that are intrinsically more likely to yield an anomaly. The notable exception is the current source distance from the lens, u, as this is known to some degree at any time (depending on whether blending and parallax are present/known) from the amplification. The source magnitude is also known and can be used to make order of magnitude estimates of r_s.

5.1.2.1 Mass ratio (q) and projected planet separation from primary (a)

Intrinsic detection probabilities that are out of the observer's control may be quantified by choosing four observation models (sets of observing parameters) to make all the comparisons. For this purpose we choose models

ME, most efficient (see 5.1.1.6): $N = 50$, $c = 0.01$, $e = 4$, $h_c = 4$, and $R_c = 0.1$.

TF, typical follow up observations: $N = 100$, $c = 0.02$, $e = 2$, $h_c = 4$ and $R_c = 1$.

TS, typical survey: $N = 25$, $c = 0.1$, $e = 0$, $h_c = 4$ and $R_c = 1$. The value of N is perhaps optimistic for current surveys but reflects the values that may be available in the near future.

LR, large follow up radius: $N = 100$, $c = 0.02$, $e = 2$, $h_c = 4$ and $R_c = 2$.

Note that for the survey model, TS, we assume $R_c = 1$, although survey groups have the entire light curve at their disposal for many Einstein radii. This is because P_d gives the detection probability averaged over all light curves, including the ones for stars that may be unlensed during a survey! P_d is the global detection probability and not really the value of interest here. The end result is that survey group detection probability is slightly underestimated, as we are ignoring detections outside of 1 r_E, even though they are capable of making these rare detections. Fig. 5.8 is a contour plot representing P_d as a function of $\log(a)$ and $\log(q)$ of all four models for a typical (favourable) planet geometry.

By far the best prospects for planet detection occur within the lensing zone of the respective observing strategies. For $R_c = 1$, this region is $0.6 < a < 1.6$. For the ME model, however, replacing $R_c = 0.1$ in Eq. 2.19 yields a very narrow band of projected planet orbital radius, a, between $0.95 < a < 1.05$. In the LR case, the zone is predicted to be within $0.4 < a < 2.4$.

Within the lensing zone is another band centered at $a = 1$, where the detection probability declines. This area of lower probability is explained by considering a planetary anomaly as a perturbation of one of the single lens images at the position of the planet. In the single lens

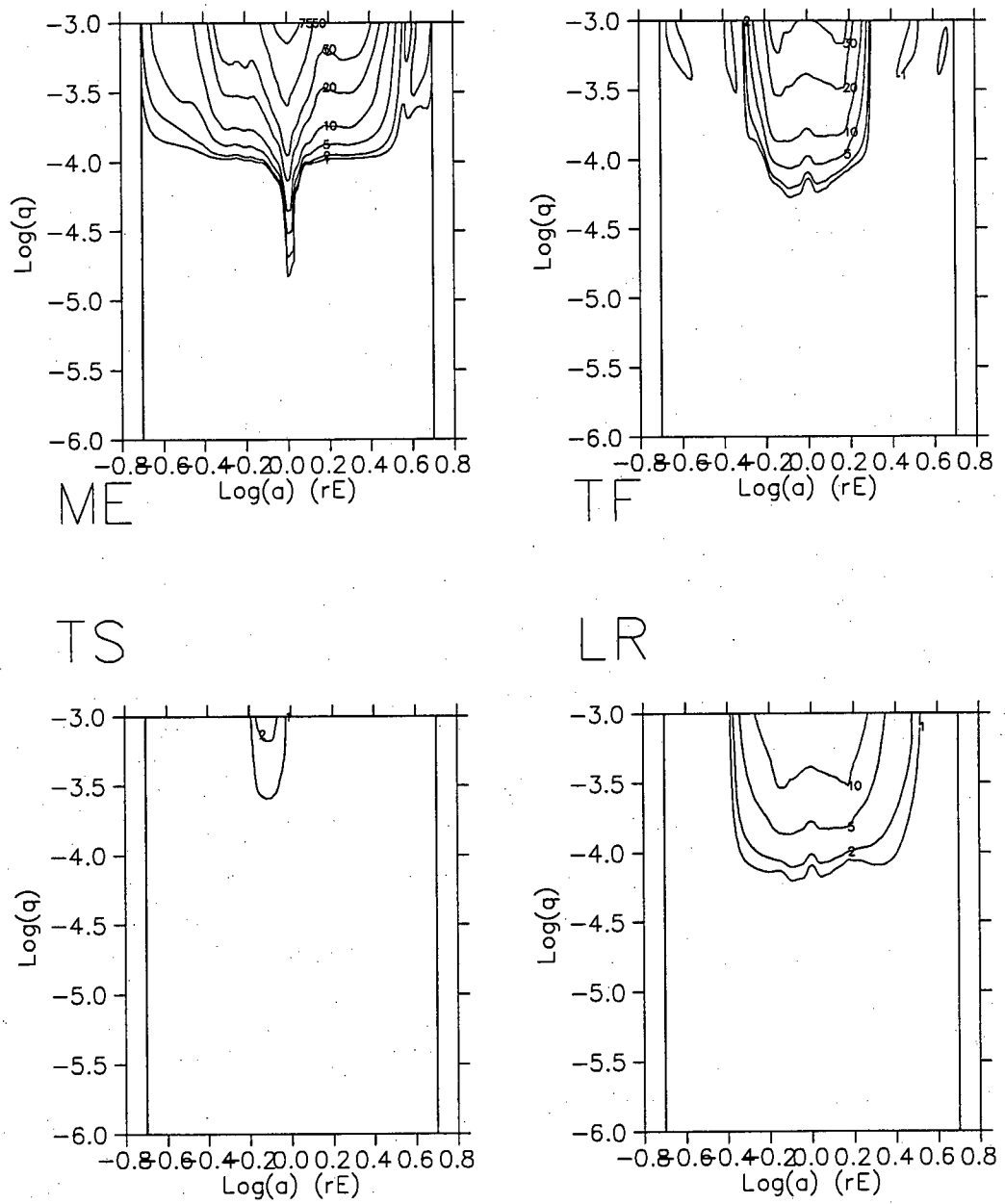

Figure 5.8: Contour plot representing P_d as a function of $\log(a)$ and $\log(q)$. In all four graphs, $r_s = 0.006$ and $f = 0.75$.

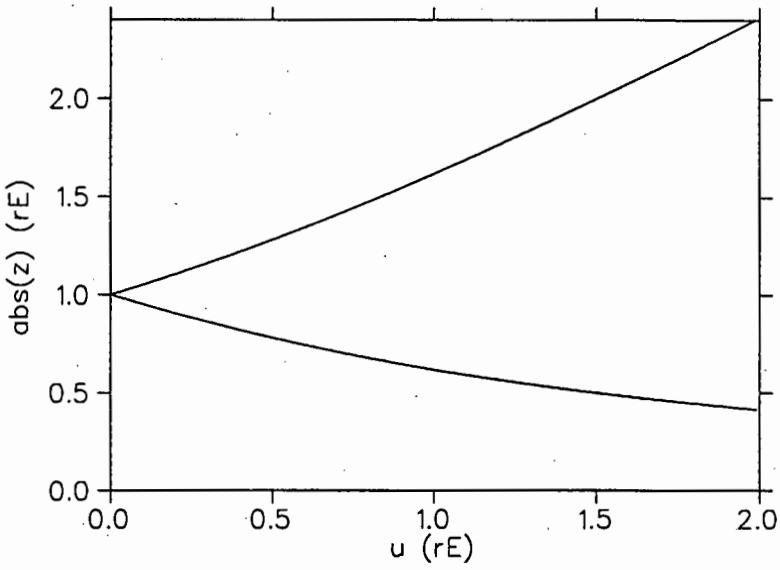

Figure 5.9: The distance of the image positions to the primary, $\|z\|$, as a function of u for the two single lens image positions.

case, two images of the source are formed. For a large distance between source and lens (u), one image is very close to the source and the other, much smaller image, is very close to the lens. As u decreases, the outer image moves inwards towards the Einstein ring, and the image close to the lens position moves outwards, also towards the Einstein ring. A planet located close to the Einstein ring has a large probability of being intercepted by one of the primary's images and causing an anomaly for a large range of impact parameters. The images never cross the Einstein radius unless the source is exactly at the origin, in which case the Einstein ring is the critical curve for a single lens. A planet located exactly on the Einstein ring is therefore never involved in perturbing the single lens light curve, for a small source radius at least. The distance of the image positions to the primary is plotted in Fig. 5.9 for both images from Eq. 2.9. Note that the image position is never equal to one except at $u = 0$.

This approximation breaks down for larger mass ratios or large resolved sources, and does not take the role of the central caustic into account. In all but the TS model, an increase in P_d is visible for larger a, around $a = 4$.

The effect of decreasing mass ratio is also seen in Fig. 5.8. For small source radius, the decrease in P_d as q decreases is steep in the lensing zone leading to the much smaller detection probability of Earth mass planets (roughly 5×10^{-6}) as compared to Jupiter mass planets (10^{-3}).

5.1.2.2 Resolved source

As a comparison to Fig. 5.8, Fig. 5.10 shows a contour map of P_d with identical event parameters, but for a larger source radius. The detection probabilities for large mass ratios remain almost unchanged, but there is a dramatic effect for smaller mass ratios.

A large resolved source affects the detection of small mass ratio planets favourably because each caustic area, normally small for small mass ratio, is effectively extended to a circular area of radius of the order of one resolved source radius. A small area of large positive magnification in a difference map is most often surrounded by a larger area of slightly negative magnification. If a resolved source covers an entire caustic region, the positive and negative magnification areas cancel exactly leading to a net loss of detection probability.

For most light curves, however, the entire caustic region is not covered. A net non-zero anomaly is created covering a minimum area that is determined by the resolved source radius, not the mass ratio and orbit projection alone as is the case for the point source approximation. The smoothing effect can influence detection probability negatively when marginally detectable magnifications in the point source approximation are smoothed to below the detection cutoff.

It is apparent from Figs. 5.8 and 5.10 that the increases occur on one side of the lensing zone only, ($a > 1$). The shift in the lensing zone away from values of $a < 1$ has been remarked on before [Bennett & Rhie 1996]: the $a < 1$ systems have a region of negative amplification between two regions of positive amplification. A large source radius will cover all these regions and lead to a cancellation of the anomaly.

The smoothing and increased detection area effects work against each other, leading to a minimum in detection probability as a function of r_s for some combinations of geometry and observation strategy, as seen in Fig. 5.11. A large increase in detection probability with increasing source size is possible. From Fig. 5.11 it is noticeable also that for mass ratios that are too small, i.e. $q = 10^{-5}$, the detection probability is already zero throughout for the TF model and the increase in resolved source radius has no effect. In addition, any change in detection probability due to r_s is dependent on the type of observations being made.

The ME model shows a sharp rise in efficiency to a maximum at $r_s \approx 0.015$ and a gradual decline thereafter, while the TF model detection probability is still rising at $r_s = 0.03$. This difference is due to the fact that the ME model observes mostly the central caustic, while the TF observes all caustics within $R_c = 1rE$, and the central and outer caustics are affected differently by increasing r_s. The increase will also be a function of the photometry cutoff, c.

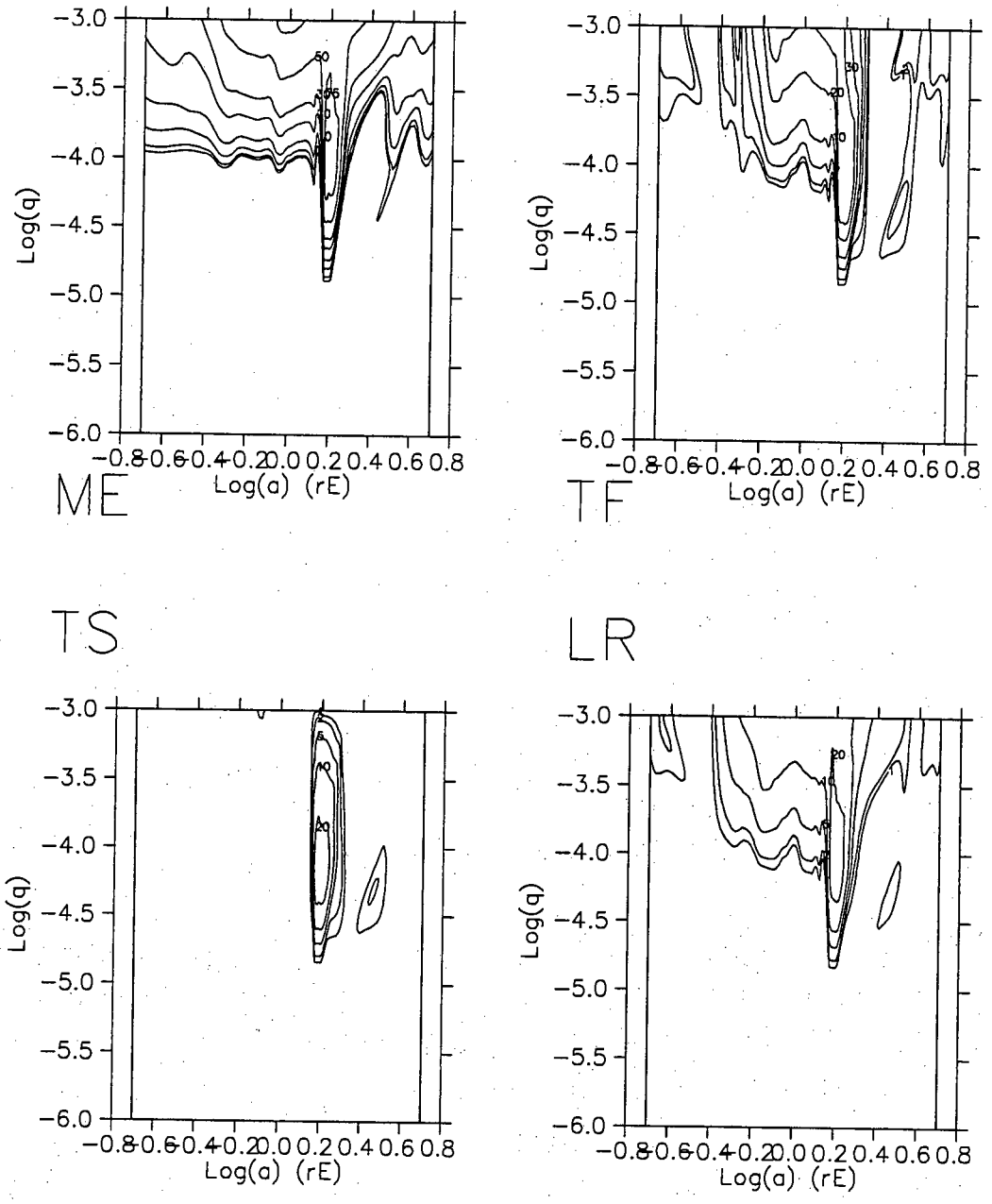

Figure 5.10: Contour plot representing P_d as a function of $\log(a)$ and $\log(q)$. In all four graphs, $r_s = 0.03$ and $f = 0.75$.

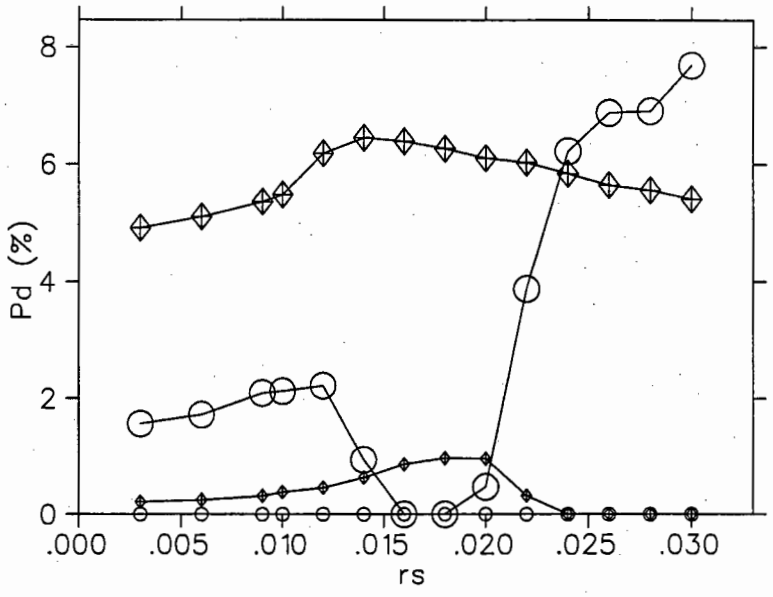

Figure 5.11: Detection probability as a function of r_s. All curves have planetary lens parameters $a = 1.3$, and $f = 0.75$. The large plot symbols refer to $q = 10^{-4}$ while the small symbols refer to $q = 10^{-5}$. Circles refer to the TF model and diamonds to the ME model.

5.1.2.3 Blending

The effect of blending on planet detection was found to be minimal in these simulations. As discussed in 2.4 above, the effect of blending on an *amplification* difference map is to multiply the entire map by the blending factor f. For small planets with small caustic areas, blending may reduce the small area of detection likely to be just above the threshold to under this threshold causing a large reduction in detection probability. Reduction of the height of large peaks of anomalies has little effect on total detection probability as the peak is likely to remain above cutoff photometry after a modest blending correction. For large planets the effect is small, as most of the map is well above detection threshold.

The effect of blending on the magnification maps of two planets with mass ratios $q = 10^{-3}$ and $q = 10^{-6}$ respectively is shown in Fig. 5.12 by plotting the distribution of anomalous area in the two maps.

5.1.3 Detection probability as a function of impact parameter

While an event is in progress, the amplification is directly related to the relative distance between source and lens. In the absence of anomalies, such as resolved source and blending effects, the relationship is one to one (Eq. 2.10). Even if blending is present, it could be fitted

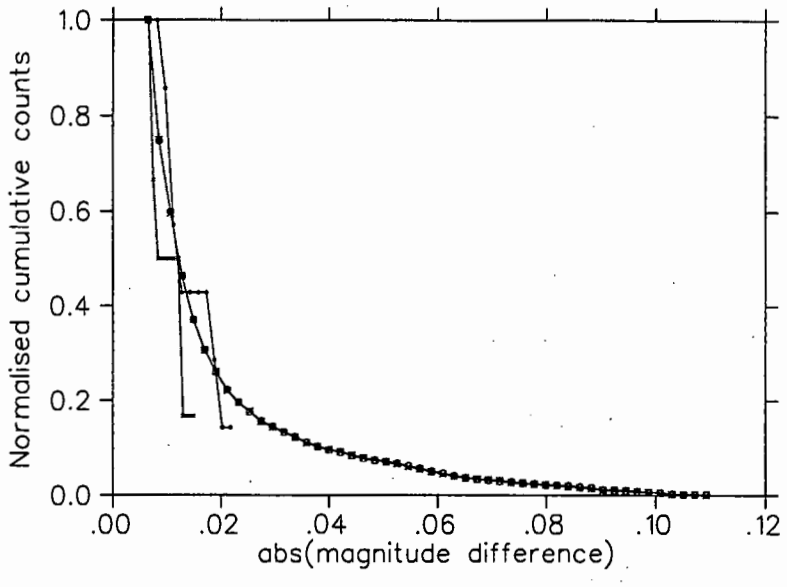

Figure 5.12: Cumulative distribution of anomalous area (normalised) for a difference map with planetary parameters $a = 1.3$ and $r_s = 0.006$. The $f = 1.0$ curve is indicated by circles and the $f = 0.5$ event by crosses. The system with $q = 10^{-3}$ is indicated by larger plot symbols.

and taken into account by using the data obtained for the first part of the event, although such a fit is unlikely to be accurate. In most cases, therefore, the observer is likely to have an estimate of the projected distance between lens and source as a function of time (u). If the detection probability is known as a function of u, observers will be able to determine real time detection probability and reschedule observations to obtain maximum detection efficiency.

Fig. 5.13 shows the percentage of the area of a ring centered at the position of the primary with width Δu, that yields a detectable anomaly for a given c, as a function of u. The event has $a = 1.3$, $r_s = 0.006$ and $f = 1$. The anomalous area is proportional to the detection probability for ideal detection conditions (very high sampling frequency, etc.). The cutoff is chosen as $c = 0.02$.

As is the case for all planetary events, the highest detection probability by far occurs when u approaches zero, i.e. the source approaches the position of the primary. This is the result of the elongation of the central caustic point, as in the single lens case, into a sharp triangular caustic shape when the lens has a companion. Unfortunately, few microlensing events reach the small values of u required for such a large detection probability - close to 100% for $q = 10^{-3}$ planets, and 100% for a larger range of b in the case of brown dwarfs or larger mass companions, $q > 10^{-3}$.

The impact parameters of all microlensing events have a flat distribution, ignoring the $\approx$ 10% effect that blending has on the distribution, e.g. [Lee & Han 1997] so only 1 in 100

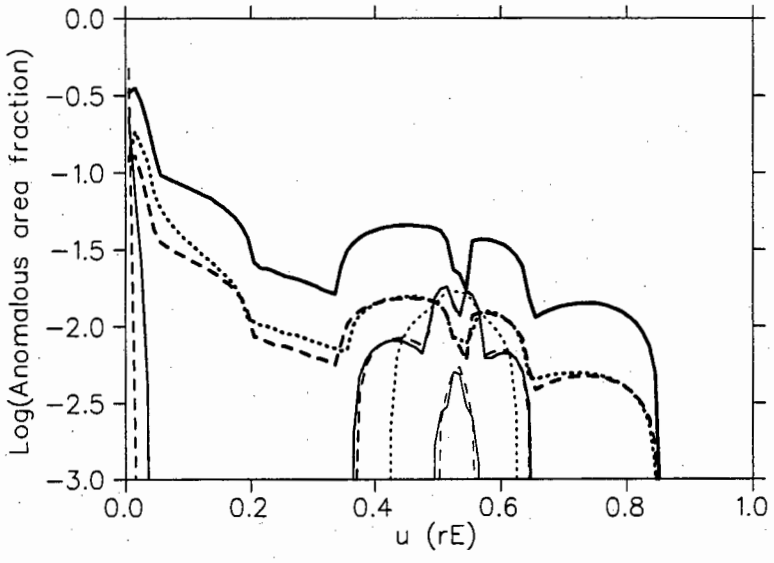

Figure 5.13: Percentage of the area of a ring centered at the position of the primary with width Δu, that yields a detectable anomaly for $c = 0.02$, as a function of u. Line thickness refers to mass ratio: thickest for $q = 10^{-3}$, medium for $q = 10^{-4}$ and thinnest for $q = 10^{-5}$. The event has $a = 1.3$ and $f = 1$. Line type refers to the resolved source size: solid for $r_s = 0.006$, dashed for $r_s = 0.01$ and dotted for $r_s = 0.03$. There is no anomalous area for the combination $q = 10^{-5}$, $r_s = 0.03$, and no anomalous area mass ratios smaller than $q = 10^{-6}$.

events will have an impact parameter of 0.01, for example. This corresponds to a single lens amplification of about 100, as $A(u) \propto \frac{1}{u}$ for small u. Detection probability is greatly reduced for smaller mass ratio planets.

There is a lot of structure in the plots, due to the irregular nature of the caustic regions. This is more often the case for larger mass ratios, as the caustics are reduced in size for smaller q and localized to certain positions. The structure at $u \approx 0.53$ is due to the two "outside" caustic regions close to the real axis of the complex lens plane at a distance from the primary of $\approx a - \frac{1}{a}$. The positions of these two caustics are predicted by the approximation Eq. 2.17.

The above results highlight the importance of monitoring microlensing events when they are close to or at their highest amplification. High amplification events are of the utmost importance to planet detection. The source in these events will approach the position of the primary and allow lensing due to the central caustic to be observed, even for planets with smaller mass ratios.

This $a = 1.3$ event contains detectable planetary anomalies for a source position within one Einstein radius of the primary only. For events with $a < 0.6$, the structure due to the two outside caustics is moved to $u > 1.0$. This causes several problems for detection. Microlensing events are generally only detected when their amplification rises above a threshold of $A = 1.34$,

or $u < 1.0$. These events could be followed to any amplification by follow up groups after being alerted by survey groups, but the area of low amplification before $u < 1.0$ will generally not be monitored to follow up density.

Caustics at large distances from the primary lens are likely to be missed by the source simply because of the larger area in the lens plane that a source can be found for a given distance from the lens u. This area is given by $2\pi u \Delta u$, the area of a ring centered on the primary that contains a caustic region between a distance u and $u + \Delta u$. As a result, the chance of detecting a caustic with a given size scales roughly as $\frac{1}{u}$. This modulation can be pictured as a straight line of slope -1 in the logarithmic plot Fig. 5.13. Finally there may simply not be enough observation time to follow all events to amplifications lower than 1.3 with sampling that is dense enough to yield a non-zero detection probability.

The existence of caustics outside of 1 r_E raises the interesting question of detecting "microlensing events" of short duration that are in reality caustic crossings of binary systems at large impact parameters. There are two caustics outside of 1 r_E for each companion within 1 r_E. A large amount of companions within the Einstein ring radius could cause a non-negligible area outside of 1 r_E to be anomalous. The effects of these anomalies on microlensing statistics as well as planet detection remain to be investigated.

5.2 Detection of non-planetary anomalies

5.2.1 Model distributions

The relevant distributions of microlensing parameters based on the microlensing model discussed in 3.1 and generated using the method described in 4.1.1 are plotted in Figs. 5.14 to 5.18. The distributions are plotted with continuous lines for clarity but are in fact the result of 20000 binned events.

The distribution in event timescales for the simulated events agrees well with the MACHO distribution [Alcock et al. 1997a]. The distribution of source magnitude, Fig. 5.15, is also in general agreement with the MACHO results in Fig. 3.1. As we are assuming a constant photometry error that is not dependent on source magnitude, this distribution serves only as confirmation that the model is in agreement with the observed distribution and is not important for the derivation of the results on measurability below.

The simulated distribution of r_s is a cause of concern. In a previous study [Bennett & Rhie 1996], values of r_s used in the study of the resolved source effect were substantially smaller than the corresponding values obtained here. Using $m = 0.3\ M_\odot$ [Bennett & Rhie 1996], the value

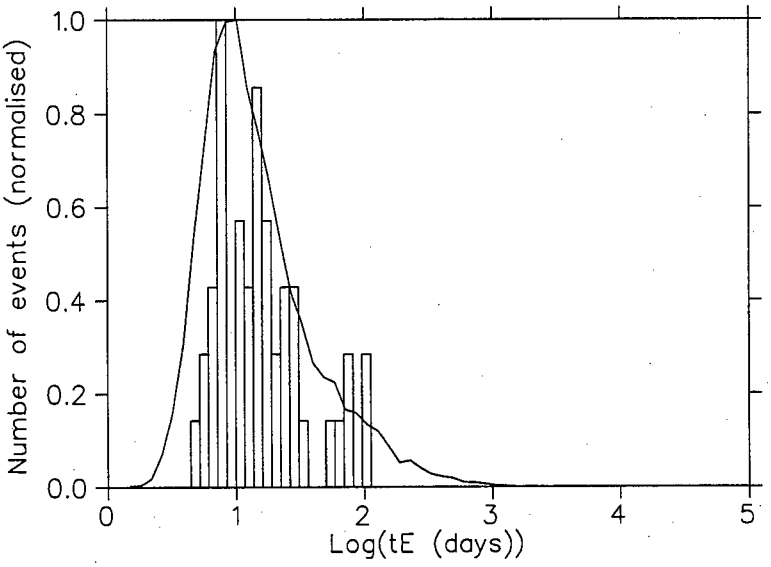

Figure 5.14: The normalised distribution in t_E of 20000 simulated events with the MACHO t_E distribution histogram superimposed.

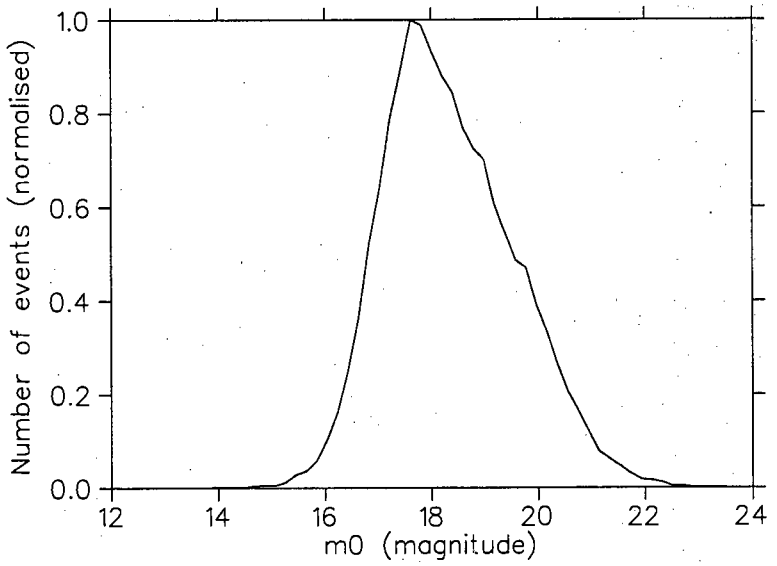

Figure 5.15: The distribution in m_0 of 20000 simulated events.

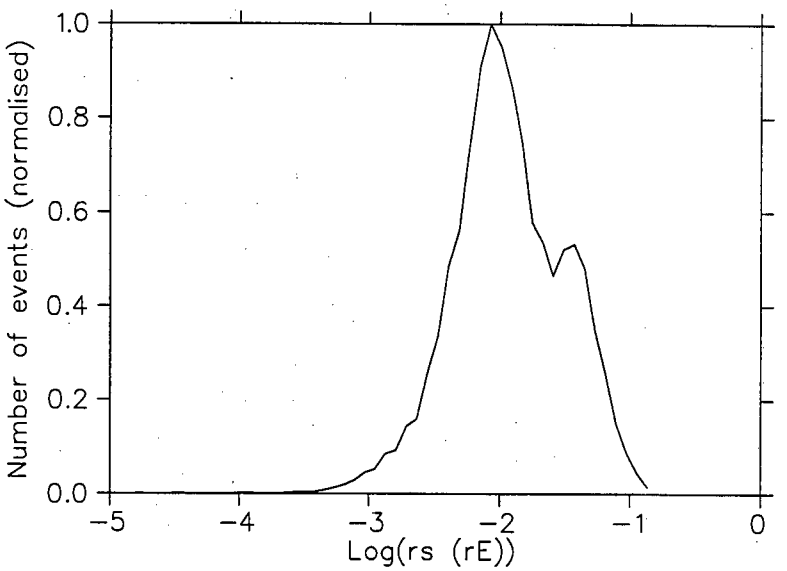

Figure 5.16: The distribution in r_s of 20000 simulated events.

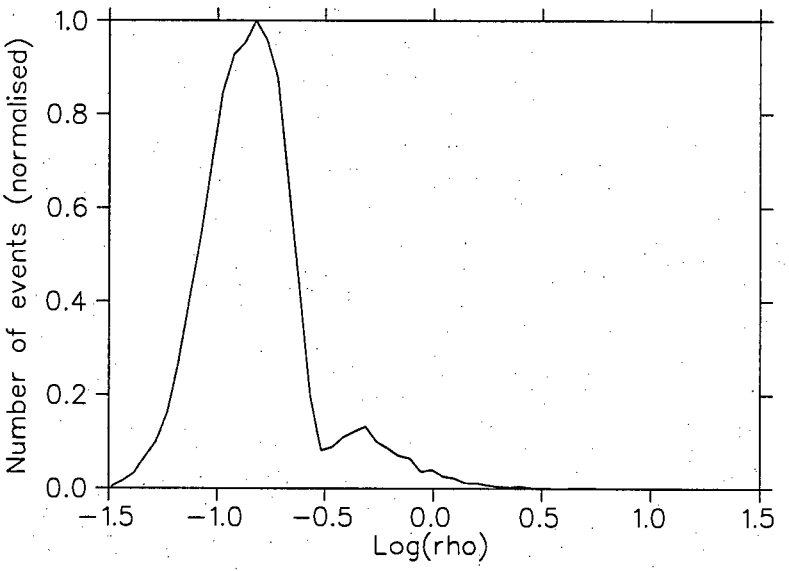

Figure 5.17: The distribution in $\log(\rho)$ of 20000 simulated events.

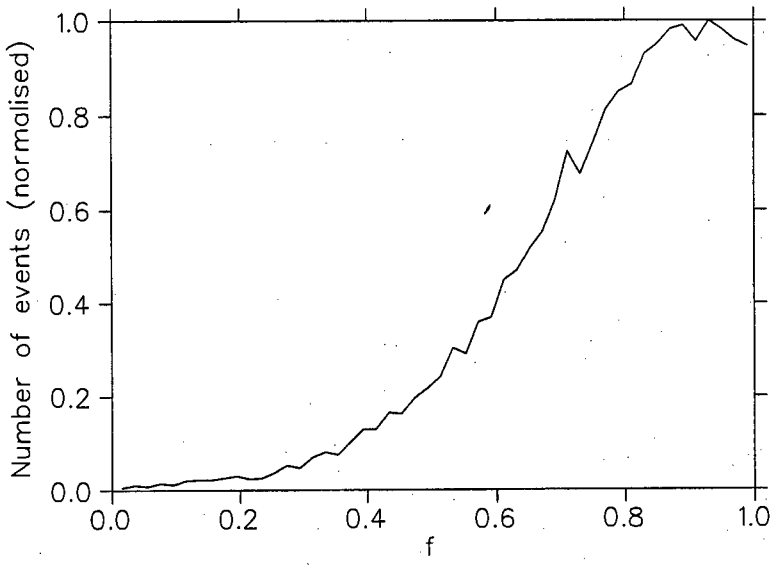

Figure 5.18: The distribution in f of 20000 simulated events.

$r_s = 0.006$ is estimated for a main sequence turn off star in the Bulge being lensed by a lens in the Bulge, the most common geometry of all events. In Fig. 5.16, the peak of the distribution is at $r_s = 0.01$. The values differ because of different lens masses being used in the estimation. The mass distribution used in this simulation is based on a fit to the MACHO t_E distribution (see Eq. 3.6) that yields a mean mass of lenses in observed events of 0.2 $M_\odot$. The secondary peak at $r_s = 0.03$ is the result of lensing of the clump giant population.

Fig. 5.17 is the distribution of ρ, a parallax parameter given by Eq. 2.32. Two conclusions from the figure:

1. Practically all events have a value $\rho > 0.1$, indicating the presence of the parallax effect. Unfortunately, in most events this parallax will be unmeasurable due to the short duration of the average event.

2. The secondary peak at larger ρ is caused by lenses in the disk. These lenses have a smaller value of x, but a comparable t_E due to the smaller relative source-lens velocity of the population. Parallax effects should be better measurable for the case of disk lensing, but these events constitute a small percentage of all events.

The distribution of f is simply that of the model used in 3.1, yielding little blending for most events.

5.2.2 Methods of observation and efficiency

Similar parameters are chosen to those used to describe observations with the aim of detecting planetary anomalies:

1. N, the number of sampled data points per t_E, Einstein radius crossing time.
2. c, the standard deviation of the photometry error.
3. R_c, the maximum radius (in r_E) from the primary lens within which events are sampled. For the non-planetary anomalies, this parameter is slightly different from R_c in the planetary investigation. In this case, all impact parameters, b, are smaller than 1.0, even if they are followed out to a distance of 2 r_E from the primary.
4. Cost, the total number of data points that are taken, when following any given strategy with a set of these parameters.
5. P_d, the percentage of all possible light curves through the area with radius R_c centered on the origin, that yield anomaly detections. This number is referred to as "the percentage of measurable curves" for a certain microlensing parameter. For this project, a fit parameter is considered measurable if it can be determined to within a formal error of 50% with 95% confidence.

The parameters e and h_c are not applicable to non-planetary anomalies, since most non-planetary anomalies (except perhaps resolved source effects) occur over the duration of the curve and should not evoke an increase in sampling rate from follow up groups. Three sets of observational parameters are chosen to correspond to the planetary observation models discussed above:

TF, typical follow up observations: $N = 100$, $c = 0.01$, and $R_c = 1$.

TS, typical survey: $N = 25$, $c = 0.05$, and $R_c = 2$.

LR, large follow up radius: $N = 100$, $c = 0.01$, and $R_c = 2$.

Note that c in this case corresponds to the actual standard deviation of the photometry, σ, while c was chosen as 2σ for the photometry cut-off in the section on planet detection probability. The measurability of various microlensing parameters is shown in Table 5.1 as calculated for each of these models. The three observational models are labeled as TF, TS

Parameter:	t_E	t_m	m_0	b	ψ	ρ	rs	f
TF	6%	17%	99%	40%	8%	4%	6%	38%
TS	3%	11%	100%	19%	8%	2%	4%	19%
LR	13%	26%	100%	77%	13%	9%	7%	66%
$\rho = 0$, $r_s = 0$, $f = 1.0$ LR	83%	82%	100%	84%	0%	12%	0%	67%

Table 5.1: The measurability of microlensing parameters for various observation models.

and LR. The last row shows the percentage of total events that are measurable using the LR observation model but with the microlensing anomaly parameters set to the values that cancel their effect: $\rho = 0$, $r_s = 0$ and $f = 1$. A very large improvement in the measurability of some parameters is seen and is discussed below.

5.2.3 Measurability of parameters

All microlensing parameters and their formal errors were checked for correlation using Spearman's rank-order correlation coefficient, r_{Spear}. This specific correlation check was chosen for its robustness and because the value r_{Spear} is not only a check to see whether parameters are correlated, but also gives the strength of the correlation in the value $P(r_{Spear})$, the two sided significance level of deviation. A small probability $P(r_{Spear})$ points to a likely correlation ($r_{Spear} > 1$) or anti-correlation ($r_{Spear} < 1$). A $P(r_{Spear})$ of close to zero means the data are definitely correlated or anti-correlated. In most cases where correlations were detected the values of $P(r_{Spear})$ were much smaller than one, making a comparison of the strengths of the correlations uncertain. To discuss the correlations, the formal error in each of the microlensing parameters was examined as a function of the two parameters that showed the strongest or very strong correlations. The LR observation model is chosen for the rest of this chapter where the microlensing parameters themselves are investigated.

5.2.3.1 Anomaly parameters

5.2.3.1.1 Parallax, ψ and ρ. The formal error in ψ, $\delta\psi$ shows the strongest correlations with t_E, b, ρ and r_s. The association with b is understandable as all microlensing effects are more pronounced at higher amplification. The correlation with r_s is due to the association of both r_s and ρ with x,

$$r_s \propto \frac{x}{r_E} \text{ and } \rho \propto \frac{1-x}{r_E} \tag{5.1}$$

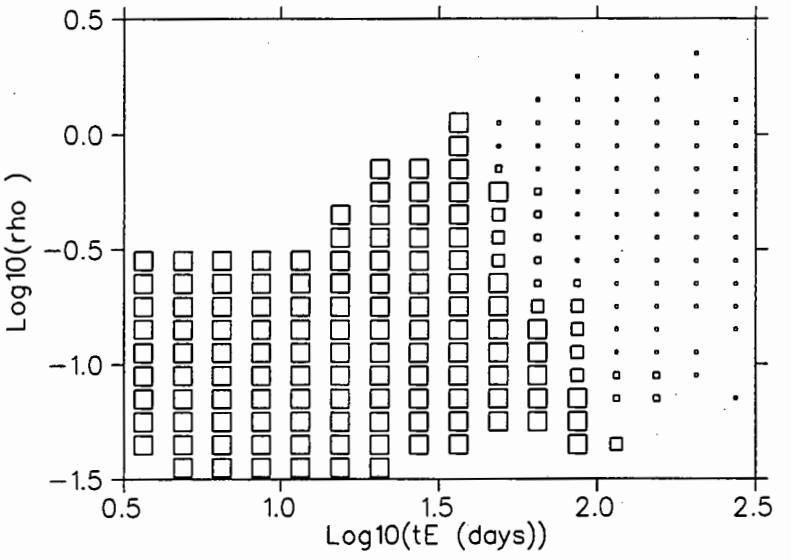

Figure 5.19: 20000 events were binned into a 20 × 20 grid. The arithmetic mean (per bin) of the fractional error with 95% confidence in ψ, $\frac{\delta\psi}{2\pi}$, is shown as a function of $\log(t_E)$ and $\log(\rho)$. The plot symbols, from small to large are for $\frac{\delta\psi}{2\pi} < 0.1$ (measurable to within 10%), $0.1 < \frac{\delta\psi}{2\pi} < 0.25$, $0.25 < \frac{\delta\psi}{2\pi} < 0.5$ and $\frac{\delta\psi}{2\pi} > 0.5$ (not measurable to within 50%.) A smaller plot symbol therefore refers to a more accurate measurement.

That means that for a few events with a very small value of x, the parallax effect will be measurable as ρ is the best indicator of a measurable parallax. For these events r_s happens to be small, hence the correlation.

$\delta\psi$ is plotted as a function of t_E and ρ in Fig. 5.19.

$\delta\rho$ had the strongest correlation with t_E, ρ, r_s and b. The correlation with r_s and b is similar in nature to that of $\delta\psi$. The fractional error is plotted in Fig. 5.20.

The trend in Fig. 5.20 is in agreement with Fig. 5.19. The most important parameter in the measurement of parallax is ρ. Fig. 5.20 indicates that ρ can only be measured to within 50% accuracy for values of at least $t_E > 40$ days, and this only for large values of ρ. For the more general case, parallax can only be measured to within 50% for $t_E > 60$ days.

Another interesting feature of the parallax anomaly is the slight dependence of $\delta\rho$ on the time of year that the peak of the event occurs in, roughly given by t_m. (t_m actually gives the time of maximum amplification for $\rho \rightarrow 0$). Fig. 5.21 shows the fractional error in ρ as a function of both t_E and t_m. A slight variation with minima corresponding to the most favourable time for measurement at roughly early January (day 4) and early June (day 187) is barely visible. These seasonal effects depend on the time of the Earth's perihelion, taken as the 4th of January in all simulations.

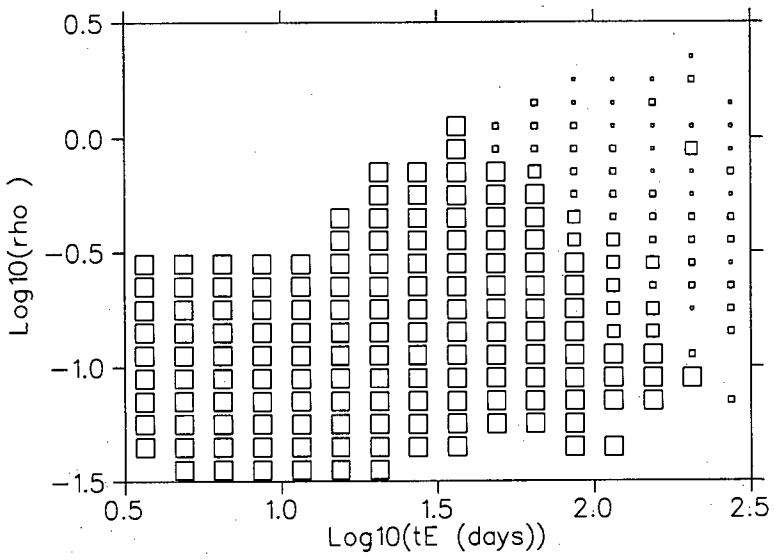

Figure 5.20: 20000 events were binned into a 20 × 20 grid. The arithmetic mean (per bin) of the fractional error with 95% confidence in ρ, $\frac{\delta\rho}{\rho}$, is shown as a function of $\log(t_E)$ and $\log(\rho)$. The plot symbol scheme is the same as that of Fig. 5.19.

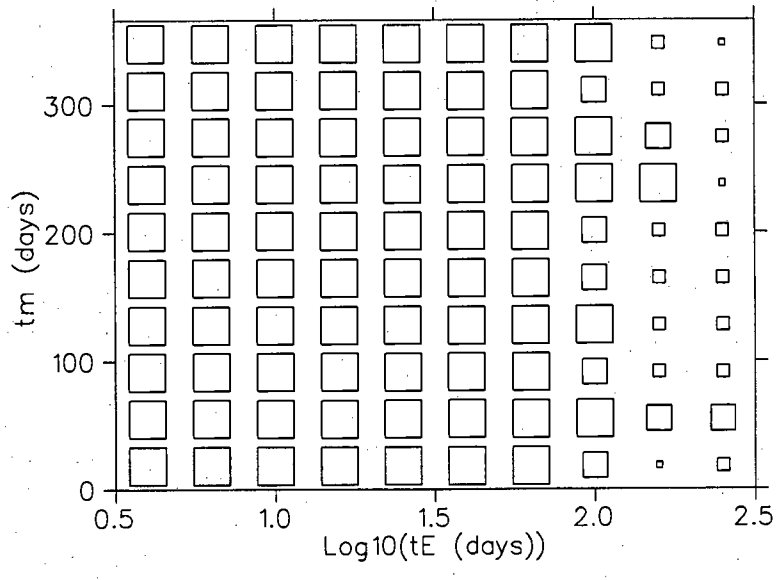

Figure 5.21: 20000 events were binned into a 10 × 10 grid. The arithmetic mean (per bin) of the fractional error with 95% confidence in ρ, $\frac{\delta\rho}{\rho}$, is shown as a function of $\log(t_E)$ and t_m. The plot symbol scheme is the same as that of Fig. 5.19.

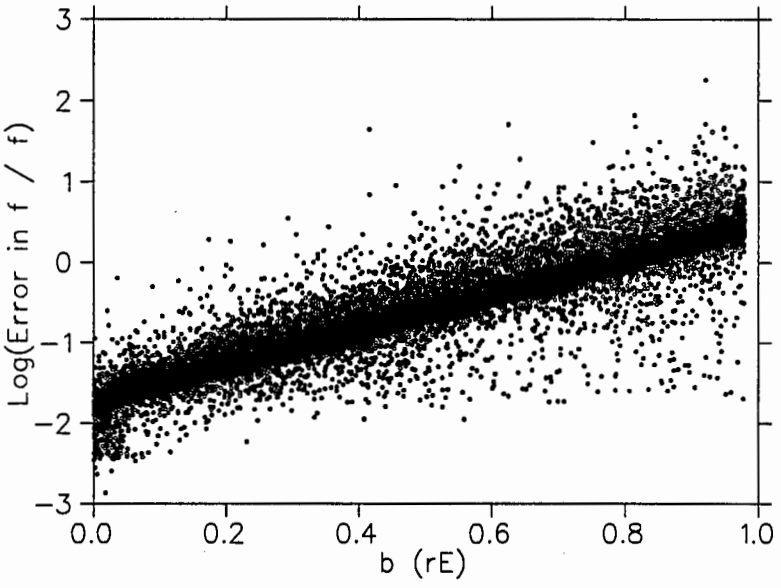

Figure 5.22: The logarithm of the fractional error (with 95% confidence) in f, $\log\left(\frac{\delta f}{f}\right)$, is shown as a function of b.

Degeneracy in the measurement of any set of microlensing parameters can be investigated to an extent by looking for a correlation between the formal errors of two parameters.

$\delta\rho$ shows correlation with $\delta\psi$ and δt_m. Almost all formal errors show correlation with δb, and the correlation with δt_m is due to the association of δt_m with δb. The errors in ρ and ψ are related as they are both indicators of measurable parallax.

5.2.3.1.2 Blending, f. Uncertainty in blending shows a very strong correlation with only one parameter, b, plotted in Fig. 5.22. In contrast, the formal error of every parameter except ρ and ψ is highly dependent on the formal error in the blending, f. As an example, δt_E is plotted as a function of δf in Fig. 5.23. The double structure in Fig. 5.23 is a result of the huge uncertainty in δt_E that is introduced by the presence of parallax, discussed below. Of importance in Fig. 5.23, is the slope as a function of f indicating the effect of blending.

5.2.3.1.3 Resolved source, r_s. Fig. 5.24 shows δr_s as a function of b and $\log(r_s)$. These are the only two parameters that show a strong correlation with δr_s. Clearly a large source radius is needed for a good measurement of r_s, and the impact parameter must be small enough for the effect to be measurable. Although actual intersection of the resolved source is not a prerequisite for detection of the effect, an intersection (indicated by a very small b) seems to improve the measurement of r_s tremendously.

As was the case with blending, the formal errors in all parameters except ψ and ρ are

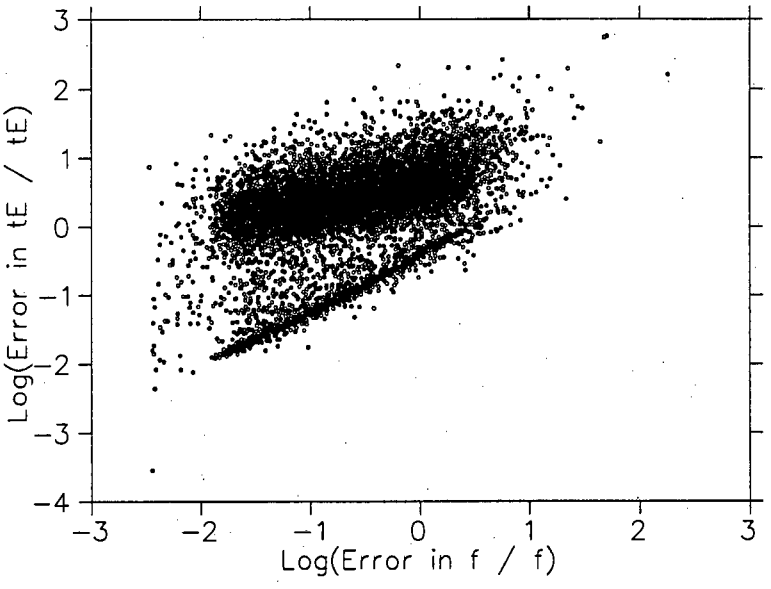

Figure 5.23: The logarithm of the fractional error (with 95% confidence) in t_E as a function of the logarithm of the fractional error (with 95% confidence) in f, $\log\left(\frac{\delta f}{f}\right)$.

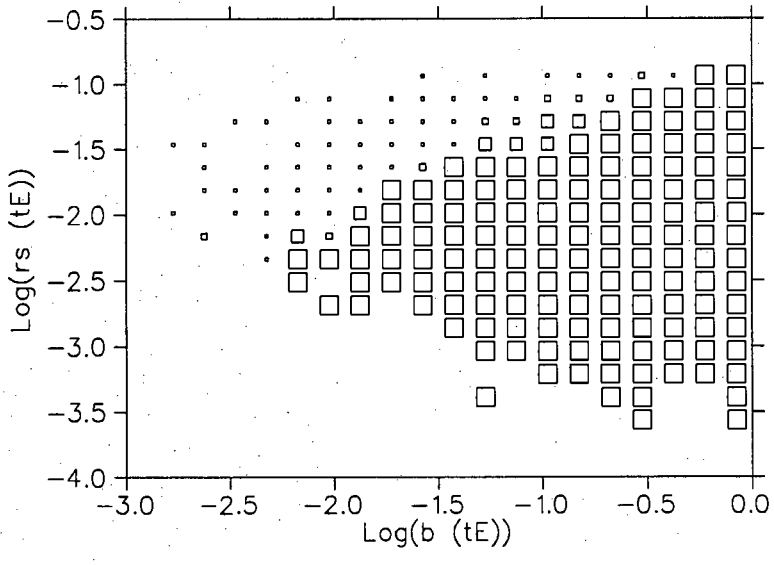

Figure 5.24: 20000 events were binned into a 20×20 grid. The arithmetic mean (per bin) of the fractional error with 95% confidence in r_s, $\frac{\delta r_s}{r_s}$, is shown as a function of $\log(b)$ and $\log(r_s)$. The plot symbol scheme is the same as that of Fig. 5.19.

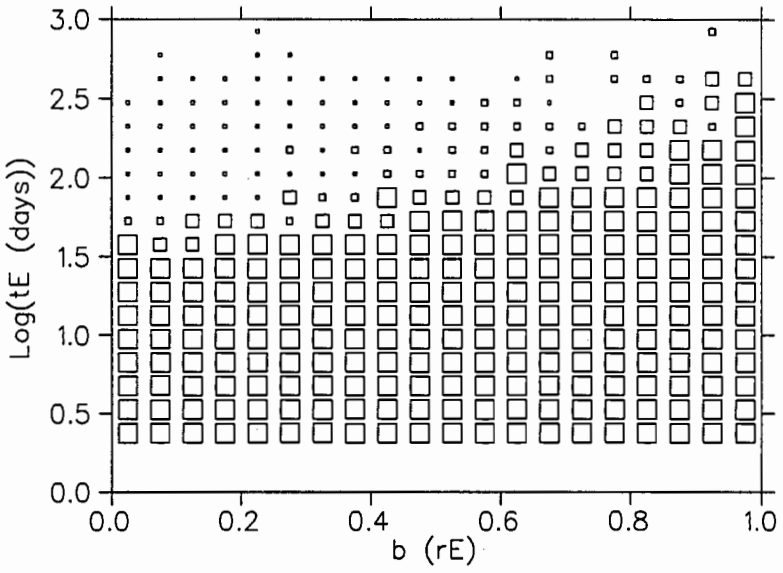

Figure 5.25: 20000 events were binned into a 20 × 20 grid. The arithmetic mean (per bin) of the fractional error with 95% confidence in t_E, $\frac{\delta t_E}{t_E}$, is shown as a function of b and $\log(t_E)$. The plot symbol scheme is the same as that of Fig. 5.19.

strongly correlated with δr_s. This is an indirect effect, due to the association of δr_s with b.

5.2.3.2 Single lens parameters

The measurability of "normal" event parameters, i.e. those that do not involve anomalies, is adversely affected by the presence of anomalies, especially blending. The negative effect these anomalies have is best described by Table 5.1 above.

5.2.3.2.1 Event timescale, t_E. The measurability of event timescale, δt_E, is most strongly correlated with t_E itself and the impact parameter b with dependence as shown in Fig. 5.25. Measurement is favoured at longer timescales and smaller impact parameters, although the timescale is of more importance.

It is apparent from Table 5.1 that the measurability of t_E plummets in the presence of anomalies. The specific anomaly most responsible for this plummet is parallax. Fig. 5.26 shows the formal error in t_E as a function of ρ. This should be compared to Fig. 5.27, the formal error in t_E as a function of what ρ *would have been*, but where ρ was reset to zero before the formal error calculation.

Introducing ρ causes the formal error in t_E for small values of ρ to increase by almost two orders of magnitude. At short timescales (or small ρ) where parallax is not accurately measured, a huge uncertainty is introduced into the formal error of t_E. Where parallax can be

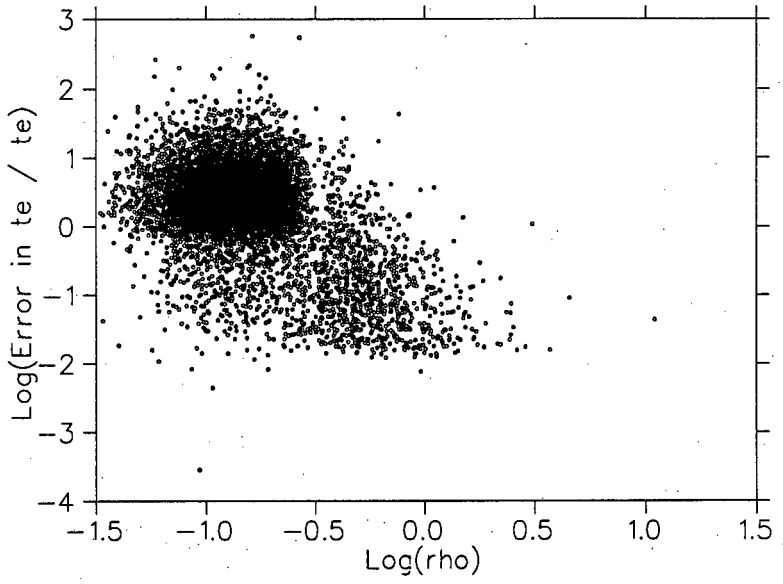

Figure 5.26: The logarithm of the fractional error (with 95% confidence) in t_E, $\log\left(\frac{\delta t_E}{t_E}\right)$, is shown as a function of $\log(\rho)$.

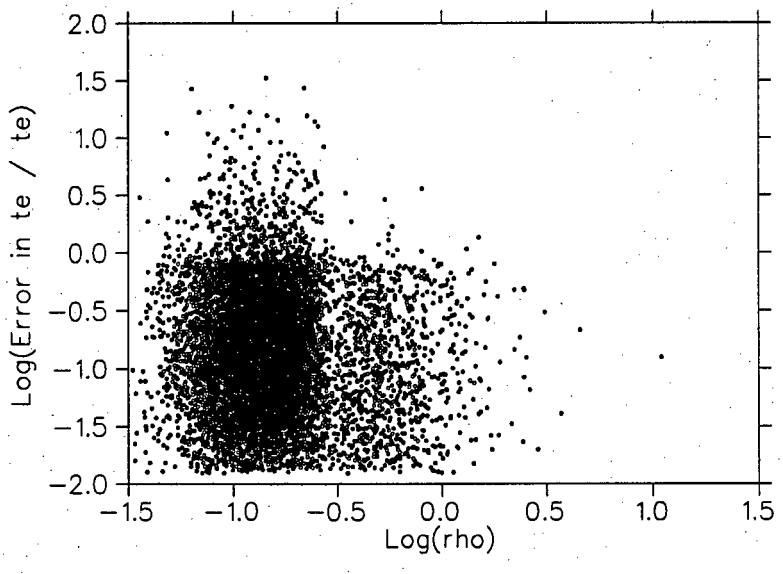

Figure 5.27: The logarithm of the fractional error (with 95% confidence) in t_E, $\log\left(\frac{\delta t_E}{t_E}\right)$, is shown as a function of $\log(\rho)$, where the value of ρ is reset to zero before the formal error calculation.

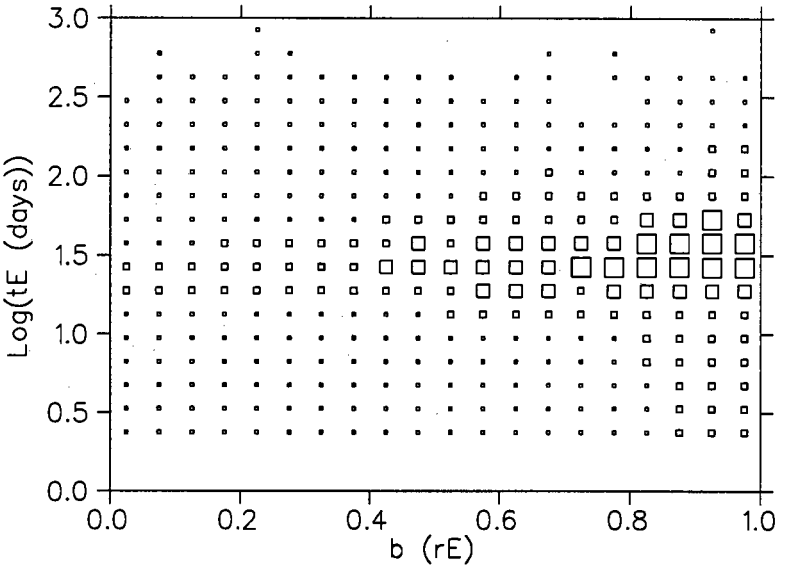

Figure 5.28: 20000 events were binned into a 20 × 20 grid. The arithmetic mean (per bin) of the fractional error with 95% confidence in m_0, $\frac{\delta m_0}{m_0}$, is shown as a function of b and $\log(t_E)$. The plot symbol scheme is *different* to that of Fig. 5.19. The smallest plot symbol refers to an error of less than 0.1% or $\frac{\delta m_0}{m_0} < 0.001$. In order of increasing size, the other plot symbols are for $0.001 < \frac{\delta m_0}{m_0} < 0.0025$, $0.0025 < \frac{\delta m_0}{m_0} < 0.005$ and $\frac{\delta m_0}{m_0} > 0.005$.

measured easily (large ρ and t_E), the degeneracy disappears, parallax is known and therefore the correct t_E is known with much smaller uncertainty.

The uncertainty in the time of closest approach in the absence of parallax, δt_m, is closely related to δt_E, and is associated with the same variables.

5.2.3.2.2 Unlensed source magnitude, $m0$. δm_0 shows the strongest correlation with b and t_E, and is plotted in Fig. 5.28.

Clearly a small impact parameter is always advantageous, but there is a turnaround in the value of t_E that is the best for measuring m_0. It should be noted that m_0 is practically always measurable to within 50% with 95% confidence. This constraint is not a very strict one on a magnitude scale, and no less is expected. The turnaround in measurement at a certain t_E value is expected from the argument that measurability of most parameters improves with increasing t_E leading to smaller uncertainty in m_0 as a result of smaller uncertainty in the other parameters. In addition, when $t_E \to 0$, the microlensing effect disappears, leaving more and more of the unlensed magnitude to facilitate a fit of $m0$.

δm_0 is correlated strongly with the uncertainty in every other parameter but $\delta\rho$ and $\delta\psi$. We illustrate this dependence in Fig. 5.29, where δm_0 is plotted as a function of δb. The

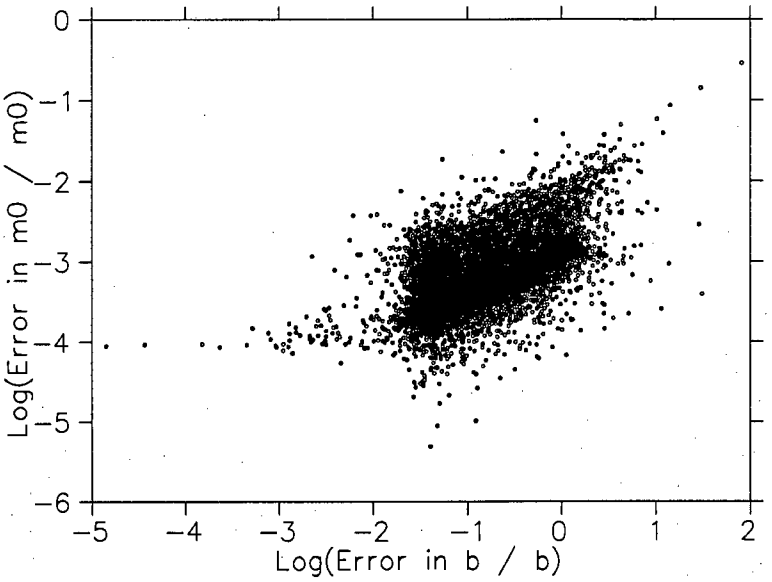

Figure 5.29: The logarithm of the fractional error (with 95% confidence) in m_0, $\log\left(\frac{\delta m_0}{m_0}\right)$, is shown as a function of $\log\left(\frac{\delta b}{b}\right)$.

importance of obtaining baseline magnitudes for fitting light curves is well known to follow up groups. Considerable observing time and effort is put into the observation of baseline, unlensed source magnitudes after an event is essentially over. Fig. 5.29 quantifies this need. Although there is large scatter in the plot, there is clearly a huge increase in the uncertainty of b (and most other parameters) with an increase in the uncertainty in m_0.

5.2.3.2.3 Impact parameter, b. Unlike the multiple parameter dependence shown by other parameters, δb is strongly correlated only with its own parameter, the value of b. This dependence is shown in Fig. 5.30. The formal error in *all* other parameters, however, is correlated with δb. This is due simply to the fact that a smaller value of b (and therefore a smaller δb) means a more pronounced microlensing effect.

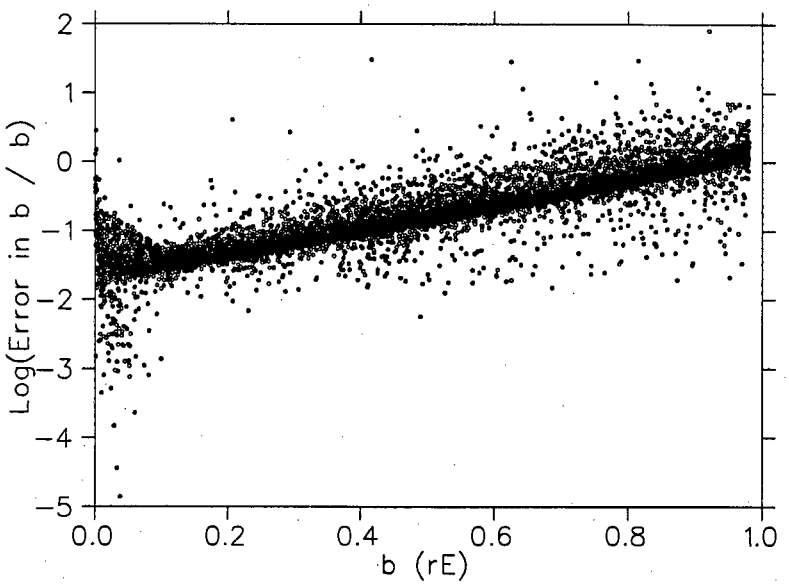

Figure 5.30: The logarithm of the fractional error (with 95% confidence) in b, $\log\left(\frac{\delta b}{b}\right)$, is shown as a function of b.

Chapter 6

Error Analysis

An estimate of the errors on calculated detection probabilities must take into consideration all numerical processes involved, as well as uncertainties in the adopted models.

6.1 Numerical errors

The calculation of difference maps, on which the planetary detection probabilities are based, is described in chapter 4. The crucial numerical step in this process is the calculation of the image postions, z_i, using Eq. 2.11. The errors in these z_i are estimated by substituting the values of z obtained from using Laguerre's method followed by a 2-D Newton-Raphson routine, back into the lens equation. The source position, ζ, is compared to the original ζ to estimate the precision of the process.

Precision is a function of the binary geometry: a, q, and ζ, but the worst case is obtained for a large a and a small q. The standard deviation and mean of the absolute value of the residuals, $\Delta\zeta = |\zeta - \zeta_{calculated}|$, is $\sigma = 3 \times 10^{-10}$ and $\overline{|\Delta\zeta|} = 2 \times 10^{-11}$ for the worst case calculated in this project, $a = 5.0$ and $q = 10^{-6}$. The residuals are plotted as a function of ζ in Fig. 6.1. The largest errors in amplification as a function of z occur at the highest amplification.

One may estimate the largest error in binary amplification by calculating the difference in amplification for two values of ζ that differ by 10^{-8}, the maximum $\Delta\zeta$, at the most unfavourable value of ζ (close to the origin). This is found to be $\Delta A \approx 0.01$ at $A = 1000$ or $\frac{\Delta A}{A} \approx 10^{-5}$.

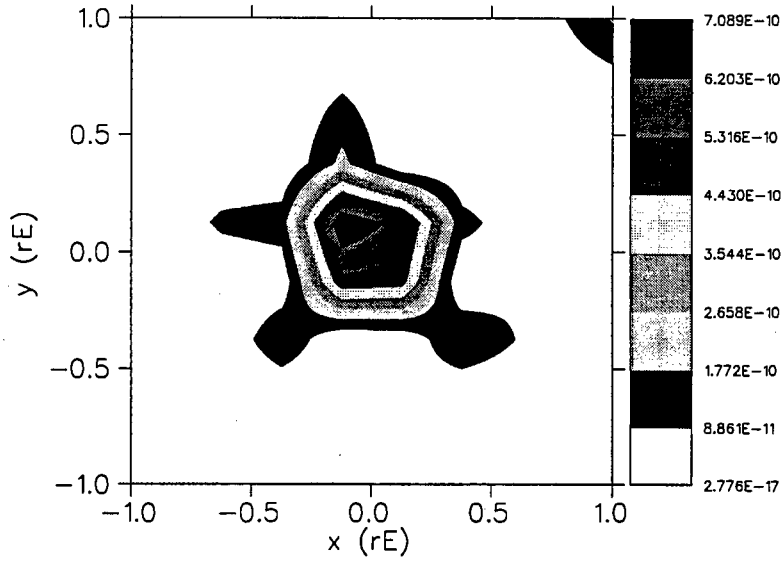

Figure 6.1: Residuals in ζ as a function of ζ.

6.1.1 Difference maps

The data load is made manageable by keeping grid points in a calculated difference map only if they differ from the single lens solution by more than 5×10^{-3} magnitudes. The error introduced in this way is much larger than the error from the amplification calculation.

6.1.2 Resolved source effects

The discrete fast Fourier routine used to calculate a point source difference map with a resolved source profile introduces a negligible intrinsic error. Any inaccuracy in this operation is introduced by way of insufficient resolution in the difference map and source profile. A source profile contains roughly $\pi N_{rE}^2 r_s^2$ integration elements leading to an error that will be dependent on the number of grid points per r_E, N_{rE}, and the resolved source size, r_s. It is assumed that the error in the discrete Fourier transform convolution is similar to that of an integration with $\pi N_{rE}^2 r_s^2$ grid points, but is not easily estimated as it also depends on the steepness of the function being integrated. If we assume a 5% error for each integration element ($\sigma_i = 0.05$) as an approximation to the error in the real contribution from that element, the error in a resolved source calculation is roughly

$$\sigma = \frac{\sigma_i}{\sqrt{\pi N_{rE}^2 r_s^2}} \tag{6.1}$$

Blending, on the other hand, is a purely analytical operation and should not introduce

error into the calculations.

6.1.3 Detection routine

The planet detection algorithm described in 4.2.4 models actual sampling closely but differs in two respects:

1. Sampling is evenly distributed, unlike real sampling that is distributed in nightly clumps and is generally "patchy" in nature due to weather etc. This should only affect very small and very large detection efficiencies. For example, if an observing group had access to telescopes on alternate weeks only they have at most a 50% detection probability for a short-lived anomaly at peak, even if this anomaly should always be detected with a sampling rate of half the observer's total sampling rate. On the other hand, a very short-lived anomaly may be detected by chance during a burst of sampling in good weather when it wouldn't be discovered in a more systematic search.

2. Difference maps are rotated in steps of 10 degrees each for detection purposes. This rotational sampling is not expected to be a serious source of error, but rotation proceeds by way of a linear interpolation of the data. Interpolation is at worst equivalent to convolving a few points with a square source of side length equal to the grid spacing, $\frac{1}{N} = 0.000625$ or $\frac{1}{N} = 0.00125$ for the spacings used in these simulations. ($N = 800$ for $q = 10^{-3}$ and $N = 1600$ for smaller q.)

These errors will be small, especially where the difference map is convolved with a large source radius.

6.2 Distribution models

The only check that can be performed on microlensing models that yield event parameter distributions is a comparison with the current data. Unfortunately, some parameters and distributions are highly uncertain ranging from the mass function, which is obtained from a fit to the MACHO events [Alcock et al. 1997a], [Zhao et al. 1996] to the actual distance to the Bulge, which is uncertain by at least 10%.

There is little doubt that the model adopted may be inaccurate, but the general conclusions drawn in 5.2 are qualitatively not highly dependent on the model.

6.3 Conclusion of error analysis

The inaccuracy of the calculations for planetary detection are small, probably on the order of 1%. A more controversial point would be the specific choice of detection criteria, which is why the detection criteria themselves are modeled using the parameters h_c and c. This choice is crucially dependent on the amount of data that is needed to break the degeneracies of a binary lens fit. Detection probability estimates for non-planetary anomalies will similarly suffer the most from the distribution models and the choice of detection criteria.

All in all the precision of calculations is high, and the numerical results are presented with confidence.

Chapter 7

Conclusions

Most of the issues in this chapter have been discussed in more detail above, but the most important points are summarised below.

7.1 Observation strategy

It has been shown that detection probabilities of all anomalies are highly dependent on the observation strategy. The relevant parameters for planet detection are discussed one by one.

7.1.1 N

The gain in planet detection probability with increasing N is almost linear up to $N = 200$, whereafter saturation is reached. Considering the fact that observation cost scales linearly with N, larger values become highly inefficient.

7.1.2 c

Planet detection probability is strongly dependent on the photometry. At the lower values of c, i.e. good photometry, large gains can be made by small increases in precision. At $c \approx 0.05$ *mag* or more detection probability flattens out, so if photometry precision is around 5% or more gains in detection probability can be made by increasing sampling frequency N at the cost of precision.

7.1.3 e

All efforts should be made to have a real-time alert capability, as planet detection probability can almost be doubled in most cases by quadrupling sampling frequency after two anomalous data points. The overall cost in observation time is negligible, and the additional data will be paramount to breaking degeneracy of binary light curve fits.

7.1.4 R_c

The wisdom of following microlensing events with $u > 1$ is questionable, but some gains may still be made if the observation time is available. From a planet detection point of view it is hardly ever beneficial to follow an event for $u > 1.5$ even if more time is available. In addition observation cost scales as R_c^2. If many events are in progress, the decision on which events to follow should be based almost exclusively on the events with the highest current amplification (and thus smallest u) if the main purpose of the observation program is planet detection.

7.1.5 h_c

At lower sampling frequency, N, planet detection probability is strongly dependent on how many consecutive points constitute a detection. At N in the region of TF observations, the dependence is smaller, so that a genuine detection should be recognisable as such.

7.1.6 Other anomalies

Survey observations (TS) are likely to measure non-planetary microlensing parameters acceptably (within 50% with 95% confidence, or within 25% with 68% confidence) about half as often as follow up observations (TF) when following the same event. This is one area where following events to further from the primary ($R_c = 2$) would be beneficial, as the follow up group would increase the frequency of parameter measurement for most parameters by a factor of roughly two. This increase is at severe cost to observation time and has a very small gain for planet detection, however.

7.2 Influence of event geometry on detection and measurability

7.2.1 a

The best planet detection probability occurs within the lensing zone, which may be broader or narrower depending on the value of R_c. ME observations do not adhere strictly to the lensing zone, as they concentrate mainly on the central caustic enabling a much larger range of orbital separations to be detected, but only for large planets.

7.2.2 q

All planet detections are highly dependent on mass ratio, with a very steep drop in detection probability from $q = 10^{-3}$ to $q = 10^{-4}$.

7.2.3 f

The effect of blending on planet detection overall is small, and is the biggest for small mass ratio. Blending has a huge effect on the measurability of other parameters, most notably t_E and b.

7.2.4 r_s

Resolved source effects on planet detection are not as simple as previously thought. A larger resolved source can lead to a dramatic increase in detection probability with TF observations for $a > 1.0$. This increase could enhance detection of smaller mass ratio planets, depending on the observation strategy and the real distribution of orbital separations.

7.2.5 t_E and t_m

The covariance matrix method used in this work predicts that the timescale and time of closest approach becomes very difficult to measure with the introduction of parallax. This is because parallax is rarely measurable and if there is uncertainty in the parallax, it introduces an uncertainty into the timescale.

7.2.6 b

Impact parameter is the most important parameter "under the observer's control" for planet detection. The importance of following high amplification events cannot be overemphasised.

7.2.7 ρ and ψ

Parallax is rarely measurable, and only for events with t_E larger than at least 60 days for TF observations. The measurement does gain from following events out to larger R_c, but this is at the cost of observing time.

7.3 The future of Galactic microlensing

It is clear from this investigation that there are observation scenarios that offer improvements to planet detection probability. The most efficient strategy investigated, ME, reaches detection probability of 75% in its lensing zone and is sensitive to a large variety of orbital projections. Unfortunately, it requires impact parameters of 0.1 r_E, and such events are rare. Yet these promising numbers should inspire the investigation of other scenarios, such as microlensing in M31 and other nearby galaxies where high amplification events may be detected in number.

The calculations show that typical survey observations (TS) are unlikely to yield any planet detections, but the number of event detections by these groups is crucial to planet detection as a whole, as there has been a shortage of events to follow to date. With more events available, follow up observers could select events for small impact parameter and uncrowded, high precision photometry.

Current follow up observations (TF) stand a good chance of detecting an extra-solar planet. Detection probability for TF observations reach more than 30% for Jupiter-mass planets in the lensing zone, and exceed 10% for Neptune-mass planets. Gains can be made in the foreseeable future merely by improving sampling frequency to $N = 200$ and photometry to 0.5% so that a 1% perturbation will be at the 2σ-level. Large gains in efficiency are possible by following events only when they are close to the primary, but this is made difficult by the current shortage of events.

All things considered, the future of microlensing as a technique for planet detection is very bright.

Bibliography

[Alard 1997] Alard C., Lensing of unresolved stars towards the galactic bulge, A&A 321:424 1997

[Albrow et al. 1997] Albrow M. et al., Proceedings of the 3rd international workshop on gravitational microlensing surveys, 1997

[Albrow et al. 1998] Albrow M. et al., The 1995 pilot microlensing campaign of PLANET: searching for anomalies through precise, rapid, round-the-clock monitoring, preprint 1998

[Alcock et al. 1993] Alcock C. et al., Possible gravitational microlensing of a star in the Large Magellanic Cloud, Nature 365:621 1993

[Alcock et al.] Alcock C. et al., APJ 445:133

[Alcock et al. 1995] Alcock C. et al., First observation of parallax in a gravitational microlensing event, APJ 454:L125 1995

[Alcock et al. 1997a] Alcock C. et al., The MACHO project: 45 candidate microlensing events from the first-year galactic bulge data, APJ 479:119 1997

[Alcock et al. 1997b] Alcock C. et al., MACHO alert 95-30: First real-time observation of extended source effects in gravitational microlensing, APJ 491:436 1997

[Aubourg et al. 1993] Aubourg E. et al., Evidence for gravitational microlensing by dark objects in the Galactic halo, Nature 365:623 1993

[Becker et al. 1997] Becker A. et al., Global Microlensing Alert Network, American Astronomical Society Meeting 191:83.05 1997

[Bennett & Rhie 1996] Bennett D.P., Rhie S.H., Detecting Earth-mass planets with gravitational microlensing, APJ 472:660 1996

[Bolatto & Falco 1994] Bolatto A.D., Falco E.E., The detectability of planetary companions of compact galactic objects from their effects on microlensed light curves of distant stars, APJ 436:112 1994

[Buchalter & Kamionkowski 1997] Buchalter A., Kamionkowski M., Rates for parallax-shifted microlensing events from ground-based observations of the galactic bulge, APJ 482:782 1997

[Chang & Refsdal 1984] Chang K., Refsdal S., Star disturbances in gravitational lens galaxies, A&A 132:168 1984

[De Rujula et al. 1991] De Rujula A., Jetzer Ph., Masso E., Dark mass moments, MNRAS 250:348 1991

[Di Stefano & Esin 1995] Di Stefano R., Esin A.A., Blending of light in gravitational microlensing events, APJ 448:L1 1995

[Dominik 1996] Dominik M., Galactic microlensing beyond the standard model, Universitat Dortmund 1996

[Einstein 1911] Einstein A., Uber den Einfluss der Schwerkraft auf die Ausbreitung des Lichtes, Annalen der Physik, 35:898 1911

[Einstein 1936] Einstein A., Lens-like action of a star by the deviation of light in the gravitational field, Science 84:506 1936

[Gaudi & Gould 1996] Gaudi B.S., Gould A., Detection rates for close binaries via microlensing, preprint, astro-ph/9606104 1996

[Goldberg & Wozniak 1997] Goldberg D.M., Wozniak P.R., Astrometric shifts in the OGLE-1 microlensing events, preprint, astro-ph/9712262 1997

[Gould & Loeb 1992] Gould A., Loeb A., Discovering planetary systems through gravitational microlenses, APJ 396:104 1992

[Gould 1992] Gould A., Extending the MACHO search to $\sim 10^6\ M_\odot$, APJ 392:442 1992

[Gould 1995a] Gould A., K-band microlensing of the inner galaxy, APJ 446:L71 June 1995

[Gould 1995b] Gould A., A new MACHO search strategy, APJ 447:491 1995

[Gould & Gaucherel 1996] Gould A., Gaucherel C., Finite source effects in microlensing events, preprint, astro-ph/9606105 1996

[Griest et al. 1991] Griest K. et al., Gravitational microlensing as a method of detecting disk dark matter and faint disk stars, APJ 372:L79 1991

[Griest & Safizadeh 1997] Griest K., Safizadeh N., The use of high magnification events in discovering extra-solar planets, preprint, astro-ph/9710342v2 1997

[Han 1997] Han C., The effects of amplification bias in gravitational microlensing experiments, APJ 484:555 1997

[Hardy & Walker 1995] Hardy S.J., Walker M.A., Parallax effects in binary microlensing events, MNRAS 276:L79 1995

[Kamionkowski 1995] Kamionkowski M., Microlensing by stars, APJ 442:L9 1995

[Kiraga & Paczyski 1994] Kiraga M., Paczynski B., Gravitational microlensing of the galactic bulge stars, APJ 430:L101 1994

[Lee & Han 1997] Lee S., Han C., The effect of luminous lens blending in gravitational microlensing experiments, preprint astro-ph/9707178 1997

[Mao & Paczyski 1991] Mao S., Paczynski B., Gravitational microlensing by double stars and planetary systems, APJ 374:L37 1991

[Marcy & Butler 1996] Marcy, Butler, APJ 464:L147 1996

[Mayor & Queloz 1995] Mayor, Queloz, Nature 378:355 1995

[Paczynski 1986] Paczynski B., Gravitational microlensing by the galactic halo, APJ 304:1 1986

[Paczynski 1991] Paczynski B., Gravitational microlensing of the galactic bulge stars, APJ 371:L63 1991

[Paczynski et al. 1994] Paczynski B. et al., The distribution of galactic disk stars in Baade's window, APJ 107:6:2060 1994

[Press et al. 1992] Press W.H. et al., Numerical Recipes in C, Cambridge university press, 1992

[Schneider & Weiss 1986] Schneider P., Weiss A., The two-point-mass lens: detailed investigation of a special asymmetric gravitational lens, A&A 164:237 1986

[Schneider et al. 1992] Schneider P., Ehlers J., Falco E., Gravitational lenses, Springer Berlin 1992

[Udalski et al. 1994a] Udalski A. et al., The optical gravitational lensing experiment. The optical depth to gravitational microlensing in the direction of the bulge, Acta. Astron. 44:165 1994

[Udalski et al. 1994b] Udalski A. et al., The optical gravitational lensing experiment: OGLE no.7: Binary microlens or a new unusual variable?, APJ 436:L103 1994

[Walsh et al. 1979] Walsh D. et al., 0957+561 A, B: twin quasistellar objects or gravitational lens?, Nature 279:381 1979

[Wambsganss 1997] Wambsganss J., Discovering galactic planets by gravitational microlensing: magnification patterns and light curves, MNRAS 284:172 1997

[Witt 1990] Witt H.J., Investigation of high amplification events in light curves of gravitationall lensed quasars, A&A 236:311 1990

[Witt 1995] Witt H.J., The effect of the stellar size on microlensing at the Baade window, APJ 449:42 1995

[Wolzczan 1992] Wolzczan, Frail, Nature 355:145 1992

[Wozniak & Paczynski 1997] Wozniak P., Paczynski B., Microlensing of blended stellar images, APJ 487:55 20 1997

[Zhao et al. 1995] Zhao H., Spergel D.N., Rich R.M., Microlensing by the galactic bar, APJ 440:L13 1995

[Zhao et al. 1996] Zhao H.S., Rich R.M., Spergel D.N., A consistent microlensing model for the galactic bar, MNRAS 282:175 1996

[Zhao 1996] Zhao H.S., MNRAS submitted 1996